INVESTIGATIONS OF ATOMIC TRANSPORT INDUCED BY HEAVY ION IRRADIATION

Thesis by

Thomas C. Banwell

In Partial Fulfillment of the Requirements

for the Degree of

Doctor of Philosophy

California Institute of Technology

Pasadena, California

1986

(Submitted May 5, 1986)

Acknowledgements

There are quite a number of people who contributed directly and indirectly to making my stay at Caltech a rewarding experience. Very little would have been achieved without the support, inspiration and guidance afforded me by my advisor, Prof. M-A. Nicolet. Thank you. My parents have been a continual source of love and support.

I would like to thank Dr. Paula Grunthaner for helping me with the XPS work, and Dr. Tim Sands for providing the TEM analysis. Prof. S. S. Lau also provided valuable guidance. Prof. C. A. Barnes and Mr. William Schick provided considerable assistance with the ion accelerators, the 3MV in particular. Discussions with Prof. D. Cohen and Prof. N. Corngold made a lot of the work enjoyable. Dr. David Scott helped in many ways as a very good friend and colleague. It was a pleasure to have worked with Mr. Xinan Zhao on a number of experiments. Mr. Rob Gorris and Mr. Rouel Fernandez helped with equipment and sample preparation. Dr. J. R. Miles also provided good counsel at difficult times. Mrs. Michell Parks provided valuable assistance and friendship. Drs. Adam and Elzbieta Kolawa provided assistance with CAM of this manuscript. I would also like to thank Mr. Douglas Bookhout for setting me in good direction years ago. A fellowship from IBM is also gratefuly acknowledged.

I would like to thank the people at OPE for helping me with the Folkdance club. Ardith, Jenny, Kayla, Marta, Michele and Nancy helped in a number of different ways too.

Abstract

The mechanisms of atomic transport induced by ion irradiation generally fall into the categories of anisotropic or isotropic processes. Typical examples of these are recoil implantation and cascade mixing, respectively. Each possesses its own characteristic fluence dependence (linear and square-root, respectively), although both may occur concurrently. In this case, these processes can be distinguished by carefully examining the fluence dependence at low fluences (less that $10^{15}cm^{-2}$). Parametric studies can produce added insight.

We have measured the interaction of these processes in the mixing of $Ti/SiO_2/Si$, $Cr/SiO_2/Si$ and $Ni/SiO_2/Si$ multi-layers irradiated with Xe at fluences of 0.01 - $10x10^{15}cm^{-2}$. The fluence dependence of net metal transport into the underlying layers was measured with different thicknesses of SiO_2 and different sample temperatures during irradiation (-196 to 500C). There is a linear dependence at low fluences. The initial slope depends on the sample temperature. At high fluences, a square-root behavior predominates. For thin SiO_2 layers (< 20nm), the cross-over point depends on the SiO_2 thickness. These results are readily interpreted in terms of competition between the flux of injected atoms and diffusion of the accumulating metal. Metal appears to be the dominant moving species in these systems. The initial linear dependence was not observed in samples without SiO_2, which shows that the effect is not due to cascade overlap.

The detailed analysis allows us to speculate on the role of chemical reaction kinetics in controlling the outcome of intra-cascade processes. There is no significant correlation between the reactivity of the metal with SiO_2 and the

amount of mixing observed when the irradiations are performed at 25C or below. The contribution from primary recoils is quite pronounced since the gross mixing is small. A significant correlation exists between the mixing and the energy deposited through elastic collisions F_D. Several models are examined in an attempt to describe the transport process in Ni/SiO_2. It is likely that injection of Ni by secondary recoil implantation is primarily responsible for getting Ni into the SiO_2. There were a few more objections against the other conceivable limiting cases. Secondary recoil injection is thought to scale with F_D. Trends in the mixing rates indicate that the dominant mechanism for Ti and Cr could be the same as for Ni. Nevertheless, the structure of the mixed region is very different for the three metals. The product of chemical reactions were identified with TEM and XPS. The low temperature results suggest that kinetic constraints are responsible for suppressing the chemical reactions that one might anticipate.

The processes of atomic transport and phase formation clearly fail to be separable at higher temperatures. A positive correlation with chemical reactivity emerges at higher irradiation temperatures. This was not pursued beyond preliminary results reported for Ti or Cr. The temperature at which rapid mixing occurs is not much below that for spontaneous thermal reaction. Less Ni is retained in the SiO_2 at high irradiation temperatures. Ni incorporated in the SiO_2 by low temperature irradiation is not expelled during a consecutive high temperature irradiation. The Ni remains trapped within larger clusters during a sequential 500C irradiation.

Chapter I Introduction

What happens when an ion with an energy of a few hundred keV hits a solid material? The answer to this question naturally depends on the solid, the ion, the implantation conditions, and why one is asking the question. A satisfying answer can probably be found if the solid is a single element like Si or Ge for almost any ion. Many questions concerning crystal damage and impurity effects can also be answered for GaAS, but are difficult for other compound semiconductors. There is a large body of knowledge available on atomic transport and phase formation when the solid consists of a metal and silicon, or two metals. The questions are motivated by both technological necessity and scientific curiosity.

A relatively new entry into the field is the ternary system with one very reactive component. A metal film on a refractory oxide substrate is a typical example. In addition to the recurrent question of phase formation, the dominant mechanisms of atomic transport have not been identified. Many of the component processes such as recoil implantation and random walk mixing are the same as in the other systems, however, their relative contributions are not known. The difference in reactivity between the components also introduces a new role for kinetic constraints on possible chemical reactions.

This work examines the problem outlined above for the mixing of Ti, Cr or Ni on SiO_2 induced by Xe irradiation. These systems where chosen becouse they are ballistically similar but differ significantly in their reactivity with SiO_2. Ti is very reactive while Ni is non-reactive and Cr is intermediate in reactivity. They have similar atomic mass. An etching technique is described in chapter II which

circumvents some of the usual resolution limitations and permits quantitative characterization of the mixing profiles. A detailed parametric study was undertaken with the Ni/SiO_2 system to identify correlations with the implantation (or irradiation) conditions. This system was chosen for extensive investigation since two apparently reliable etchants were available, there is no problem with metal film oxidation, and the mass separation between Si, Ni and Xe is ideal for depth profiling with MeV He backscattering spectrometry. Fairly general concepts are developed in chapter III to describe the results of the experiments. Several fairly simple analytical models are used in chapter IV to help identify the dominant processes controlling the irradiation induced mixing of metal with SiO_2. A prominent feature of the metal profiles in the SiO_2 is an exponential tail attributed to primary recoil implantation. A simple model is developed in chapter V to describe these tails. Although this model is founded on established principles, several new approximations to describe the range statistics are employed. The problem of a random walk on a sphere entered into the approximation and a simple solution for the moments represents the pet project.

Our final speculation made in chapter VI is that there are probably kinetic constraints alleviated with the creation of a thermal spike.

Chapter II Experimental Methods

A. Introduction

The experiments were designed to identify correlations between the ion induced mixing of metal films on SiO_2 layers, and the implantation conditions and particular metal M. This was often accomplished by measuring the effect of a particular parameter change on the relationship between mixing and the incident ion fluence Φ. 2 MeV He backscattering spectrometry (RBS) was the primary analytical tool. X-ray photoelectron spectroscopy (XPS) and transmission electron microscopy (TEM) were used with selected samples.

B. Sample Preparation

1. Film deposition

Si wafers served as supporting substrates in these experiments. Commercially available (Monsanto, Motorola) 0.005 - 0.02 Ωcm boron doped 2 inch polished <111> Si wafers were generally used. Occassionally 1 - 3 Ωcm phosphorus doped 2 inch polished <100> Si wafers were used instead. Each wafer was sequentially cleaned ultrasonically in acetone, methanol, and de-ionized water prior to etching in 10% HF. The wafers were then placed in a solution of 1:1:5 28% NH_3:30% H_2O_2:water. This treatment produces an oxide layer equivalent to 1.2 - 1.4nm SiO_2 , as measured using either ellipsometry or the $^{16}O(d,\alpha)^{14}C$ nuclear reaction [1]. The desired SiO_2 layer was grown by thermal oxidation after etching these wafers in 10% HF. Thick SiO_2 layers (~1μm) were grown by

wet oxidation at 1100C, and the thickness measured using RBS. One set of experiments used thin SiO_2 films (<20nm) which were produced by dry oxidation at 850C, and measured using both ellipsometry and backscattering with the 3.05MeV $^{16}O(\alpha,\alpha)^{16}O$ resonance. Following characterization, a 10-100nm film of either Ti, V, Cr, Ni, Fe, Nb, or Pt was deposited onto the oxidized Si wafers in an oil-free e-beam evaporation system (background pressure $<10^{-7}$ Torr). Thin (<50nm) Ni and Fe films, as well as V, Ti, Cr and Nb films exhibited good adhesion to the SiO_2. Pt films had a tendency to peel off.

2. Implantation

The intention was to introduce a prescribed dose Φ of mono-energetic ions, such as 290keV Xe, into the sample, which was held at a desired temperature T in vacuum. An MPR 400 research implanter (Varian) with a hot cathode source and paraxial electrostatic beam rastering was employed. The samples were mounted in a target chamber pumped with a CTI-7 cryopump assisted by a liquid nitrogen cooled shroud. The chamber pressure was 10^{-7}–10^{-6} Torr, depending on the carousel temperature. Radiative heating was thought to induce desorption of gases from the chamber's surfaces. Two carousel-type target holders were available, one with an operating range of -196 to +350C using external heating or cooling, and the other with a range of room ambient to +600C using internal heating. The samples were mounted onto 3mm thick Al or stainless steel plates using thermally conductive paste for sample temperatures between -196 and +200C, or with compression clips at higher temperatures. Both carousels had a relatively large thermal mass, and their temperature was measured with a thermocouple. Adjustable slits defined the implanted region. The beam current was typically 1 - 3μA cm^{-2}, although this was substantially reduced to give 3 - 5 minute exposure times when low doses were desired. The estimated

temperature changes associated with beam heating were not significant (please see Appendix All.1 on page 116). The ion dose Φ was initially preset using integration of the target current. SiO_2 blanks prepared by wet oxidation were included with samples implanted with Xe. RBS was used to measure the amount of Xe implanted into the SiO_2 blank. The two methods agreed within 2% for Φ exceeding $5x10^{14}$ cm^{-2}, although only within 15% for Φ below 10^{14} cm^{-2}, due to interference from leakage currents when small beam intensities were required. Secondary electron currents were suppressed by maintaining a +90V bias on the target and using a Faraday cup configuration [2]. The estimated lateral variation was less than 5% as determined by RBS of Xe implanted SiO_2 blanks.

3. Chemical Etching

The intermixed region could not be resolved with the unreacted metal layer present. This was due to limited RBS depth resolution and limited contrast from TEM. Selectively etching away the unreacted metal layer circumvented these limitations, while transfering the uncertainty to the etching process. Many etchants were tested. A satisfactory etch must quantitatively remove the unreacted metal, but not alter the mixed region. The etchant(s) should not react with SiO_2 or compounds comprising of M-Si, M-O, M-Si-O, nor should it leach out metal trapped within the SiO_2. Ti,Cr, and Nb are difficult to etch since they tend to form passivating oxides [3,4]. HF can not be used, for obvious reasons, while oxidizing agents like NOCl are too aggresive. Boiling concentrated HCl (37% reagent, b.p. 80C) was found to be a satisfactory etch for Ti,Cr, and Ni. The samples were rinsed with water and methanol after etching. A commercial $Ce(SO_4)_4$ solution (Nichrome etch, Transene Co.) was the preferred etch for Ni. Ni samples treated with the Nichrome etch were rinsed sequentially in 2% aq. H_2SO_4, de-ionized water, and methanol after etching.

A conclusive test of etch selectivity would require the ability to distinguish small differences between etched and un-etched samples. Etching would be unnecessary if independent means existed to prove that etching did not disturb the mixed layer. The alternative is to look for evidence that the etching is not selective enough.

The following factors were examined: incomplete etching, persistent etching, inherent selectivity of the etching mechanism, etchant permeability into the mixed layer, and etching of M-Si and M-O compounds formed by thermal reaction. No metal was detected with RBS ($<10^{13}$ atoms cm^{-2}) on the SiO_2 surface after etching as-deposited M/SiO_2 layers with the appropriate etch. Repeated etching did not alter the residual metal profile in implanted samples. There was no visual indication of etching by the HCl at 25C; the metallic luster of the films remained after a one hour exposure. Etching initiated with the onset of gas evolution from the surface of the samples upon boiling, and was complete within 30 seconds. It is likely that HCl adsorbed on the Ti metal surface catalyzes the net reaction $Ti + 2H_2O \rightarrow 2H_2 + TiO_2$, which would otherwise produce passivation [3], and similarly for Cr. TiO_x with $x<0.3$ (often considered a solid solution of Ti-Ti_2O_3) formed by thermal reaction was found to etch like Ti. Cr films contaminated with substantial surface O would not etch. The Nichrome etch removes Ni with the redox reaction $Ni^0 + 2Ce^{4+} \rightarrow 2Ce^{3+} + Ni^{2+}$ [5]. These mechanisms could produce inherently selective etching. The etching of Ni with hot HCl may be promoted by the temperature related increase in the H^+ ion activity [6] or HCl adsorption. The compounds Ni_2Si, NiSi, $TiSi_2$, and $CrSi_2$ formed by thermal reaction were not affected by etching. One might expect to find Cl or Ce within the SiO_2 if the etchant permeates the mixed region. Cl was never evident by RBS, although this does not rule out its presence since it could escape during He bombardment. A small peak, probably corresponding to $\sim 10^{12}$ cm^{-2}, was barely

discernable by ESCA at a binding energy of 199eV on the exposed surface of etched implanted Ni samples. A small amount of Ce ($\sim 10^{13}$ cm^{-2}) was occassionally detected on the surface of the nichrome etched Ni samples by RBS, but was independent of Xe dose. A larger Ce residue was apparent when the 2% H_2SO_4 rinse was once accidentally omitted. Two identical implanted Ni/SiO_2 samples had indistinguishable residual Ni profiles when one was etched in HCl and the other in nichrome etch. There was some indication that leaching occurred with hot HCl containing 2-5% HNO_3. There was no detectable shift (< 1nm) in the mean position of the Xe profile in implanted SiO_2 blanks subjected to the HCl treatment. Resonant He backscattering analysis showed no discernable O loss from samples with thin SiO_2 layers, either.

The experimental results themselves provide evidence that the etching process selectively removes unreacted metal. There is a significant accumulation of the implanted Xe within the SiO_2 which distinguishes the M-SiO_2 interface in RBS by a discontinuity in the Xe spectra. This discontinuity moves to the surface after etching, suggesting that only free metal is removed. RBS, TEM, and XPS all show that a continuous SiO_2 layer, about 5nm thick and devoid of significant Ni, isolates the Ni bearing region from the Ni-SiO_2 interface; hence, neither etchant comes in contact with the intermixed region. There is agreement between the measured recoil tails for Ti, Cr, and Ni, and their theoretical profiles. The Ni result may be taken as validation of the calculation, while the calculations indicate that <5nm of the mixed region is removed by etching, even though both Ti and Cr may extend to the interface.

C. Analysis

1. MeV He Backscattering Spectrometry

2 MeV He backscattering spectrometry (RBS) was used to measure atomic profiles. In RBS, the sample is bombarded with mono-energetic He. The sample's composition is inferred from the energy spectrum of backscattered He. The incident He beam and a Si surface barrier detector were coplanar with the sample's single rotation axis, which was perpendicular to the incident beam. A 170^0 scattering geometry was employed. Signal processing was done with an Ortec 142 charge sensitive preamplifier, an Ortec 572 spectroscopy amplifier with pile-up rejection, and a Tracor-Northern 1710 multichannel analyzer (MCA) with 100MHz ADC. 2 MeV He was obtained with the Kellog 3MV van de Graaff type accelerator or a tandem mode 3SDH Pelletron accelerator. Two sets of beam slits were used in front of the sample; one set to define the incident He beam, and the second to obstruct He scattered off the first slits [1].

The following well-known model facilitates discussion of the technique [7]. Most of the incident He atoms travel undeflected through the first micron or so of the sample, experiencing a "viscous" energy loss due to electronic stopping along the way. This can be described by $\frac{dE_i(x)}{ds} = -S_e(x,E_i)$, where E_i is the average incident particle energy at position x, and s is the path length. The stopping power $S_e(x,E_i)$ is determined by local sample composition; it has a slowly varying energy dependence which can usually be neglected for MeV He travelling a distance $\Delta s \lesssim 500$nm (surface approximation). In traversing a short distance ds at position x, a small number of He atoms out of an incident number Q will experience a nuclear collision with a target atom k within ds such that they are scattered by an angle $\varphi=170^0$ into the solid angle $\delta\Omega$ defined by the detector. The scattering cross-section $(\partial\sigma/\partial\Omega)_k\delta\Omega$ is usually Rutherford and the

average number ofsuch scattered particles is

$$\bar{n}_k(x) = Q(\partial\sigma/\partial\Omega)_k \delta\Omega \cdot \rho_k ds \quad , \tag{1}$$

where ρ_k is the atomic density. From energy and momentum conservation, the He energy E_s immediately after scattering is given by

$$E_s = K_k(\varphi) \cdot E_i \quad , \tag{2}$$

where K_k depends on the mass of k but not E_i, thus providing a way to distinguish k. The scattered He experiences an additional energy loss $S_e(x, E_s)$ in leaving the sample. Tilting the sample by an angle θ with our geometry results in the relationship $\frac{ds}{dx} = \sec\theta$ at incidence or $\sec\theta \sec\varphi$ upon egression. The detected energy of a He scattered by an atom k in the sample at a position x can be found by adding up the energy losses along the classical trajectory [7]. This also determines the depth interval ds in the sample corresponding to a particular energy channel of the MCA, and Eqn (1) gives the average number of counts expected in that channel. The quantity $Q\delta\Omega$ was determined for each RBS analysis using the SiO_2 (or Si) substrate as a reference. Q can be obtained by integration of the target current; however, there are uncertainties due to secondary electron and neutral beam effects [8]. The surface approximation was applicable in our samples. The mean concentration of M and Xe in the mixed layer was generally small enough so that their contribution to the energy loss was negligible and the density of the SiO_2 was presumed unchanged. As an application, the mean Ni concentration $[Ni]$ at a depth x in SiO_2 after etching can be related to the number of counts $h_{Ni}(E)$ in channel E of the "Ni spectrum" by

$$\frac{[Ni]}{\rho_{Si}} = \frac{h_{Ni}}{h_{Si}} \frac{(\partial\sigma/\partial\Omega)_{Si}}{(\partial\sigma/\partial\Omega)_{Ni}} \frac{[S]_{Ni}}{[S]_{Si}} \tag{3}$$

$$E = E_o K_{Ni} - [S]_{Ni} \rho_{Si} x \sec\theta \tag{4}$$

where $[S]_{Ni} \simeq K_{Ni} S_e(E_o, SiO_2) + sec(170^0) S_e(K_{Ni} E_o, SiO_2)$,etc.,

where h_{Si} is the height of the Si signal in the "SiO_2 spectrum", ρ_{Si} is the assumed density of Si in SiO_2 ($\rho_{Si} \gg [Ni]$), and E_o is the incident He energy. At 2 MeV, the surface position $E_o K_{Ni}(170^0)$ is 1.52 MeV. $[S]_{Ni}/[S]_{Si}$ is the ratio of stopping factors calculated for He scattering from Ni, Si, respectively, and dissipating energy in the SiO_2 layer . This ratio is ~1.03 and is not sensitive to either Ni or Xe content. The variation in Rutherford cross-section associated with it's E_i^{-2} dependence is less than 2% for He travelling through 100nm of SiO_2. Within this accuracy, the integrated, or sheet concentration of Ni is given by

$$[Ni]_s \equiv \int [Ni] dx = \frac{\sum h_{Ni}}{h_{Si}} \frac{(\partial\sigma/\partial\Omega)_{Si}}{(\partial\sigma/\partial\Omega)_{Ni}} \frac{\delta E_{ch}}{[S]_{Si}} \cos\theta \quad , \qquad (5)$$

where $\sum h_{Ni}$ is the sum over the Ni profile and δE_{ch} is the energy width of one channel. In calculating $[Ni]_s$, h_{Si} was chosen to be the deep Si signal extrapolated to the sample surface. Analogous relations apply to other configurations. A 1 - 10mm^2 area of the sample is typically exposed to the incident He beam. The depth profile inferred from an RBS spectra is therefore an average over this area of the actual distribution of atoms in the sample at a depth corresponding to a given energy loss $E_o K_k - E$.

The depth resolution is limited by noise generated within the detector and preamplifier. Energy straggling of He in the sample contributes a minor uncertainty. These sources add in quadrature since they are uncorrelated. The observed profile $h(E)$ is a convolution of the "actual profile" with a Gaussian noise distribution of variance σ = 9.8 keV (typical). This was readily verified by examining the surface edge corresponding to a thick layer or the profile for a very thin layer. The major problem affecting quantitative profiling was background interference which originated from three principle sources. One

problem was pulse pile-up. This occurs when two or more He are detected within a time interval $\tau \simeq$ 400nsec such that the 572 amplifier cannot distinguish the individual events. A single event with the combined energy is recorded. This produces a high energy tail beyond the Si edge extending from 1.13 to 2.26 MeV, whose magnitude depends linearly on the He current $\dot{\Phi}_{He}$. Experimental measurements and a theoretical discussion are given in Appendix AII.2. He currents below 10nA were required to profile very low Ni levels, resulting in an aquisition time of several hours for sufficient counting statistics. The second problem originated from the use of slits to define the beam. A small portion of the He striking the edges of the first slits is scattered into the sample chamber with a continuous distribution of energy below 2 MeV. This produces a low energy tail on the profile of heavy atoms such as Xe (surface energy 1.84 MeV) which is proportional to the sheet concentration, e.g. $[Xe]_s$. The second set of slits does not prevent some of the scattered He from hitting surfaces within the sample chamber and contributing to the background. The background measured for Xe implanted SiO_2 was roughly constant from 1.25 - 1.5 MeV. This background is superimposed on the metal profile. The background for a particular sample could usually be estimated from the RBS spectra. The third problem was due to impurities such as P in the Si which accumulated at the Si-SiO_2 interface during oxidation. This produced an annoying peak in the energy region used for background estimation. B doped wafers did not exhibit this nuisance.

Thin oxide layers can be measured using the ^{20}Ne resonance in the $^{16}O(\alpha,\alpha)^{16}O$ cross-section at 3.05 MeV. This provides a 30X increase in the sensitivity over the Rutherford cross-section and is specific to ^{16}O [7]. The affect of beam straggling is discussed in reference 9. Accidental channeling of He in the Si substrate presented a difficulty in normalizing $Q\delta\Omega$ for samples on thin oxides. In this case target current integration was resorted to.

The kinematic factor K places a constraint on the types of systems that can be studied without the peaks overlapping. K determines the relative location of each element's surface energy position. Fig. 1 indicates the relationship between atomic number Z and $K(170^0)$ for the first 100 elements [7]. 57% of these elements fall in the interval $0.85 \leq K < 1$, while $K(170^0) = 0.566$ for Si. The first row transition metals occupy much of the intermediate region. Not many systems will give good separation (i.e. $\Delta K \simeq 0.2$) if one chooses to use a heavy ion for mixing. Enhanced separation can be obtained in some cases using the angular dependence of $K(\varphi)$ [7].

2. X-ray Photoelectron Spectroscopy

XPS was performed using the high resolution spectrometer (a modified HP 5950A) at the Jet Propulsion Laboratory, Pasadena. In XPS, the sample is irradiated with mono-energetic x-rays. Chemical information is inferred from the emitted photoelectron energy spectrum. The observed energy of an electron ejected from the k^{th} level of an element in a solid is

$$E = h\nu - E_b(k) - \Phi_{spec} \quad , \tag{6}$$

where Φ_{spec} is the spectrometer work function and $E_b(k)$ is the binding energy. $E_b(k)$ is determined by the potential from the element's nucleus, the potential from surrounding electrons and other nuclei, changes in these potentials due to electronic charge redistribution following ejection of the electron, and the Fermi level position [10]. A change in an element's chemical environment alters the valence electron charge distribution. This alters the potential felt by the core electrons and produces a shift in $E_b(k)$ [10]. Fig. 2 shows the photoelectron spectra for a 25nm Ni film with a native oxide layer. Some of the lines are identified for reference [10-12]. The background steps result from inelastic

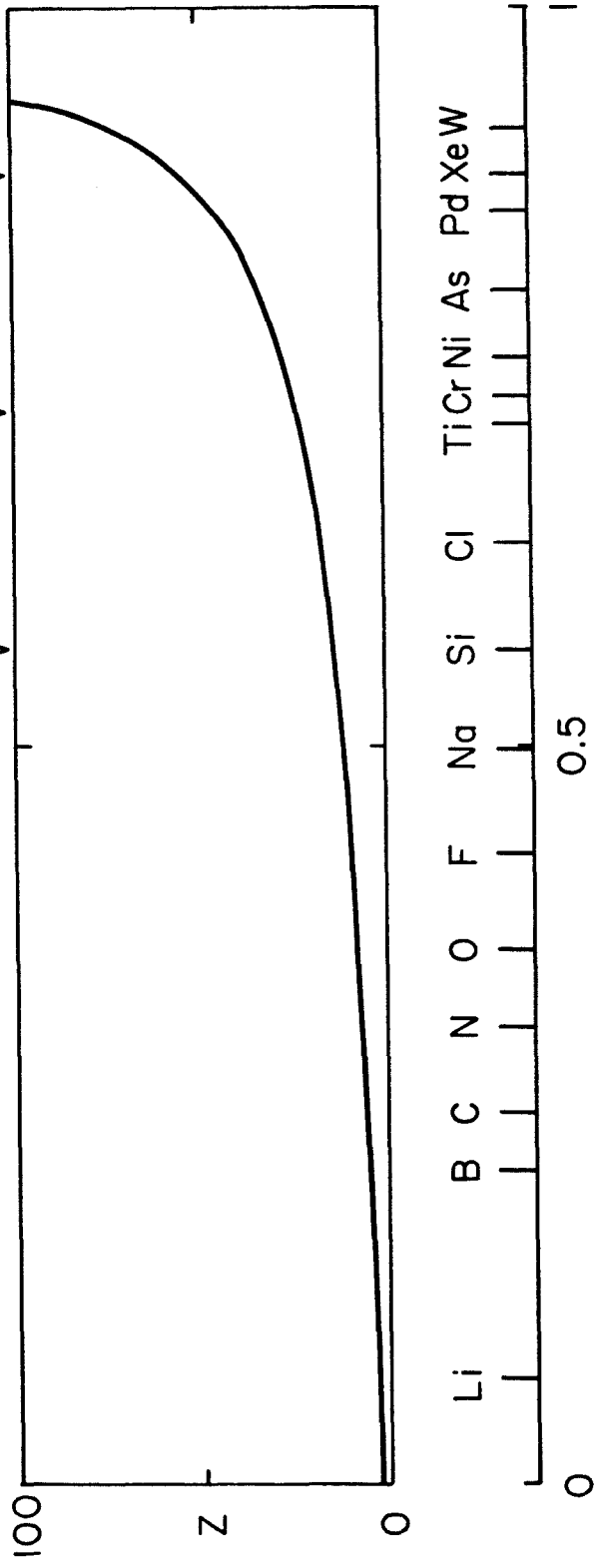

Figure 1. Relationship between kinematic factor K(170°) and atomic number Z.

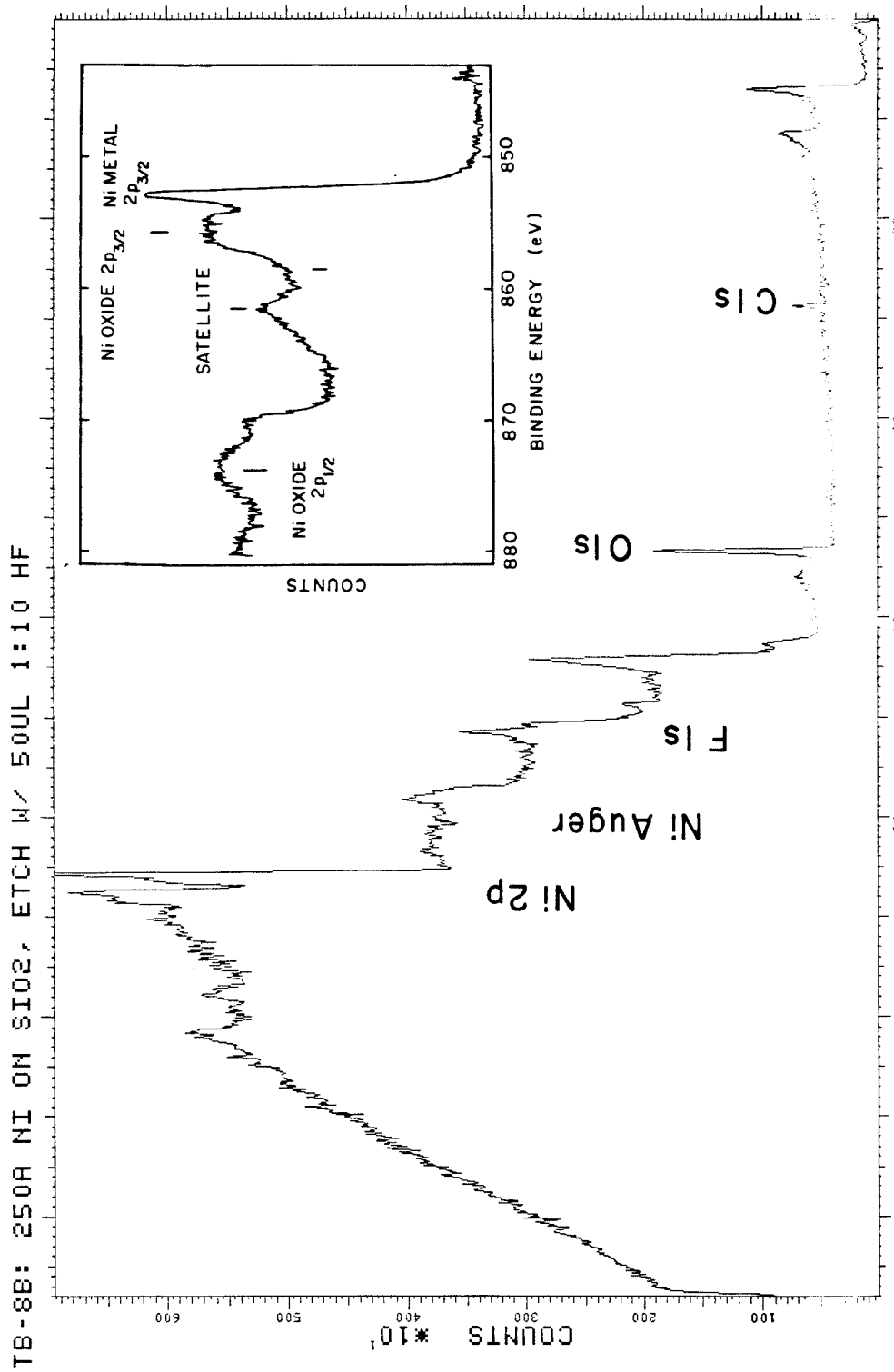

Figure 2. Photoelectron spectra for Ni film with native oxide layer.

scattering. The inset figure shows the Ni lines in greater detail. The Ni metal $2p_{3/2}$ line has an 852.4eV binding energy. Some of these electrons experience a quantized energy loss which may be responsible for an obscured peak at 858.3eV. Oxidation shifts the Ni $2p_{3/2}$ line to 854.5eV in NiO and to 855.8eV in Ni_2O_3 [11-13]. The corresponding $2p_{1/2}$ levels experience the same potential changes. Additional electronic excitation can coincide with the emission of these electrons, resulting in a satellite with higher binding energy like that for Ni oxide at 861.5eV [10].

A 100 - 1000eV electron can typically travel a distance $\lambda \sim$ 1nm in a solid without energy loss [10]. Most of the detected photoelectrons originate from within $\sim 3\lambda$ of the surface. An element's observed photoelectron yield is proportional to an exponentially weighted average of the element's concentration in this region [14]. Chemical depth profiling was accomplished by spin etching using 1:10 HF:ethanol to remove finite sections of the SiO_2 layer [13]. This was done in a dry N_2 chamber. The sample was spun at ~1200 RPM. The etching proceedure consisted of dropwise addition of 1ml ethanol, 0.1ml etchant, and then another 1ml ethanol. The Si 2p (E_b = 102.8eV), O 1s (532.9eV) substrate lines and the pervasive C 1s (285.0±0.2eV) line served as an internal calibration of the binding energy as charge accumulation on the SiO_2 surface produced a 4 - 6V shift in the spectra.

3. Electron Microscopy

Sample thinning and TEM were performed by Dr. Tim Sands at the Lawrence Berkeley Laboratory, Berkeley. The samples were cleaved and two sections were epoxied face to face. These sections then were physically thinned to ~20nm, with Ar ion milling used as the last step. Bright field images were obtained with their 1MV electron microscope. At high resolution, the microscope's

magnification factor was directly calibrated using the lattice fringes from the Si substrate as a reference.

References

[1] D. M. Scott, Ph. D. Thesis, California Institute of Technology, (1982)

[2] S. Matteson, D. G. Tonn and M-A. Nicolet, *J. Vac. Sci. Technology* **16**, 882 (1979)

[3] W. J. James and M. E. Straumanis in *Encyclopedia of Electrochemistry of the Elements Vol. V*, A. J. Bard, ed. (Marcel Dekker, New York, 1976), Ch. 7

[4] H. V. K. Udupa and V. K. Venkatesan in *Encyclopedia of Electrochemistry of the Elements Vol. II*, A. J. Bard, ed. (Marcel Dekker, New York, 1974), Ch. 3

[5] D. A. Skoog and D. M. West, *Fundamentals of Analytical Chemistry* (Holt, Rinehart and Winston, New York, 1976), 346

[6] C. H. Rochester, *Acidity Functions* (Academic Press, New York, 1970)

[7] W-K. Chu, J. W. Mayer and M-A. Nicolet, *Backscattering Spectrometry* (Academic Press, New York, 1978)

[8] S. Matteson and M-A. Nicolet, *Nucl. Instr. and Meth.* **160**, 301 (1979)

[9] X-A. Zhao, T. C. Banwell and M-A. Nicolet, to be published in the proceedings of SPIE 1986 Spring Meeting.

[10] C. R. Brundle in *X-Ray Photoelectron Spectroscopy*, T. A. Carlson, ed. (Dowden, Hutchinson and Ross, Stroudsburg, 1978), 212

[11] K. S. Kim and R. E. Davis, *J. Elect. Spectrosc. and Related Phenom.* **1**, 251 (1972/1973)

[12] N. S. McIntyre, T. E. Rummery, M. G. Cook and D. Owen, *J. Electrochem. Soc.* **123**, 1164 (1976)

[13] P. J. Grunthaner, Ph. D. Thesis, California Institute of Technology, (1980)

[14] C. S. Fadley, R. J. Baird, W. Seikhaus, T. Novakov and S. A. L. Bergstrom, *J. of Electron Spectrosc.* **4**, 93 (1974)

Chapter III Characterization of Ion mixing in M/SiO_2

Prelude

Experimental results which were useful in identifying the various processes affecting the ion mixing of metal M and SiO_2 are discussed in this chapter. Several models which are useful for interpreting these results are developed in the following chapters. We shall confine our present discussion to general principles as best we can. The investigation of M-SiO_2 mixing involved many separate experiments. Most of the experiments utilized metal films on thick SiO_2 layers (~1μm) and 290keV Xe irradiation. These conditions are implied if they are not otherwise specified.

A. General Behavior

RBS spectra for 25nm Ni (a) and 73nm Ti (b) films on ~1μm SiO_2 after irradiation at 25C with $4x10^{15}$ cm^{-2} and $6.7x10^{15}$ cm^{-2} 290keV Xe, respectively, are shown in Fig. 1. The solid lines represent the samples prior to irradiation. The steps at 0.6 and 1.1 MeV are from the SiO_2, while the peak near 1.4 - 1.5 MeV is from the metal film. Although there is a discernable difference after irradiation, the amount of mixing is very small compared to that seen for M-M and M-Si systems where diffusion tails or new steps are observed [1]. Identical results were also obtained for irradiated V, Cr, Fe, Co, and Pt films on SiO_2.

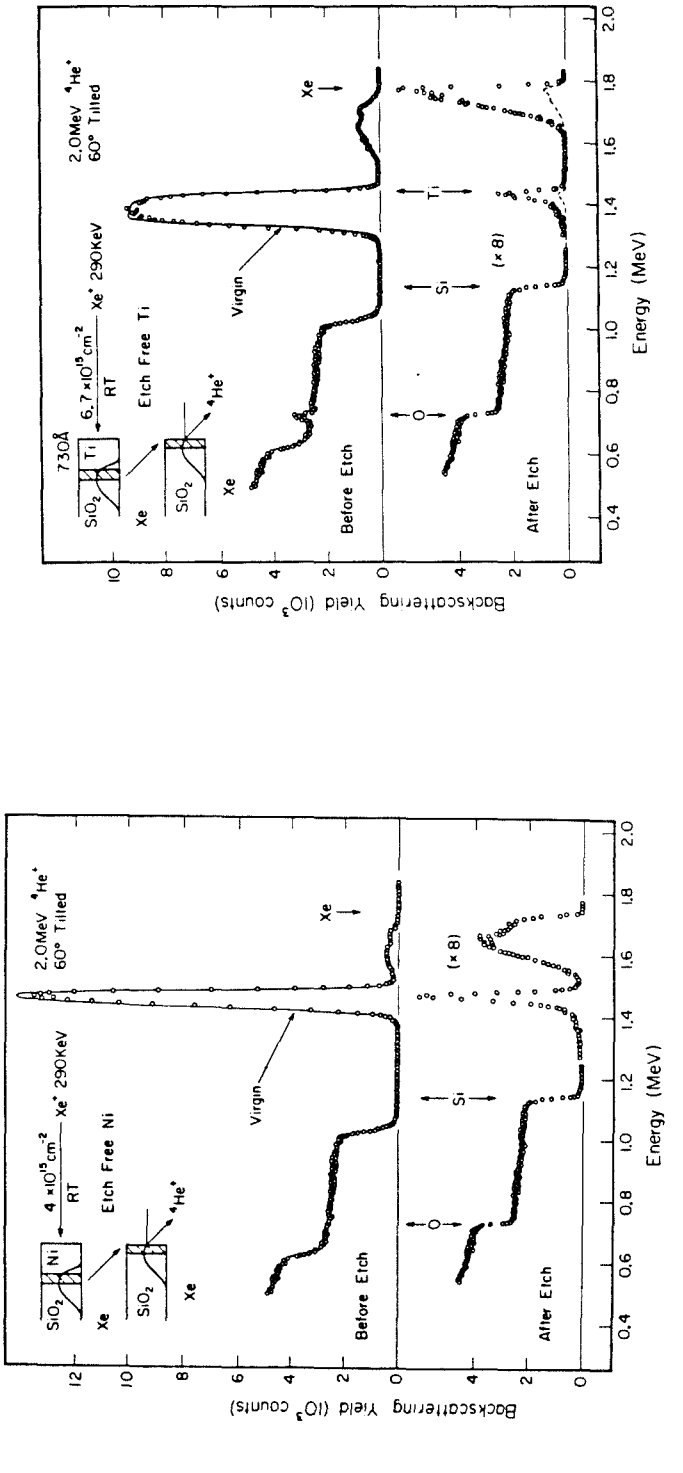

Figure 1. RBS profiles for (a) Ni and (b) Ti samples before (solid lines) and after 290 keV Xe irradiation at 25°C.

B. A Closer Look With TEM and XPS

1. Ni/SiO_2

Fig. 2 shows a bright field cross-sectional TEM image of a 25nmNi/SiO_2 sample after irradiation with $6x10^{15}$ cm^{-2} Xe at 25C. The atomic profiles from RBS and the depth scale are also shown. The dark region corresponds to the Ni film. The contrast is insufficient to distinguish an intermixed region. The waviness is a microscope aberration [2]; the metallurgical interface appears smooth and the Ni film remains uniform. A high-resolution TEM image of this implanted Ni sample after removal of the free Ni is shown in Fig. 3 with the corresponding Ni and Xe RBS profiles. The two arrows identify the SiO_2 surface. The dark clusters again correspond to Ni. There is a significant discontinuity in the Ni distribution at the interface, which is not expected for regular diffusion. Most of the apparent Ni is located within a 5nm region centered 5nm below the SiO_2 surface. The RBS profile shows a similar Ni disribution, however, the shape of the convoluted peak is dominate by the Gaussian (FWHM $\simeq$ 21nm) spectrometer noise density. This Ni is contained in clusters with a typical diameter of 2.1±0.5nm. Ni is not evident in the 3nm region adjacent to the interface. The slowly varying RBS tail beyond 30nm is physically significant (recoil tail). Ni clusters are also apparent in this deep tail region. Fig. 4a shows a high-resolution TEM image of the clusters near the surface of the sample examined in Fig. 3. The lattice fringes indicate that the clusters are crystalline. The boxed region is shown in Fig. 4b with greater magnification. The most common plane spacing observed in the crystalline clusters is d = 0.241±0.004nm. Clusters were occassionally observed in a low index orientation (crossed fringes). The orientation of the cluster in Fig. 4b is near <110> [2]. Crossed {111} planes are visible. These observations suggest that the clusters have cubic, probably fcc, structure with

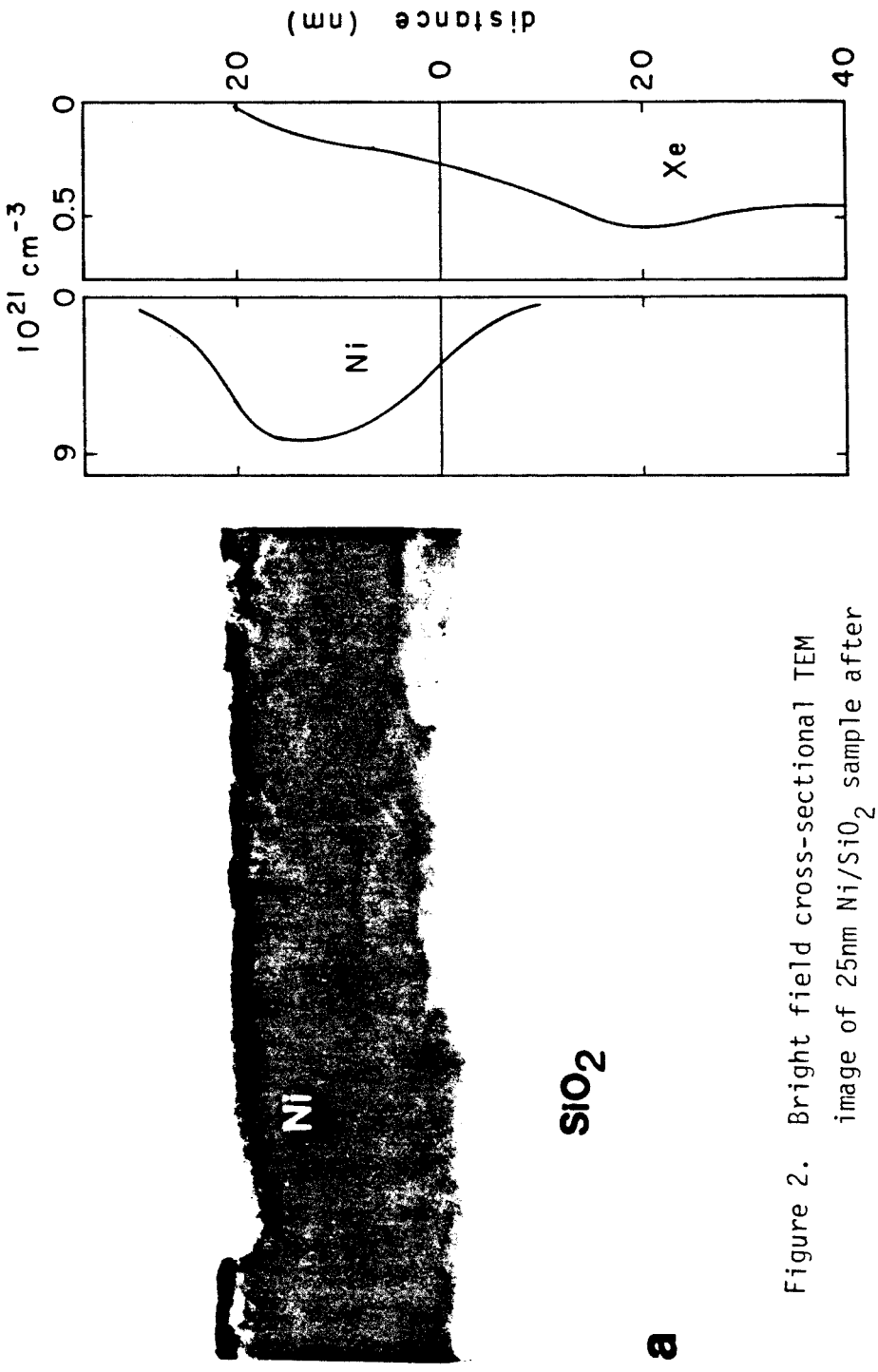

Figure 2. Bright field cross-sectional TEM image of 25nm Ni/SiO_2 sample after irradiation with 290keV Xe.

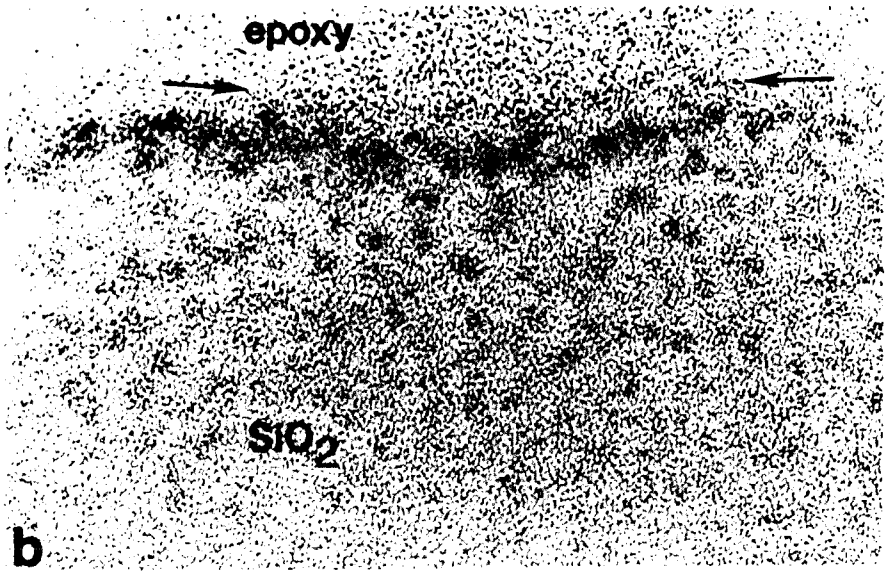

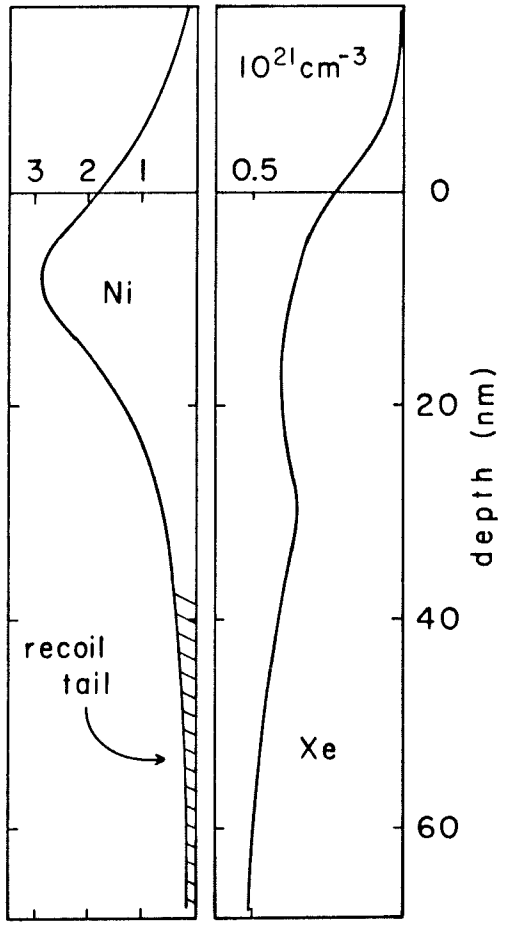

Figure 3. High-resolution image of sample shown in Figure 2. after removing free Ni layer.

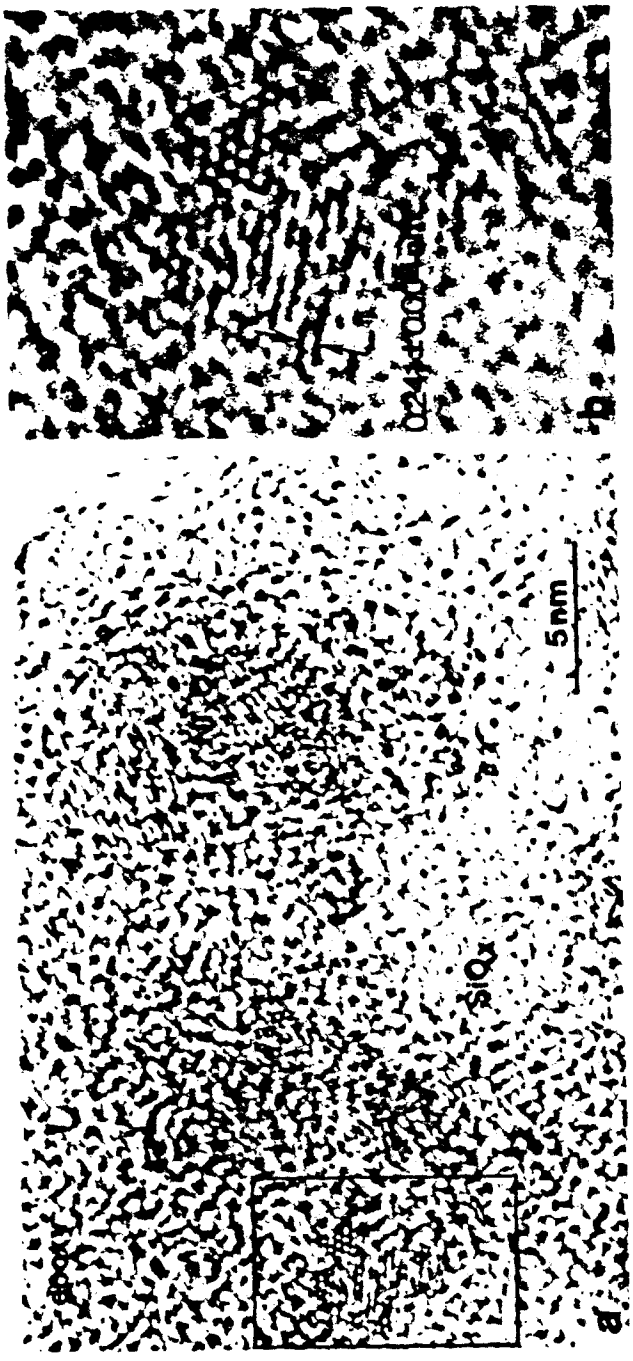

Figure 4. (a) High-resolution image of Ni clusters in SiO_2. Boxed region is shown in (b) with greater magnification.

$a_0 = \sqrt{3}d_{111} = 0.417\pm0.007$nm. The characteristics of some relevant Ni compounds are given in Table 1. The structure and lattice parameter of the clusters closely resemble the reported values for two nickel oxides; the high temperature polymorph of NiO, and possibly Ni_2O_3 [3,4]. A 2nm diameter cluster would contain ~300 NiO molecules. Additional Ni phases are not discernable, nor is the implanted Xe.

The histogram in Fig. 5 shows the depth distribution of the clusters in Fig. 3. An 82nm x 2nm window was used for the counting. The corresponding Ni RBS profile is reproduced by the dotted line. The thickness of the thinned sample, estimated to be ~20nm, is much larger than the cluster diameter; consequently, compensation must be made for cluster overlap. The calculated peak cluster density is $2x10^{19}$ cm^{-3}.

Fig. 6a shows a sequence of Ni 2p photoelectron spectra from a chemical depth profile of a 25nm Ni/SiO_2 sample irradiated at 25C with $15x10^{15}$ cm^{-2} Xe. The unreacted Ni film was previously removed. A single $Ni2p_{3/2}$ peak is evident at 853.6±0.3eV binding energy with a FWHM of 1.6eV. A satellite is apparent 4.4eV higher at 858eV. The relative heights and peak positions do not change significantly with depth. The depth profile obtained by plotting the intensity of the 853.6eV line versus etchant volume, Fig. 6b, qualitatively agrees with the Ni profiles from TEM and RBS. The prominent shake-up satellite is characteristic of Ni oxide [5] The Ni $2p_{3/2}$ peak lies 0.9 and 2.2eV lower than that of bulk NiO and that proposed for Ni_2O_3, respectively [5,6]. The binding energy in small clusters differs from the bulk value due to initial and final state effects which depend on the interaction of the clusters with the supporting substrate [7,8]. A 0.9eV shift can be associated with the formation of clusters. The clusters are most certainly NiO. Kelly suggests that this is to be expected from thermodynamic considerations [9]. Xe $3d_{5/2}$ and $3d_{3/2}$ peaks were present with binding energies of

Table I. Structures of some selected nickel compounds

Compound	Structure	Lattice parameters a_0	c_0	C	Comments	Ref*
Ni	fcc	3.524				[19]
NiO	rhombo.	7.594	7.236	2.450	low temp.	22-1189
NiO (Bunsenite)	fcc	4.1769			hi temp.	4-835
Ni_2O_3	hexagonal	4.61	5.61	1.22		14-481
Ni_2O_3	fcc	4.186				[3]
Ni_2SiO_4	cubic	8.045			hi press.	15-255
$NiSi_2$	cubic	5.395				[19]
$NiSi_2$ - θ	hexagonal	3.805	4.890	1.291	hi temp.	[19]
Ni_3Si - β_1	cubic	3.5040				[19]

*Powder Diffraction File number

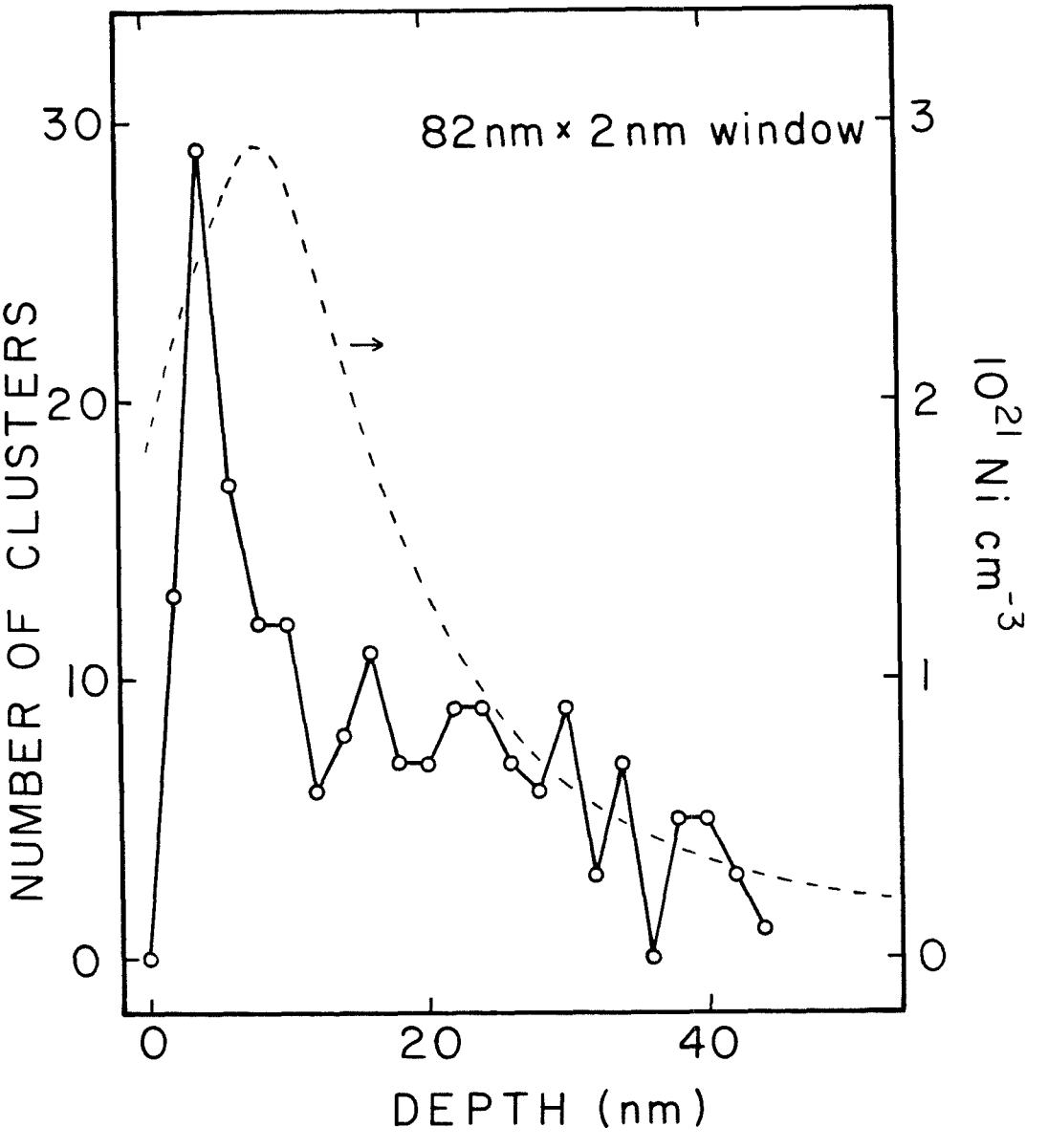

Figure 5. Depth distribution histogram for Ni clusters in Figure 3.

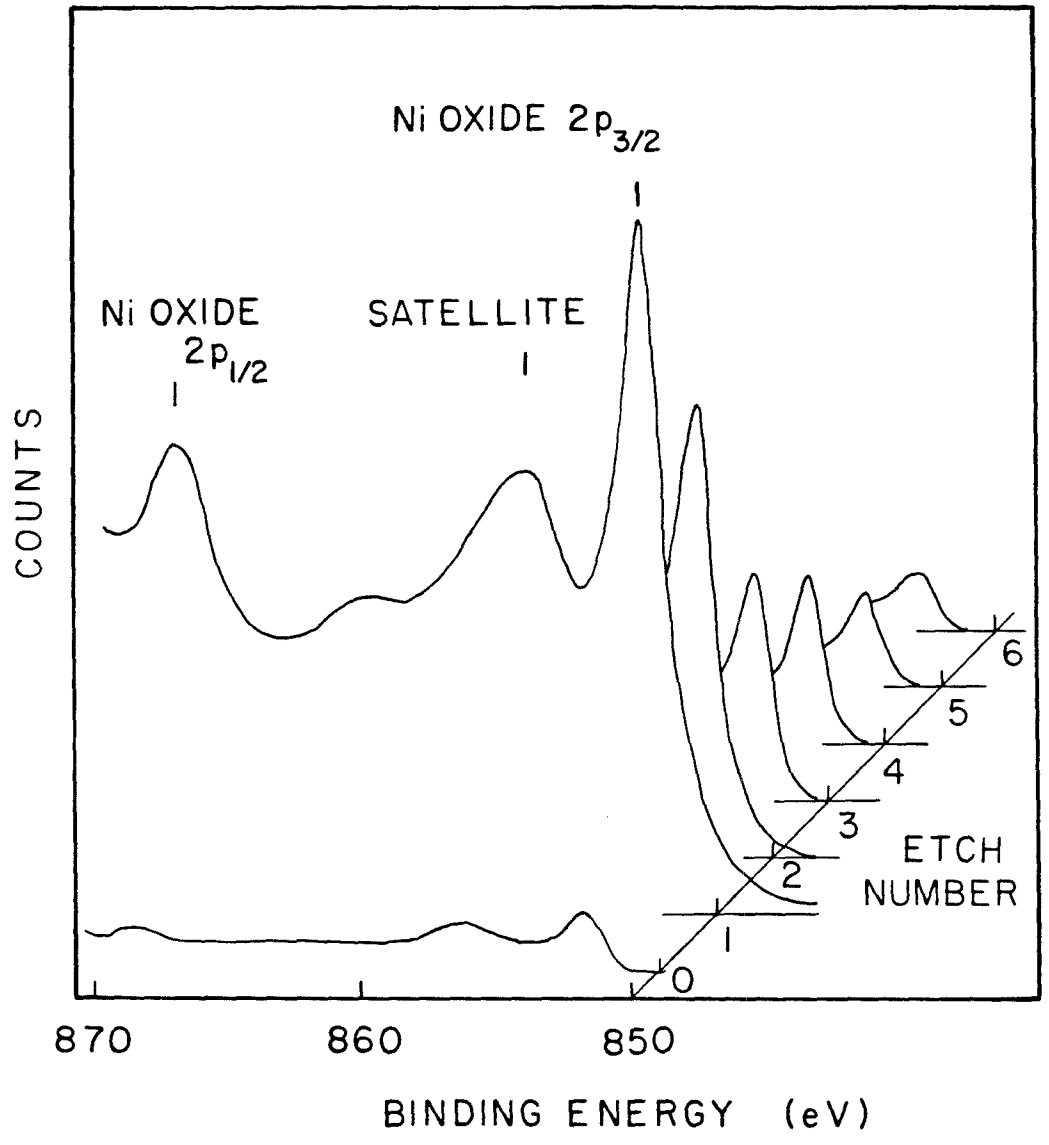

Figure 6a. Sequence of Ni 2p photoelectron spectra for a chemical depth profile of a 25nm Ni/SiO_2 sample irradiated at 25°C with $15x10^{15}$ cm^{-2} 290 keV Xe. The free Ni was previously removed.

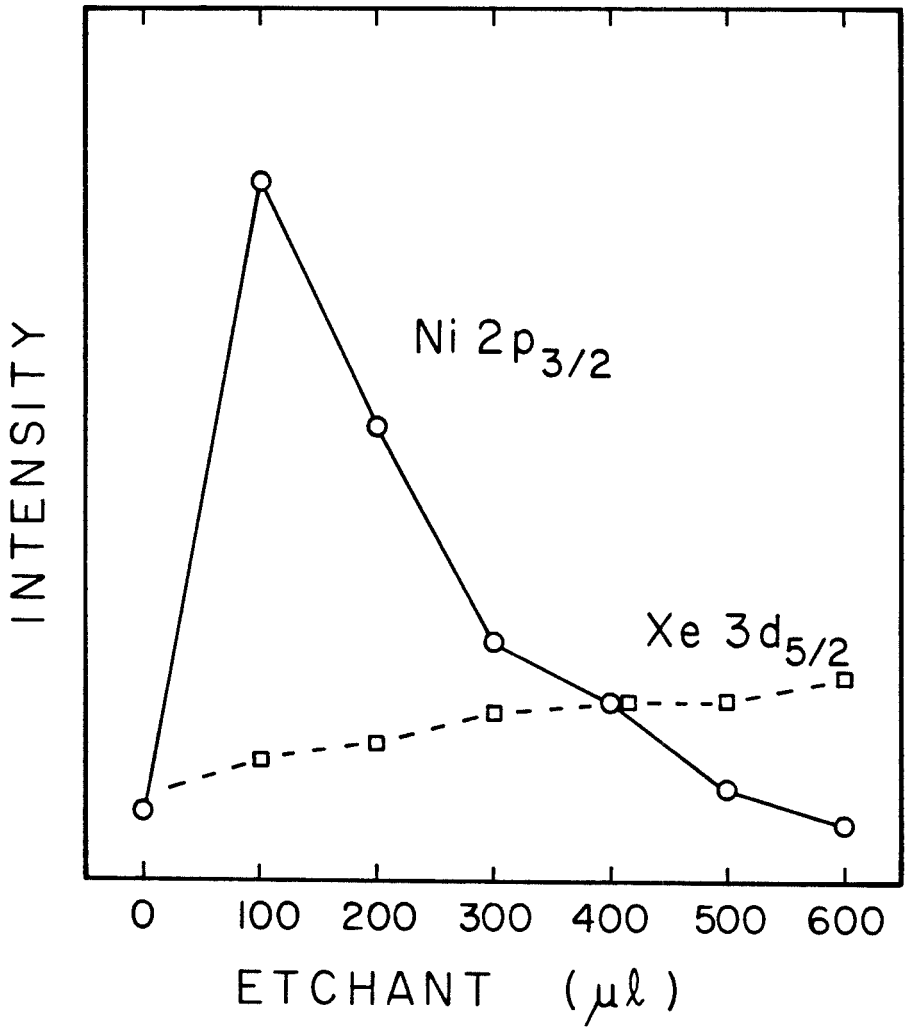

Figure 6b. Graph of Ni $2p_{3/2}$ and Xe $3d_{5/2}$ peak intensities versus etchant volume.

669.6±0.3 and 682.3eV, respectively. The Xe $3d_{5/2}$ intensity profile is also reported in Fig. 6b and resembles the RBS Xe profile in Fig. 5 as well.

O 1s and Si 2p spectra are shown in Fig. 7a,b respectively, for the sample of Fig 6. There is a low binding energy tail on the O 1s peak which could be deconvoluted into two Gaussian profiles as shown using numerical fitting. The two peaks are separated by 2eV and both have a FWHM of 1.7eV. The dominant peak coincides with the O 1s spectra for an SiO_2 blank. The small peak is probably from NiO. The depth profile of this peak followed that of the Ni. The ratio of the average concentrations $[O\ in\ NiO]/[O\ in\ SiO_2]$, which is given by the ratio of the corresponding peak areas, had a maximum value of 0.12. The peak value of the ratio $[Ni]/[Si]$ estimated by RBS was 0.2. These agree within 20% for NiO in SiO_2. The Ni $2p_{3/2}$ core levels for the Ni silicides also have binding energies in the range 853 - 853.5eV; however, the shake-up satellite is absent [10]. The tail on the Si 2p spectra in Fig. 7b is attributed to a small peak with a 101eV binding energy. This is significantly higher than the value of ~98.8eV observed for the Si 2p levels in the Ni silicides [10].

2. Ti/SiO_2 and Cr/SiO_2

Cross-sectional TEM micrographs for irradiated and etched Cr/SiO_2 and Ti/SiO_2 samples are shown in Fig. 8a and b respectively. The Cr samples show no evidence of crystalline phase formation or clustering. TEM would probably reveal crystalline phases if present. TEM is not sensitive, however, to the Cr distribution if it is disordered as the electron scattering factor for Cr is not significantly different from that for Si. The Ti samples exhibit considerable structure. There are 13 - 25 nm diameter particles at the surface which show a lattice plane spacing of 0.33±0.01 nm. This corresponds to a strong reflection in several titanium oxides. The particles are not metallic Ti, although it is also

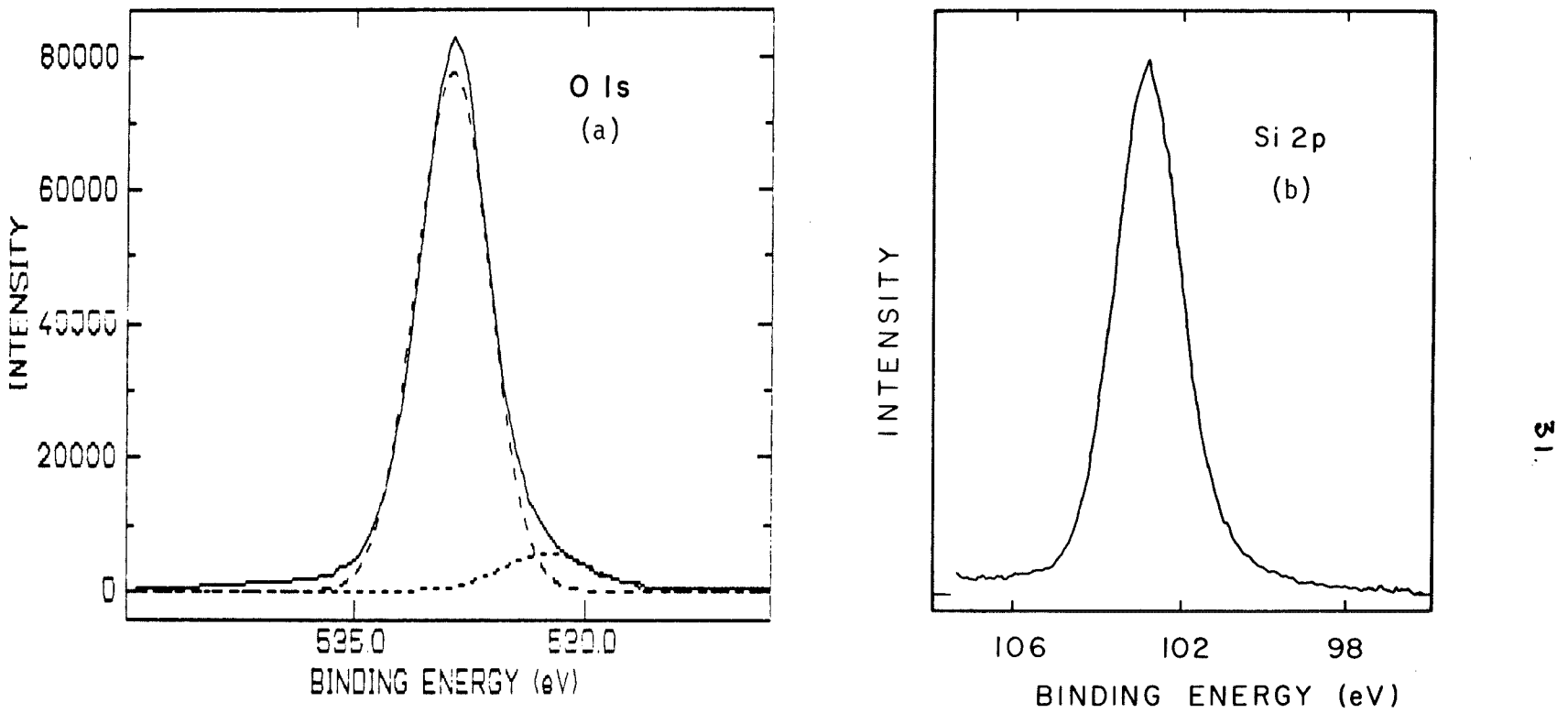

Figure 7. (a) O 1s spectrum for the sample of Figure 6 after etch number 1. Component Gaussians from a numerical fit are also indicated by broken lines.
(b) Si 2p spectrum for same sample.

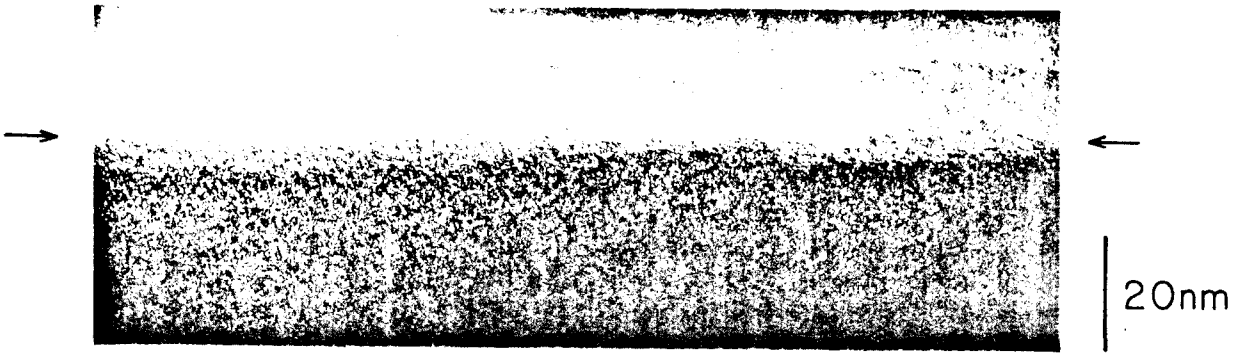

Figure 8a. TEM image for irradiated Cr/SiO_2 sample after etching.

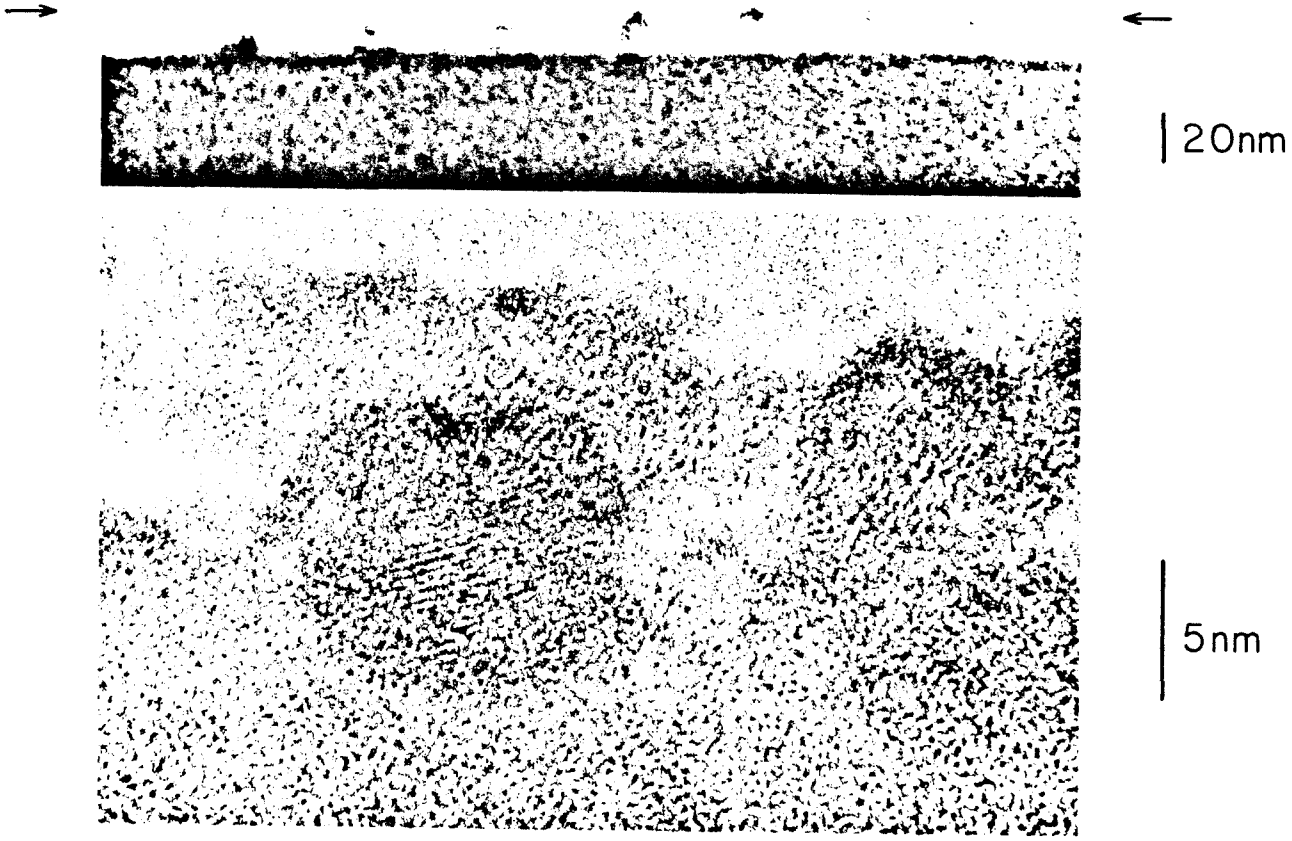

Figure 8b. (Top) TEM image for irradiated Ti/SiO_2 sample after etching. The arrows indicate the surface of the SiO_2.

(Bottom) Higher resolution image of Ti bearing clusters apparent in previous micrograph.

possible they are $TiSi_2$ [2]. There is ,in addition, a band of amorphous or partially crystalline material centered at a depth of ~10 nm which probably contains Ti.

C. Comparison of Ti, Cr and Ni Mixing Rates

A set of Ti, Cr and Ni samples on ~1μm SiO_2 were prepared with three different film thicknesses chosen for each metal corresponding to $R_p/2$, $R_p - \Delta R_p$, and R_p, where R_p is the projected range and ΔR_p is the standard deviation in the projected range of 290keV Xe in the metal (34 and 11.5μg cm^{-2}, respectively) [11]. RBS profiles of Ti, Cr and Ni in the SiO_2 after etching are shown in Fig. 9 for a ~23μg cm^{-2} film thickness (47, 33, and 26nm, respectively) and a 10x10^{15} cm^{-2} Xe fluence. The metal concentration $[M]$ is plotted logarithmically versus SiO_2 depth x. The profiles consist of two distinct parts. Most of the metal is contained in a resolution limited peak near the surface. In contrast to the Ni bearing region which lies below the SiO_2 surface, Ti and Cr may extend to the surface monotonically. The peak is most pronounced for Ni and least for Ti. The peak concentrations are less than 5% of the densities in the respective metals. A large discontinuity is sustained across the M-SiO_2 interface. The deep tails extending beyond the ~40nm result from recoil implantation [12]. The distribution of relocated atoms displaced by high energy collisions with the incident ion is approximately exponential (linear in a log plot). This is the topic of chapter V. The recoil tails are similar, as these metals are close in atomic number. The resolution of the tail beyond ~120nm is restricted by interference from background counts. Both the peak and tail were seen in all of the irradiated samples, although with differing proportions. Samples irradiated at -196C where indistinguishable from the 25C samples.

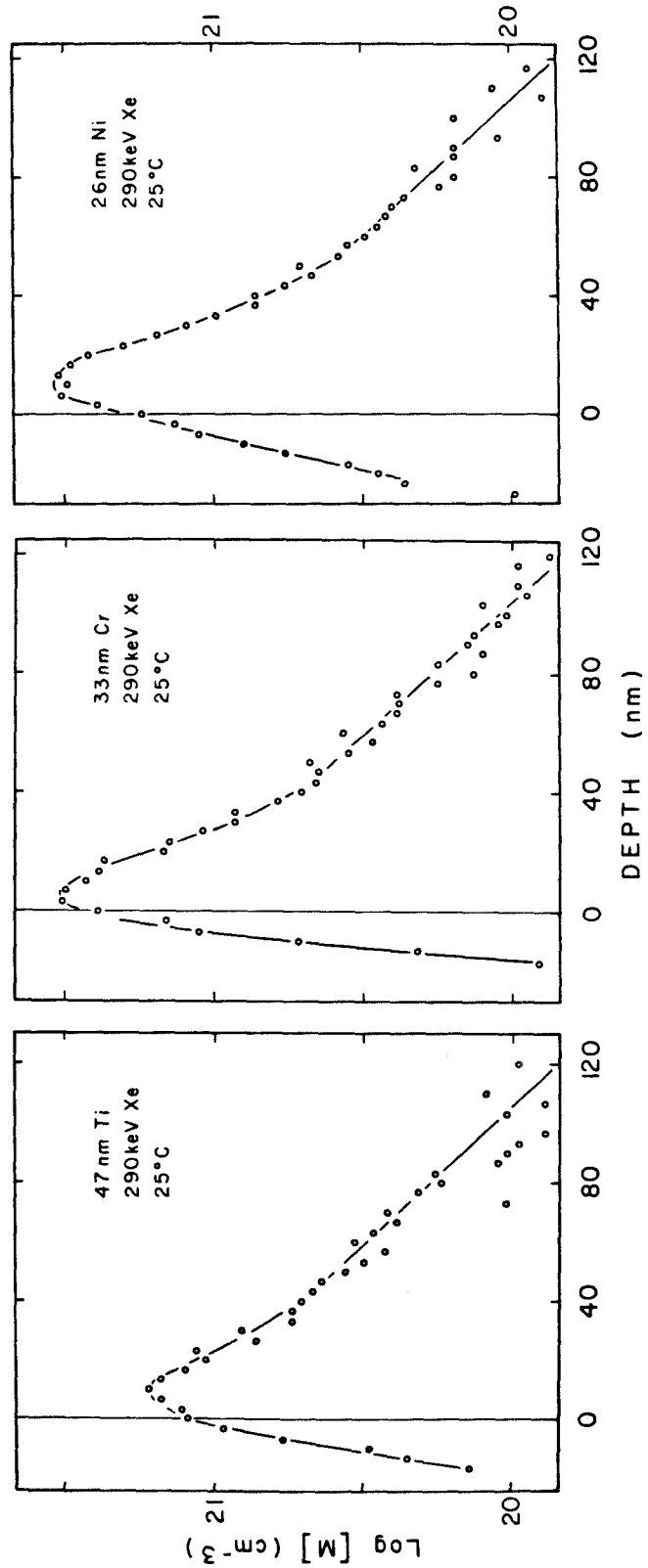

Figure 9. RBS depth profiles of Ti, Cr and Ni in SiO_2 produced by $10x10^{15}$ cm^{-2} Xe irradiation. The free metal was previously removed.

The areal density of M atoms incorporated in the SiO_2, $[M]_s = \int [M]\,dx$, was measured as a function of the Xe fluence Φ. $[M]_s$ will have at least two components. Independent events such as recoil implantation will introduce a Φ^1 dependence. The random walks associated with cascade mixing will have a $\Phi^{1/2}$ contribution. A first order approximation is therefore

$$[M]_s \sim \mathbf{A}\Phi^{1/2} + \mathbf{R}\Phi \quad . \tag{1}$$

Division by $\Phi^{1/2}$ yields a linear relationship in $\Phi^{1/2}$;

$$[M]_s\,\Phi^{-1/2} \sim \mathbf{A} + \mathbf{R}\Phi^{1/2} \quad . \tag{2}$$

The two contributions can be visually distinguished by plotting $[M]_s\,\Phi^{-1/2}$ versus $\Phi^{1/2}$. Fig. 10 shows the mixing at 25C for the three different thicknesses of Ti, Cr and Ni over a Xe fluence range of 1 - 15×10^{15} cm^{-2}. The relative variation in film thickness produced by sputtering was minor for films with ~23μg cm^{-2} or more of metal. Sputtering was significant in the 16μg cm^{-2} samples for $\Phi > 5 \times 10^{15}$ cm^{-2}, as indicated by the appearance of a step in the Si profile corresponding to exposed SiO_2. The mixing behavior for Ni and Ti closely follows Eqn. 2. There is a negative deviation for those samples showing signs of significant sputtering. The scatter in the Cr results is attributed to the difficulty in etching Cr. Surface oxidation inhibited etching of several implanted Cr samples. The trend in the Cr results also seems to follow Eqn. 2.

Two correlations are apparent. The mixing is greatest when the film thickness is ~$(R_p - \Delta R_p)$, and it falls off with larger or smaller values. A low sensitivity to variations in film thickness or ion energy should occur with this sample configuration. A convenient measure of the relative mixing rate is provided by the area

$$Q_M = \int_1^S ([M]_s\,\Phi^{-1/2})\,d(\Phi^{1/2}) \tag{3}$$

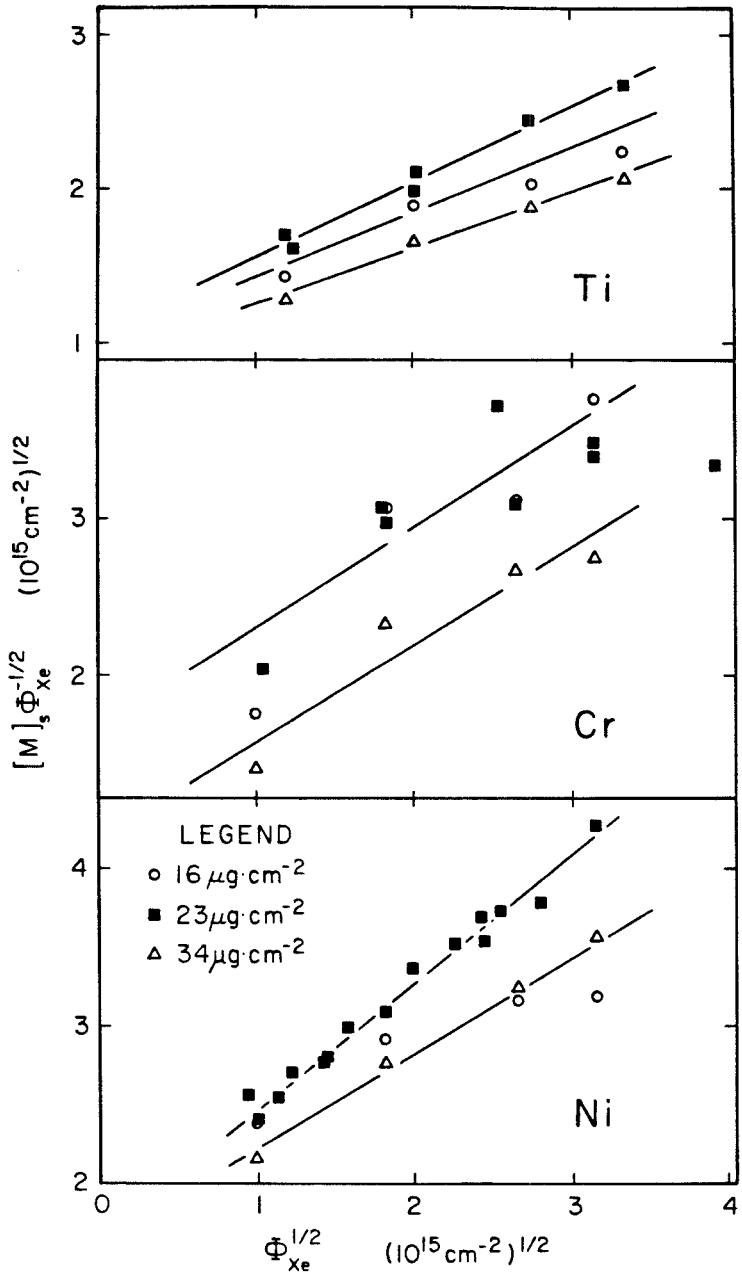

Figure 10. Dose dependence of mixing at 25°C for three different thicknesses of metal on SiO_2 irradiated with 290keV Xe.

within the interval $1x10^{15}$ $cm^{-2} \leq \Phi \leq 9x10^{15}$ cm^{-2}. This is equivalent to averaging $[M]_s$ with the weighting function Φ^{-1}. Fig. 10 suggests that the variation in Q_M with Φ primarily reflects the difference in the diffusional component referred to in Eqn. 1. Q_M was calculated from the lines fitted to the data in Fig. 10, and the results plotted in Fig. 11 against the energy deposited in the metal per incident Xe ion per unit depth (F_D), at a depth corresponding to the position of the M-SiO_2 interface [11]. A gaussian distribution was assumed. Results from later experiments are also included (open symbols). The linear correlation in Fig. 11 is often observed [1]. The principle difference between Ti, Cr and Ni seems to be more strongly associated with ballistic effects, rather than with thermochemical considerations.

Thermochemical effects are known to play a role in biasing the random walk process of mixing in metallic systems induced by dense cascades [13]. Mixing in these systems is enhanced when the heat of mixing $\Delta H_{mix} < 0$. The chemical reactivities of Ti, Cr and Ni with SiO_2 are very different [14]. Many reactions of Ti with SiO_2 are thermodynamically favorable, although segregated $TiSi_2$ and Ti_2O_3 layers are the observed reaction products for annealing above 670C. Ti provides a diffusion path, allowing oxygen transport away from the reaction zone. There are two favorable reactions of Cr with SiO_2 , both forming Cr_2O_3 [14], which is renowned for its passivation behavior. The equivalent of approximately one monolayer of Cr_2O_3 remains after etching a Cr/SiO_2 sample annealed above 670C. There are no favorable reactions of Ni with SiO_2. Ni films tend to coalesce into islands at high temperatures. The 3nm depleted region seen with Ni is consistent with the thermal behavior. These considerations explain the reactivity observed with thermal annealing [14], but are superceded by other considerations in ion mixing. Q_M for the mixing of Cr and Ni with Si is ~5 - 13X greater than with SiO_2. Oxygen suppresses mixing in these ternary systems with equal

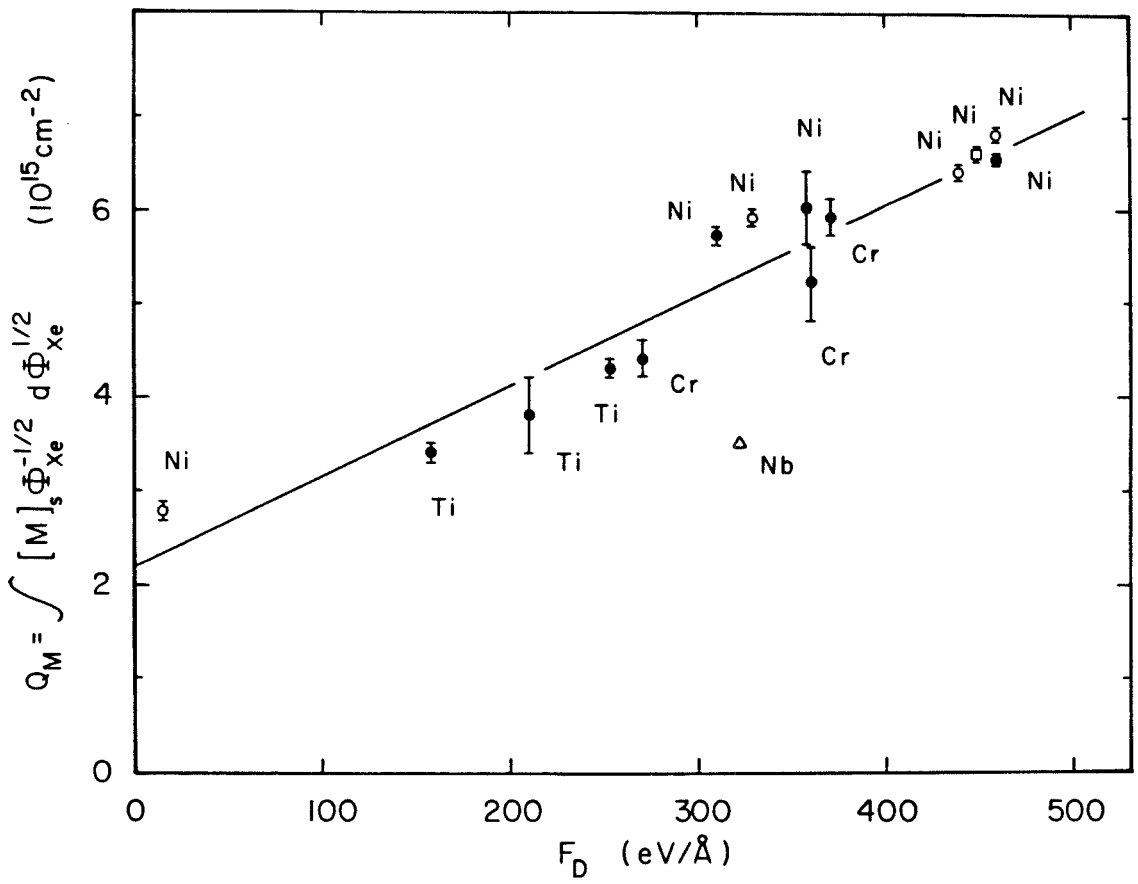

Figure 11. Graph of Q_M versus deposited energy F_D .

efficiency. This leads us to believe that kinetic constraints associated with the ternary nature of the M-SiO_2 system inhibit ion mixing.

D. Analysis of Ni Profile Evolution

1. General Trends

Continuing on our way, Fig. 12 shows the Ni RBS profile for 25nm Ni/SiO_2 samples irradiated at either 25, 300, or 500C with a Xe fluence of 6 - 6.5x10^{15} cm^{-2}. The unreacted Ni was removed. $\log[Ni]$ is plotted versus depth x. The temperature dependence for Ti and Cr are very different and are discussed in Appendix AIII.2. As previously noted, there is little structure evident in the resolution limited, nearly gaussian, peak adjacent to the interface. The peak is diminished at elevated temperatures by the suppression of net short range mixing. A portion of the low temperature mixing prevails relatively unchanged at 500C. The recoil tail beyond ~40nm is slightly affected by the implantation temperature. The 10% lower Φ is partially responsible for the reduction of the profile at 500C. The outward shift in the tails at 25, 300C produced by the He energy loss in the Ni represented by the large peak is ~1nm. The Ni $2p_{3/2}$ photoelectron spectra for these samples were similar in structure to those previously shown.

Most of the information about the mixing process is contained in the peak which we can not resolve with RBS. Microscopy is far too tedious for a parametric study. There is usually some promise in asking simpler questions. Our strategy will be to characterize the yield and slope of the deep tail which is discernible. The total Ni yield is not affected by the spectrometer resolution. The first spatial moment $\int[Ni]x\,dx$ can also be extracted from the spectra. The higher moments are too heavily biased by the tail to be useful. RBS spectra

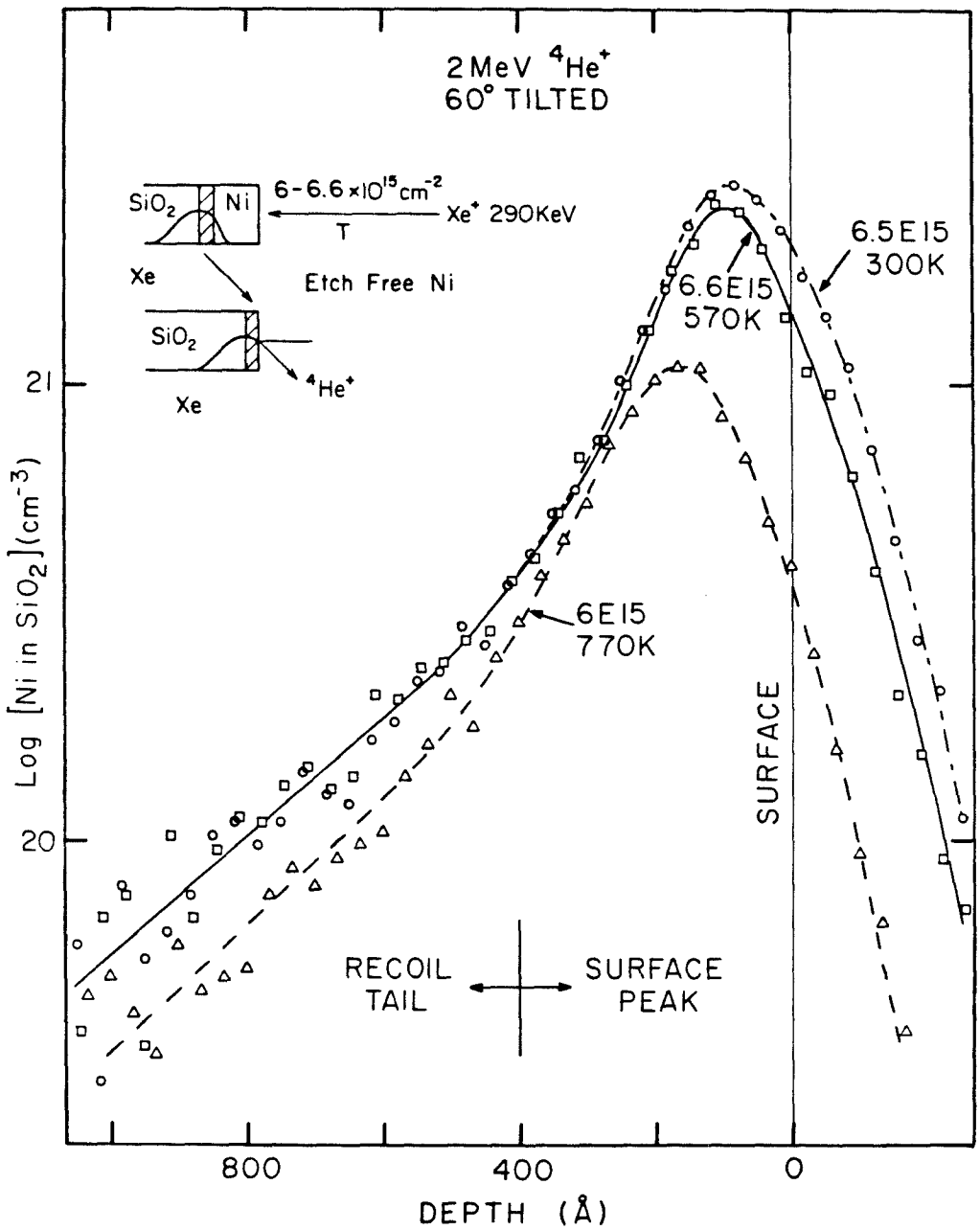

Figure 12. Ni RBS depth profiles for 25nm Ni/SiO_2 samples irradiated at the temperature indicated.

were taken for 25nm Ni/SiO_2 samples irradiated at various temperatures T with 290keV Xe fluences Φ in the range 0.01 - $10x10^{15}$ cm^{-2}. This is a considerably larger range that most ion mixing experiments can utilize.

2. Recoil Tail

The recoil tail was subjectively defined as the deep linear portion of the $\log[Ni]$ profile, generally in the region ~35nm to ~100nm. The background was estimated from the flat portion of the spectra beyond this interval. The tails were characterized by a linear least squares fit, with the constraint that $\int_{tail}[Ni]dx$ be preserved. The fitted line was used to extrapolate the tail to the surface. This approach accommodates regions of differing size. The areal density of Ni contained in the extrapolated profile is plotted in Fig. 13 versus Φ. The origin has been displaced for each temperature. The extrapolated area, which reflects only the tail, has a linear Φ dependence as expected for recoil implantation. The difference at 500C is again apparent. This is probably not an etching artifact, becouse the peak at ~20nm in Fig. 12 is not commensurately displaced. The decay length l corresponding to the slope of the tail, $\frac{1}{l} = -\frac{\Delta \ln[Ni]}{\Delta x}$, has the Φ dependence shown in Fig. 14 for the various T. The irradiation temperature and dose do not have a large effect on the value of $l \simeq$ 33nm. The uncertainty in calculating l from the tail is ±7%. However, the trend in l for $\Phi < 2x10^{15}$ cm^{-2} is probably due to interference from the dominating peak. The theoretical estimate (Chapter V) of the extrapolated yield for primary Ni recoils is 0.60. l is estimated to be 32nm by this calculation. Appendix AIII.1 shows that resolution broadening produces a small displacement in the deep exponential tails, which increases the apparent yield by 5%. Cascade mixing may also produce noticeable distortion in the deep tail ($x > l$) when subsequent RMS displacement of the incorporated Ni atoms $\sigma^2(\Phi) \simeq l^2$ (Appendix AIV.1). A very high fluence is

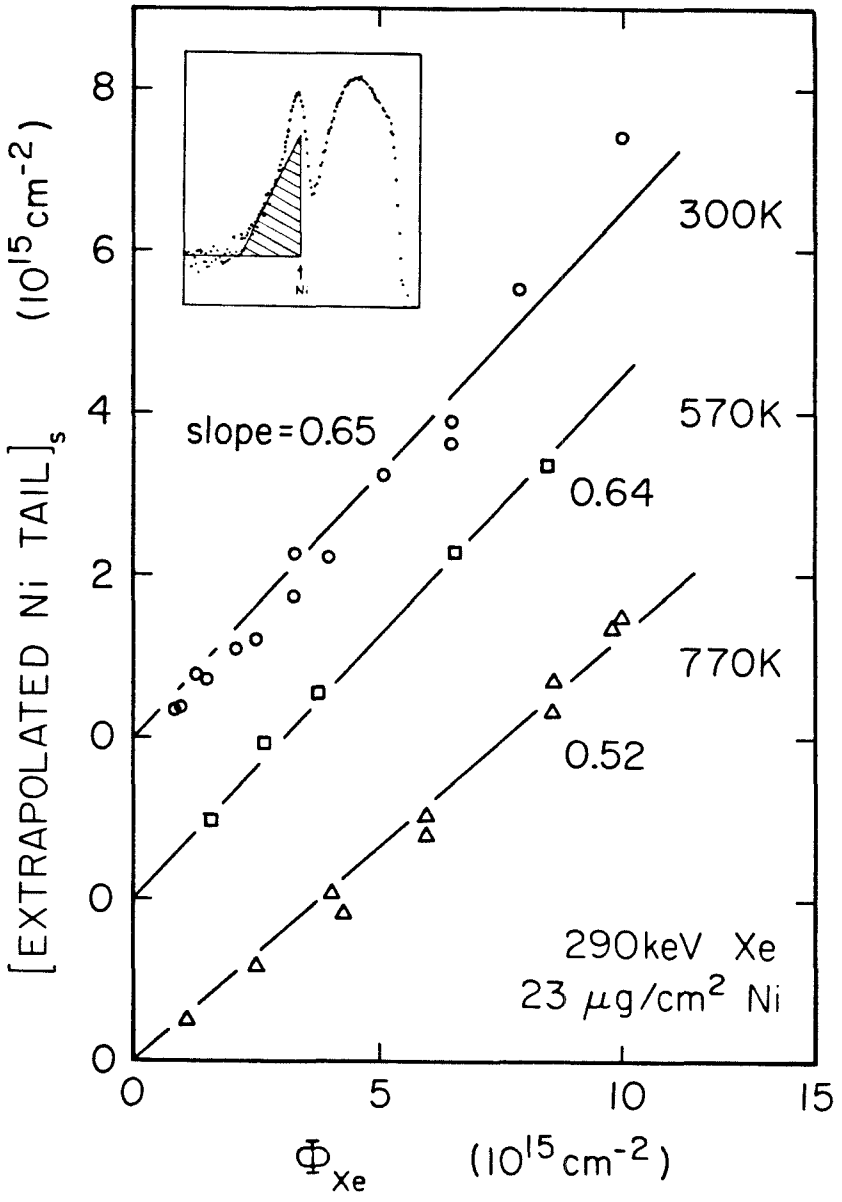

Figure 13. Graph of Ni areal density in extrapolated deep tail versus Xe fluence for 25nm Ni/SiO_2 samples. Please note the shifted scale at each temperature.

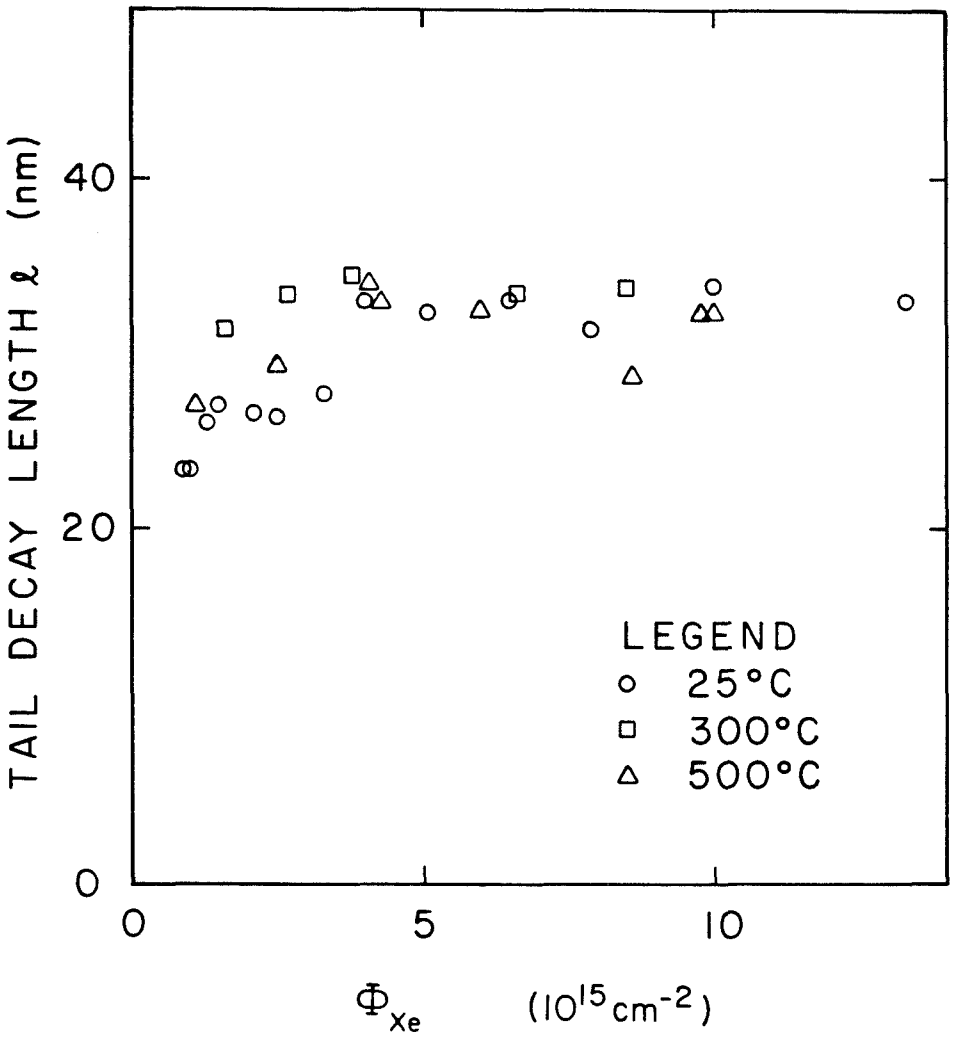

Figure 14. Dose dependence of tail decay length for 25nm Ni/SiO_2 samples.

required for this to occur, $\Phi > 10^{17}$ cm^{-2}, based on the results of Barcz, et al. [15,16] for the Xe irradiation-induced spreading of thin Ni markers in SiO_2.

The Ni tails closely resemble theoretical primary recoil profiles. Cascade mixing does not seem likely to alter the profile within the 20nm resolution limit of RBS. The appearance of NiO clusters at ~40nm suggests that some redistribution must occur for $\Phi = 6\text{x}10^{15}$ cm^{-2}. The recoil profile can be described for $x >$ 30nm by

$$C_R(x) = \frac{\Phi R}{l} e^{-\frac{x}{l}} \qquad (4)$$

where R is the extrapolated recoil yield. The radius of a spherical volume containing 300 Ni atoms varies from 4 to 12nm over a 100nm tail with this distribution for $\Phi = 6\text{x}10^{15}$ cm^{-2}. The redistribution of Ni necessary to form the observed precipitates would not be perceptible by RBS.

3. Net Ni Transport

The net areal density of Ni incorporated in the SiO_2, $[Ni]_s$, can be accurately determined by summing the counts over the entire Ni spectrum. This integral is conserved in the gaussian convolution. Fig. 15 shows that the relationship between $[Ni]_s \Phi^{-\frac{1}{2}}$ and $\Phi^{\frac{1}{2}}$ exhibits a greater variety of structure when a larger fluence range is considered. Two regimes exist for mixing at 300C and below. $[Ni]_s$ has a linear Φ dependence at low fluences (recall Eqn. 2). The slope decreases at higher fluences by the introduction of a $\Phi^{\frac{1}{2}}$ dependence. The intersection of the low and high Φ asymptotes define a transition fluence Φ_0 = 0.22, 1.6x10^{15} cm^{-2} for 25, 300C respectively. Recoil implantation accounts for some of the linear Φ contribution remaining for $\Phi > \Phi_0$. The mixing at 500C follows a linear Φ dependence over the entire fluence range, which is commensurate with the linear component remaining at lower temperatures for $\Phi > \Phi_0$.

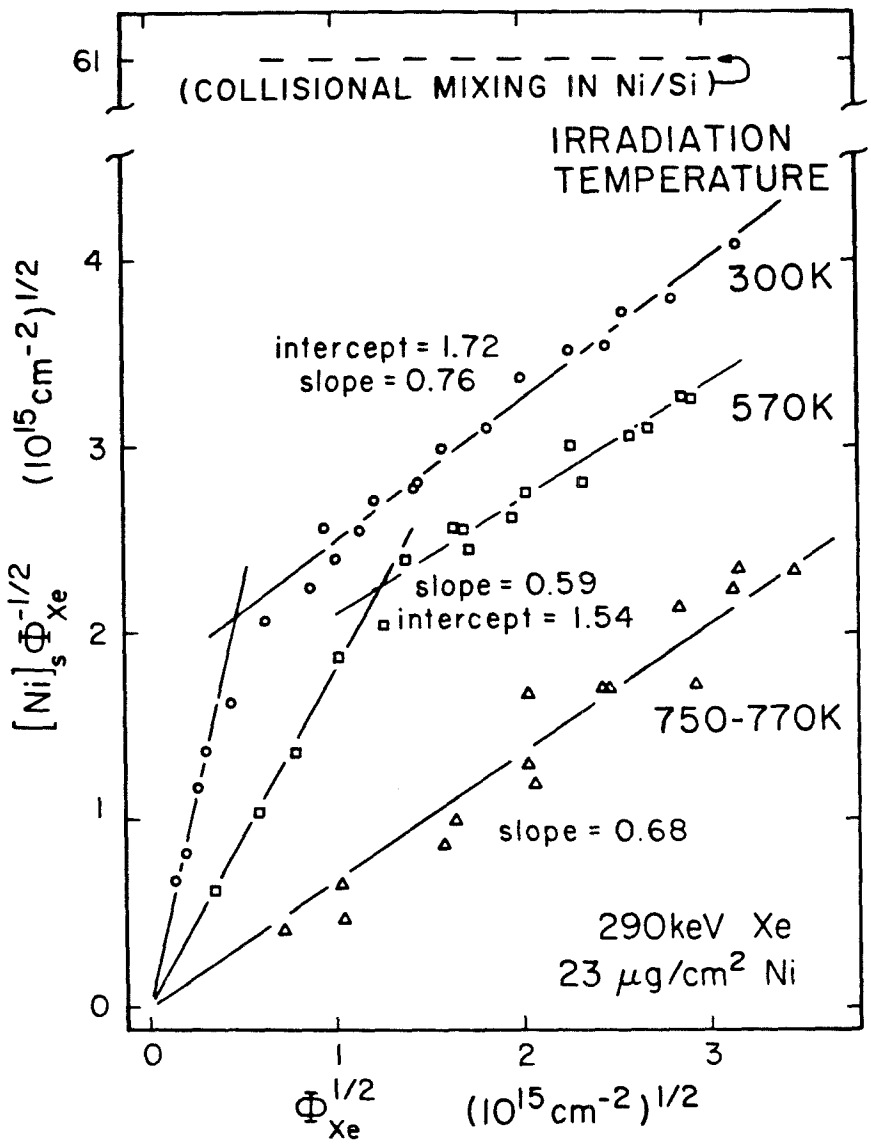

Figure 15. Relationship between mixing and fluence for various irradiation temperatures.

The initial slope at $\Phi < \Phi_0$ is most sensitive to the irradiation temperature. The linear component (slope) at higher fluences is only slightly affected by implantation temperature, consonant with deep recoil implantation. The mixing in Ni/Si is also indicated at the top of the figure. An initial linear dependence is not observed for $\Phi > 10^{13}$ cm^{-2}.

The dose dependence elicits a simple interpretation. It is important to distinguish between atomic motion within a single cascade and the statistical effects associated with the cumulative behavior of overlapping cascades. Both isotropic and anisotropic motion occurs within a cascade which can transport Ni from the metal film into the SiO_2, while previously incorporated atoms engulfed in the cascade are relocated within the SiO_2 or returned to the film. The dominant Ni flux (per incident ion) at low Φ results from the injection of Ni into the SiO_2 by each cascade. This flux is initially constant as the distribution of injected atoms is the same for each cascade. There is a diffusional flux associated with the random walk generated by subsequent overlapping cascades which increases as $[Ni]$ grows. The transition Φ_0 occurs when the diffusional and injection fluxes are commensurate. The concentration gradient at the interface at 500C is not sufficient to sustain this competition and only a low level injection is apparent. The behavior for $\Phi < \Phi_0$ reflects the basic process whereby Ni is incorporated into the SiO_2. The intercept for $\Phi > \Phi_0$ corresponds to Ni diffusion within the SiO_2 as the result of further ion mixing after a steady-state profile is established adjacent to the interface. The Ni film must act as both a source and a sink.

Φ_0 can be used to define an effective cross-section α for Ni displacement by the relation $\alpha \cdot \Phi = 1$. Irradiation damage studies with $CrSi_2$ show that $\Phi \sim 10^{12}$ cm^{-2} when $\alpha \sim (10\text{nm})^2$ is determined by the physical extent of the cascade. You can read about this in Appendix AIII.3. This fundamental transition

also occurs at $\Phi < 10^{13}\,cm^{-2}$ with Ni/Si. The effective area for Ni/SiO_2 is extremely small, $(0.7nm)^2$ and $(0.2nm)^2$ at 25C and 300C, respectively, compared with the size of the cascade.

4. First Moment

Some additional information regarding the evolution of the structure within the peak was provided by the integral $(Q\bar{x})_p = \int^{53nm} x\,[Ni]\,dx$. The SiO_2 surface was chosen as $x = x_0 = 0$. The RBS surface energy for Ni was determined using the O, Si and Xe edges as an internal standard. XPS showed that the Xe was within ~1nm of the surface. The calibration was frequently verified using O, Si, Ni and Pt thick film surface edges. The depth dependence of the product $x \cdot [Ni]$ is shown in Fig. 16 for $\Phi \simeq 4x10^{15}\,cm^{-2}$. The region $x < 53nm$ was used to define $(Q\bar{x})_p$ since it contains the contribution from the peak with only a slight interference from the tail. The tail was previously characterized and its inclusion obscures the peak. The principle error in calculating $x \cdot [Ni]$ comes from the uncertainty $\Delta x_0 = \pm 0.7nm$ in establishing the Ni surface position. The convolution of a profile $f(x)$ with spectrometer noise alters the product $x \cdot f(x)$ without changing its total integral. The perturbation to the partial integral $(Q\bar{x})_p$ produced by this convolution can be safely ignored here. The sample variance of the ratio $\frac{(Q\bar{x})_p}{\Phi}$, plotted in Fig. 17, is shown by the error bars and probably arises from the uncertainty Δx_0. The He energy loss in the Xe and Ni was neglected in calculating $x \cdot [Ni]$. This produces a ~0.7nm shift in the calculated $(Q\bar{x})_p / \Phi$, and also introduces a $\sim 0.1nm/10^{15}\,cm^{-2}$ variation with Φ. $(Q\bar{x})_p / \Phi$ exhibits a different behavior at low and high temperatures. The correlation between $(Q\bar{x})_p / \Phi$ and Φ at 25, 300C is probably not related to ion mixing. There is a clear Φ dependence at 500C, however. Different mechanisms are dominant

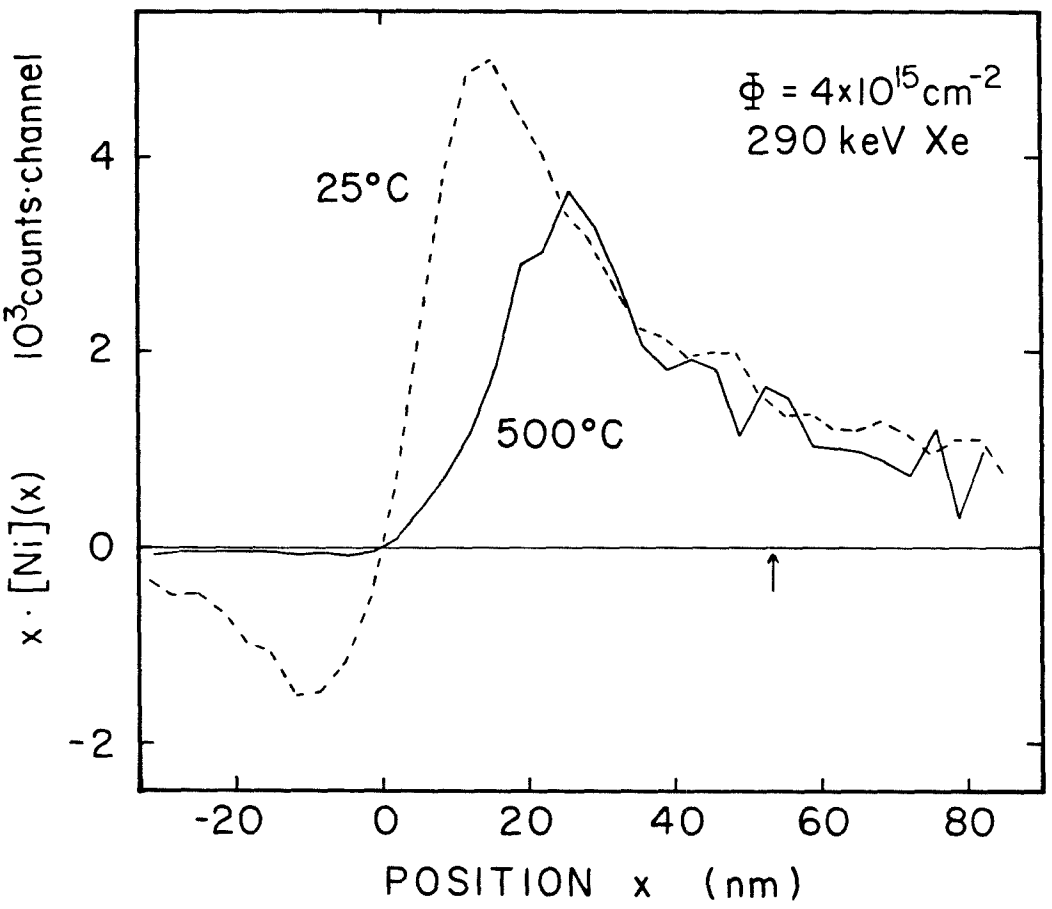

Figure 16. Typical dependence of x·[Ni](x) versus position x for 25nm Ni/SiO_2 samples irradiated at 25°C (dashed line) or 500°C (solid line) with 290 keV Xe.

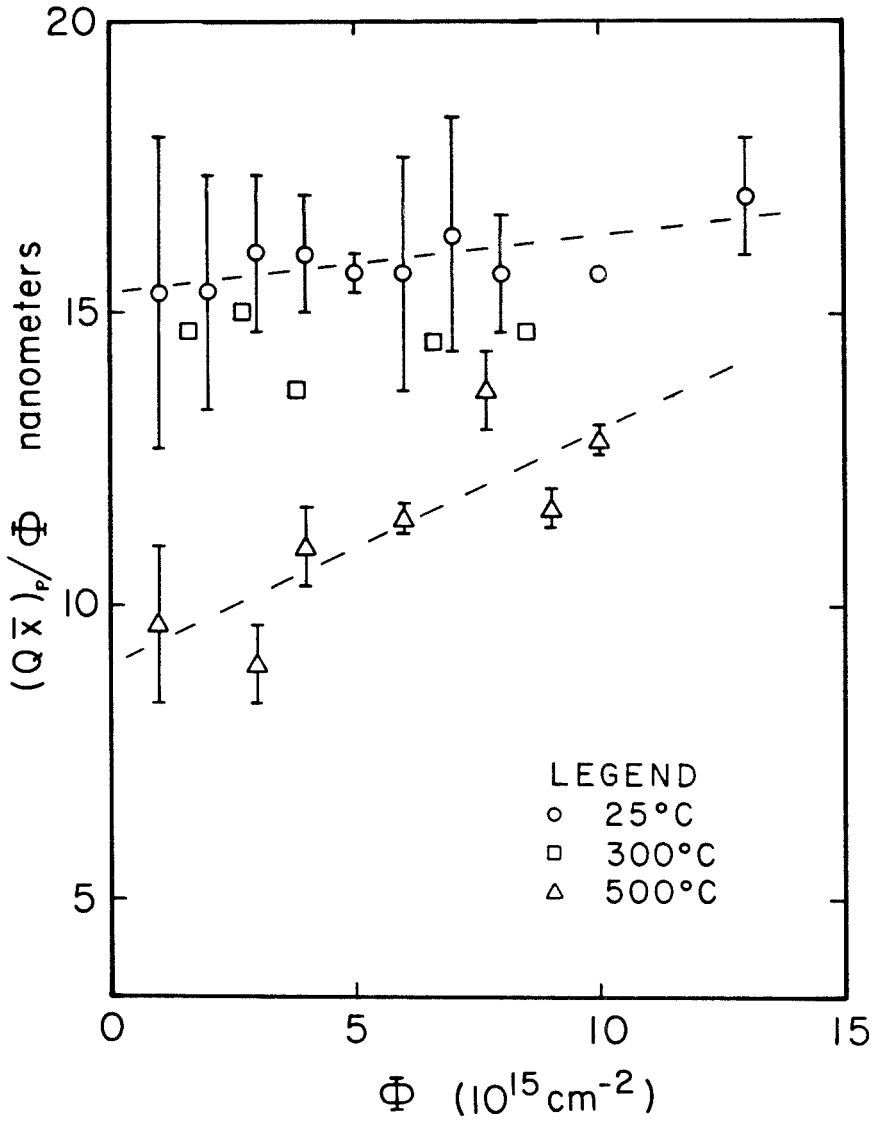

Figure 17. Dose dependence of the partial first moment for 25nm Ni/SiO_2 samples irradiated at various temperatures with 290 keV Xe.

at high and low temperatures.

The moment $(Q\bar{x})_t = \int^{100nm} x\,[Ni]\,dx$ is dominated by the deep recoil tail. An analysis of variance using Scheffé's test [17] failed to show significant correlation between $(Q\bar{x})_t / \Phi$ and either dose or irradiation temperature. The observed value $(Q\bar{x})_t / \Phi$ = 20±3nm concurs with the value one would deduce using Eqn. 4 to describe the describe the primary recoil profile.

E. Parametric Studies with Ni/SiO_2

The following experiments examine the influence of Xe energy, SiO_2 thickness, temperature and local oxygen stoichiometry on the rate of mixing in $Ni/SiO_2/Si$.

1. Energy Dependence with Fixed Sample Thickness

This experiment complements the earlier one with varied sample thickness. The amount of mixing $[Ni]_s$ was measured for 28nm Ni/SiO_2 samples irradiated with 100 - 400 keV Xe at 25C. The dose dependence for the different energies is shown in Fig. 18. The familiar linear relationship (Eqn. 2) is apparent at each energy. The mixing efficiency Q_M (Eqn. 3) calculated for these lines are included in Fig. 11 (open circles). As previously noted, there is a significant correlation with F_D. It is unlikely that several distinct mechanisms together would produce such consistent behavior over this range of metal activity and implantation conditions.

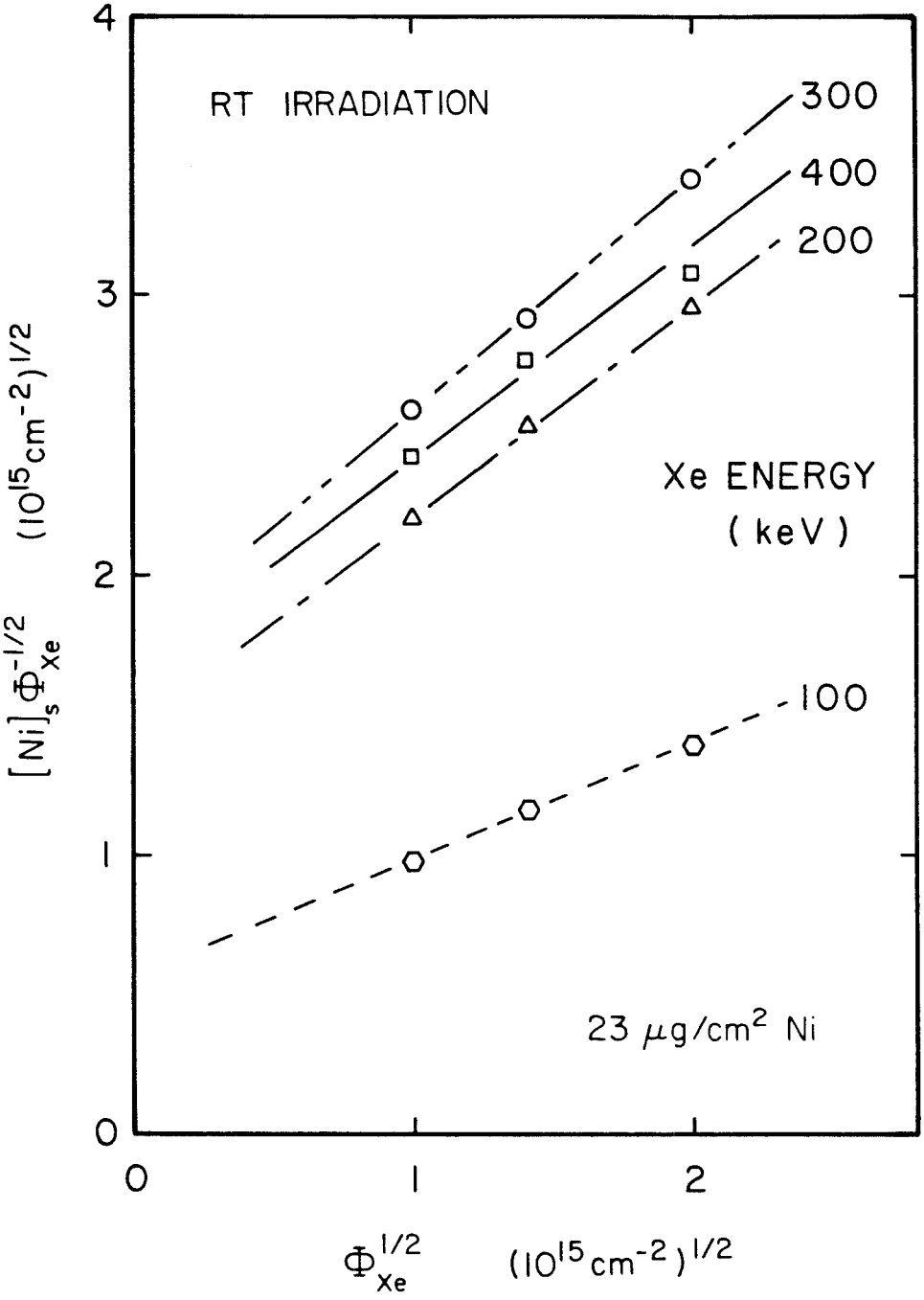

Figure 18. Relationship between mixing and fluence for 25°C irradiation with Xe at various energies.

2. Thin SiO_2 Layers

Several different thicknesses of SiO_2 on Si were used in this investigation. 20nm thick Ni films were employed. A small adjustment of the Xe energy to 240keV was made to compensate for the thinner Ni film. The role of oxygen is apparent in Fig. 19 where the relationship between $[Ni]_s \Phi^{-\frac{1}{2}}$ and $\Phi^{\frac{1}{2}}$ is presented for these samples. The irradiations were all performed at 25C. The behavior for the thick SiO_2 layer ($\sim 2\mu m$) is similar to that previously described in Fig. 15, while the differences are consistant with the change in energy and Ni thickness according to the trend with F_D in Fig. 11 (open square). A clean Ni-Si interface was obtained by etching an oxidized wafer in 10% HF immediately prior to the Ni deposition. There was some reaction between the Ni and Si associated with their contact. The areal density of Ni remaining after etching an as- deposited sample was $[Ni]_s(0) = 10 \pm 0.2 \times 10^{15} cm^{-2}$. Cheung, et al.[18] previously observed this effect using a more sophisticated channeling technique. The initial silicide $[Ni]_s(0)$ and $[Ni]_s(\Phi)$ due to ion mixing were assumed to add in quadrature. The stoichiometry of the intermixed region was that of Ni_2Si. Diffusional mixing dominates at even low Φ. Several features were noted earlier concerning the relatively large amount of mixing and the absence of the initial linear dependence seen with SiO_2.

The Si-SiO_2 interface is also a sink for the Ni in SiO_2 since the solubility and diffusivity of Ni in Si are far greater than in SiO_2 [19,20]. Only a linear Φ dependence is observed over the investigated range for 5nm SiO_2. The slope is identical to the initial slope for $\Phi < \Phi_0$ with thick SiO_2. The measured variation in the areal density $[^{16}O]_s$ between implanted and unimplanted samples was <5%. It is not likely that native oxide formation is responsible for this invariance. The amount of Ni contained in the Si was measured after removing the 5nm SiO_2 layer with 1:10 HF:ethanol. This showed that a steady state accumulation of

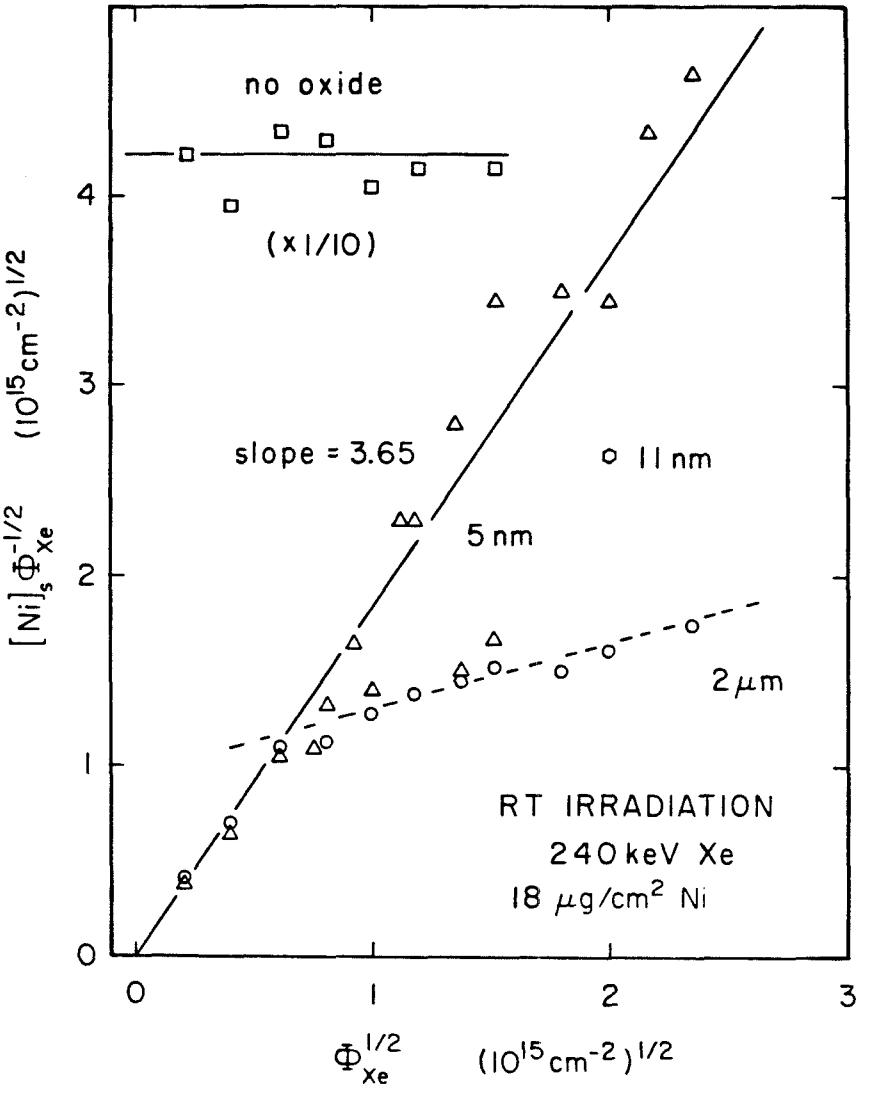

Figure 19. Relationship between mixing and fluence at 25°C for different thicknesses of SiO_2 .

~0.8×10^{15} Ni cm^{-2} in this SiO_2 layer was established at $\Phi \simeq 0.06 \times 10^{15}$ cm^{-2}. The mixing for a 11nm SiO_2 sample lies between the curves for the other two configurations as shown. There was rapid silicide formation at Xe fluences exceeding ~10^{15} cm^{-2} when a 1.2nm SiO_2 layer was used.

This experiment establishes two important facts. The processes retarding Ni transport or establishing the boundary condition at the Ni-SiO_2 interface are confined within 5nm of the interface. This region coincides with the denuded zone. The diffusion of Ni in SiO_2 back to the Ni-SiO_2 interface results from the accumulation of Ni at a depth exceeding 5nm, for otherwise there would have been a ~50% reduction in slope at high Φ in Fig. 19 even with the 5nm SiO_2 samples.

This investigation could not be extended to usefully higher temperatures. Ni/Si reacts spontaneously above ~150C. The permeability of the 5nm SiO_2 is sufficiently altered by 10^{15} cm^{-2} irradiation that substantial silicide formation occurs by thermal processes at 300C. This phenomenon has been reported in other systems [21,22]. Possible waiting time behavior associated with a concentration dependent diffusivity would be interesting to investigate. There is a question whether the ion irradiation changes the characteristics of the oxide or if the incorporated metal introduces high mobility paths through the oxide.

3. Sequential Irradiation

The following experiment was devised to assess how the irradiation temperature affects the evolution of the shallow peak. A set of 25nm Ni/SiO_2 samples were irradiated at 25C with 290keV Xe to a dose $\Phi/2$ for Φ = 2, 4.5, 6×10^{15} cm^{-2}. The carousel temperature was then raised to 300C, and the same irradiation performed for a net fluence Φ. This order was reversed for a second set of samples. Both sets were irradiated simultaneously at 300C. Two control

samples received doses at $6x10^{15}$ cm^{-2}: one at 300C, and the other receiving a fluence of $3x10^{15}$ cm^{-2} with each 25C implantation. The amount of mixing in these samples is shown in Fig. 20. The labels refer to the order of the low (L) and high (H) temperature irradiation. Results from Fig. 15 are included for a comparison of the scatter. The LL and HH results agree with those of Fig. 15. The difference between LH and HL results is comparable to the scatter in the single temperature data. Either sequence produces essentially the same result; the profiles for a given net Φ were indistinguishable by RBS.

The earlier experiments suggested that a steady-state Ni concentration C_{ss} was established near the interface by the balance of injection and diffusional fluxes, which decreases with increasing temperature. It seems reasonable then that C_{ss} established at one temperature would be unstable at another. It is therefore surprising that there is no apparent out-diffusion of Ni for the LH sequence relative to HL.

This anomaly was also investigated with permutations of 25C and 500C irradiation temperatures. A sample was irradiated with $6x10^{15}$ cm^{-2} Xe at 25C followed by a $3.3x10^{15}$ cm^{-2} Xe irradiation at 500C. The Ni profiles after the 25C and the sequential implantation are shown in Fig. 21. The profiles for $10x10^{15}$ cm^{-2} Xe irradiation at a single temperature are also indicated for comparison. The Ni peak is not diminished by the subsequent 500C irradiation. The peak remains unchanged in the second implantation with only the addition of Ni to the tail. The mixed temperature profile resembles the superposition of the profiles obtained for each temperature individually. Fig. 22 shows a cross-sectional TEM micrograph of the mixed temperature sample. The Ni bearing clusters are substantialy larger than 21nm. Their distribution is a curiosity.

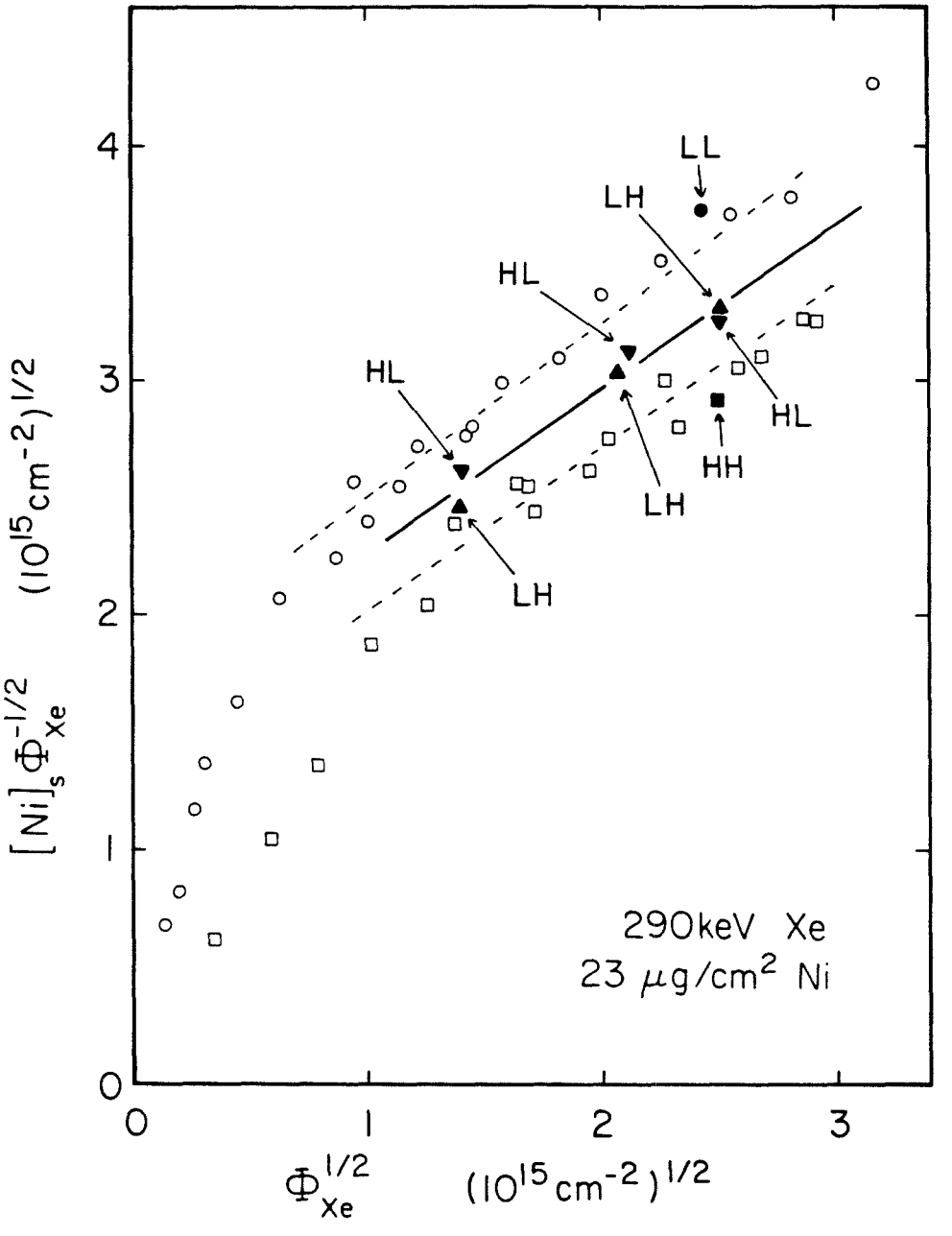

Figure 20. Results from mixed temperature experiment with 25°C and 300°C. HL describes the sequence 300°C first followed by 25°C, etc.

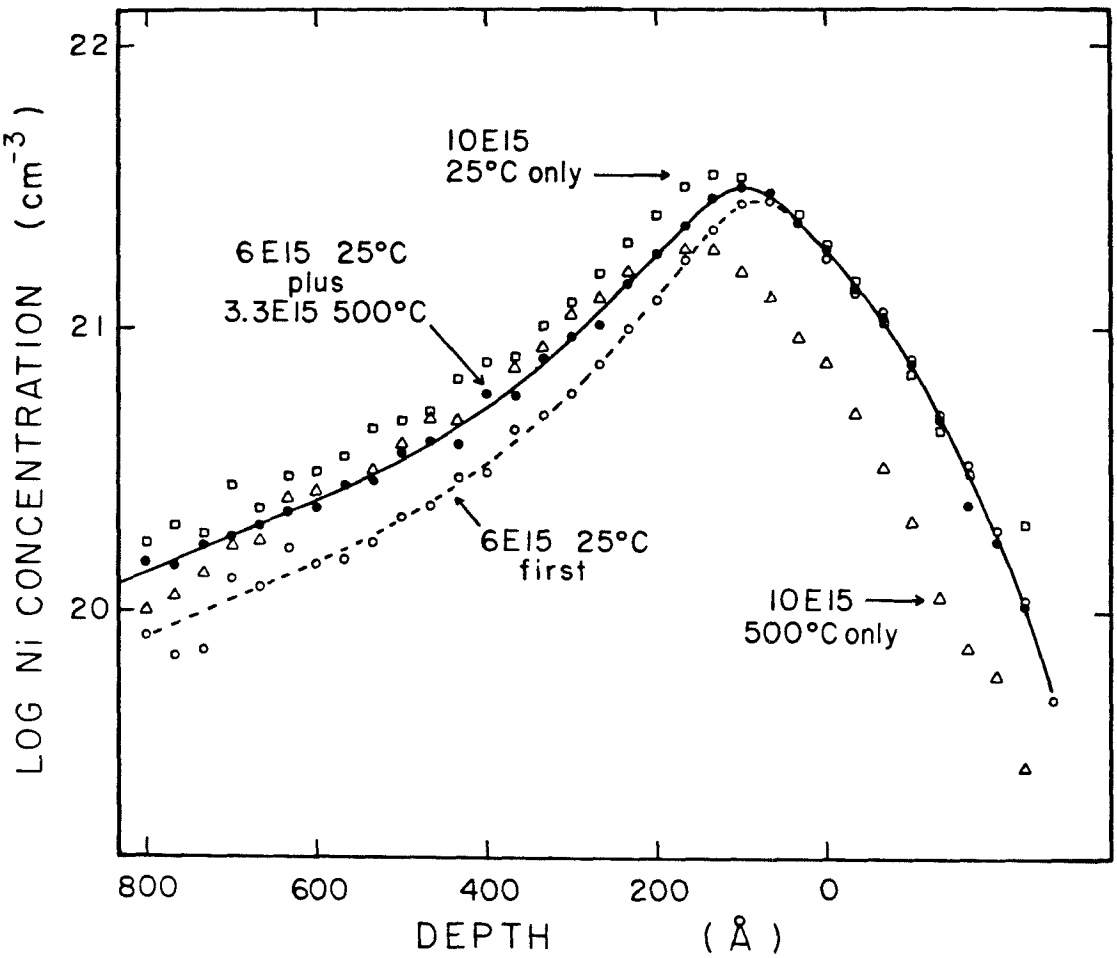

Figure 21. Ni RBS depth profiles for mixed temperature experiment with 25°C and 500°C.

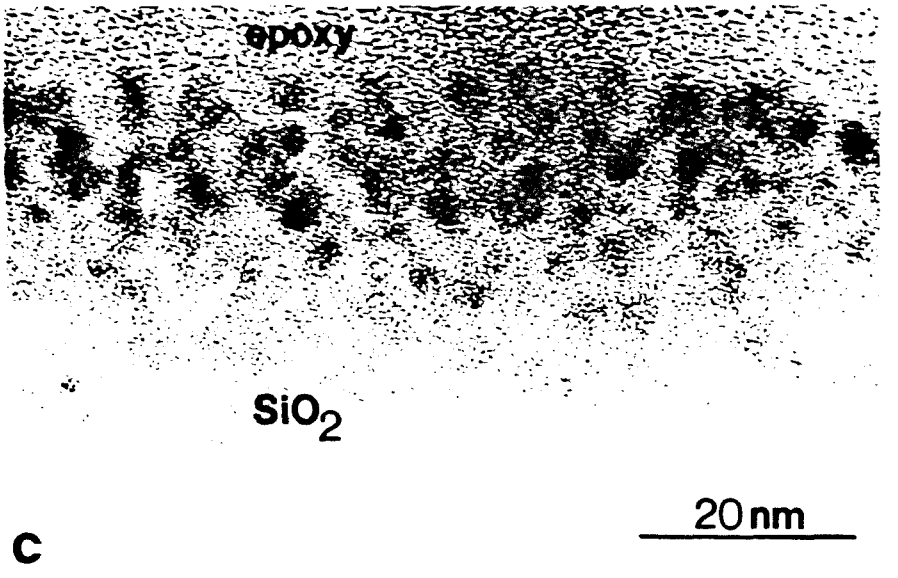

Figure 22. Cross-sectional TEM image of a Ni sample irradiated first at 25°C followed by 500°C (see text). The free Ni was previously removed.

4. Oxygen Pre-Implantation

Oxygen is required to form NiO. The equilibrium concentration of available mobile O in SiO_2 produced by wet oxidation is $3x10^{19}$ cm^{-3} [23]. The amount of this O within a 2μm layer is ~$6x10^{15}$ cm^{-2}, less than that contained in NiO for samples with $\Phi > 4x10^{15}$ cm^{-2}. If the rate limiting step in the formation of NiO requires the liberation of O from the SiO_2, then a pre-implantation of O may enhance subsequent mixing with Xe. 25nm Ni/SiO_2 samples were implanted with 150keV O_2^+ to a fluence of $1x10^{15}$ O cm^{-2}. This should alter the O stoichiometry within 100nm of the interface by $\Delta[O] \simeq 4x10^{15}$ cm^{-3}, which is commensurate with $[Ni]$ in the peak. These samples were subsequently implanted with $1x10^{15}$ cm^{-2} Xe. The O pre-implantation produced no discernible change in the resultant Ni profile. Apparently, the incorporation of Ni is not restricted by just the dissociation of SiO_2 and the availability of free O. The chemical state of the O should be examined with XPS. It is possible that an equilibrium is established between the SiO_2 and implanted O in accordance with Le Chateliar's principle. The complimentary experiment with a Si pre-implantation was not attempted.

There is a possibly interesting analogy to the previous result. The electrical activity of Si in GaAs is determined by the substitutionality of the Si on the Ga and As lattice sites. It was once thought that an implantation with As or Ga would alter the concentration of vacancies and consequently modify Si substitutionality. This did not happen, either. It was argued in this case that the defects produced by the altered stoichiometry were absorbed by the substrate during annealing required to promote Si activation and regrowth of the damaged layer. The reader will find this paper is included as Appendix AIII.4.

5. Thermal Stability of Ni Profile

The kinetic energy of the atoms within a well-developed, dense cascade are on the order of 1eV. Several models of ion mixing relate the motion within a cascade to the relatively high local temperature [13,24,25]. We therefore examined the stability of the Ni profile produced by $6x10^{15}$ cm^{-2} Xe irradiation at 25C with respect to thermal annealing at 800C for 1 hour. The Ni film coalesced into islands as expected, and was physically removed by wiping the samples surface with a cotton swab; no etching was employed. The RBS spectra for this sample is shown in Fig. 23. The solid and dashed lines are reproduced from Fig. 12 for the 25C and 500C profiles, respectively. The shallow peak is completely expelled by the annealing. The diffusion coefficent for Ni in amorphous SiO_2 has an Arrhenius behavior given approximately by $10^{-9} e^{-1.6eV/kT}$ cm^2/sec [20]. The Ni diffusion length for our annealing conditions is only 2.4 nm. The clusters enhance the expulsion of Ni from the SiO_2. Xe accumulates at the interface for implantations at both 25C and 500C. Much of this Xe is also expelled during the thermal annealing.

F. Xe Redistribution

Much of the Xe, which ballistically should have stopped in the Ni film, was found within the SiO_2. The Xe profiles for a set of samples, consisting of 40nm Ni on SiO_2 implanted with various fluences of 290keV Xe at 25C, are shown in Fig. 24. This thickness corresponds to the projected range of the Xe in Ni. The profiles have been scaled to give a constant peak height. Please note that the Ni layer has not been removed. The Xe profile with $\Phi = 1x10^{15}$ cm^{-2} closely follows a theoretical estimate of the Xe concentration, calculated using the approximation discussed in Chapter V. The reason for the discontinuity in the Xe profile is that the Xe travels farther in the SiO_2 than in Ni for a given energy loss, and the

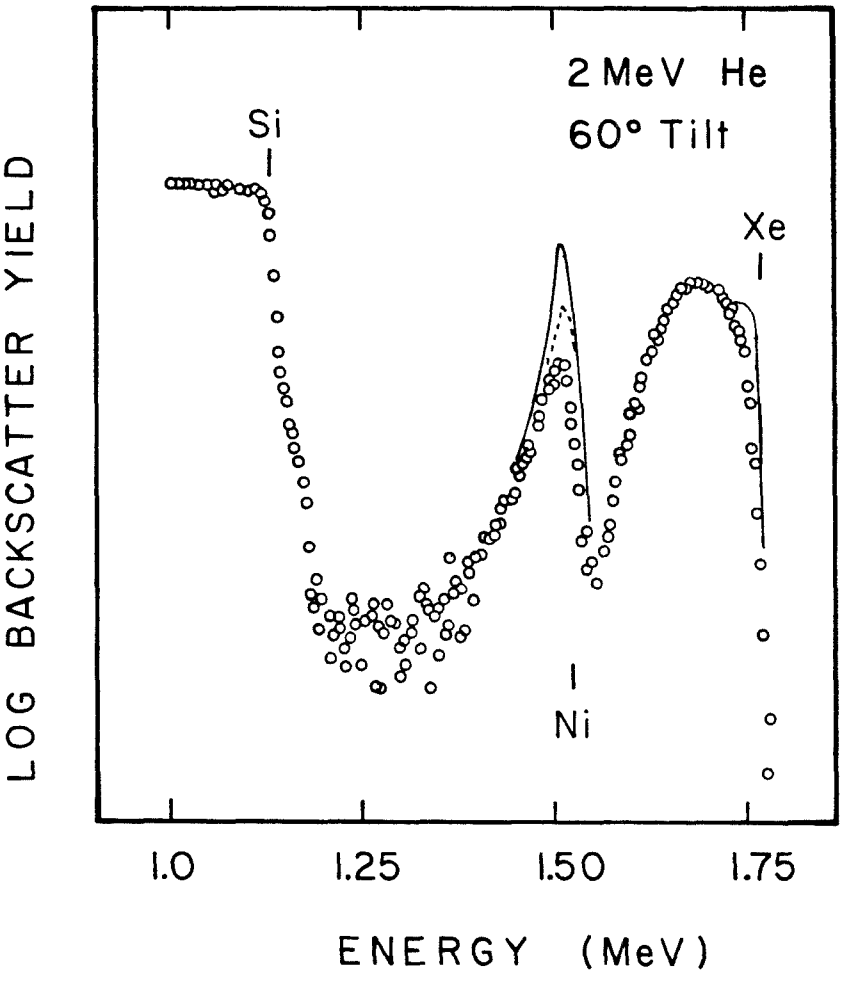

Figure 23. RBS spectra for an implanted Ni sample ($6x10^{15}$ Xe cm^{-2}) after annealing at 800°C for 1 hour (circles). The solid line is the Ni spectra for a not-annealed sample after etching. The dashed line is for the corresponding 500°C irradiation .

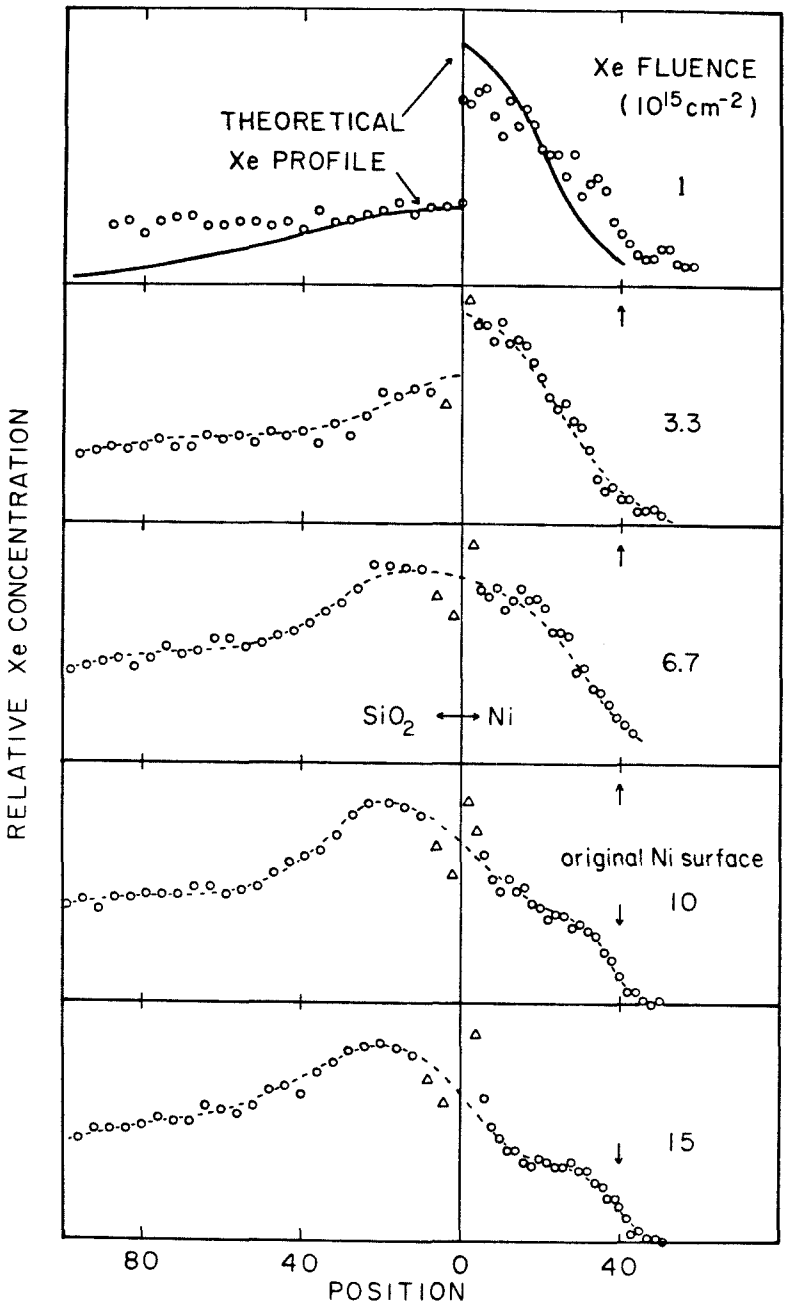

Figure 24. Xe RBS depth profile in Ni and SiO_2 after irradiation at 25°C with 290keV Xe at various fluences. The Ni layer was 33nm thick.

profile is therefore more spread out. The calculation does not account for the influence of the SiO_2 on the flux of reflected Ni atoms (continuous stopping approximation), and therefore slightly over-estimates the Xe concentration in the Ni near the interface. The significant feature is that the Xe is expelled from the Ni and incorporated in the SiO_2 at higher fluences. The Xe concentration in the Ni saturates at about $5x10^{20} cm^{-3}$. The same effect was apparent at other energies and film thickness, and with Ti and Cr as well. The Xe profile remains relatively uniform in the region containing the metal. An interaction between the Xe and Ni seems unlikely, but certainly cannot be ruled out. The correlation between Q_M and $[Xe]_s$ is not significant compared with the correlation to F_D reported in Fig. 11. The Xe redistribution observed in the variable energy experiment (Section E.1) could be modeled by assuming that most of the Xe within ~10nm of the interface in the Ni was pushed into the SiO_2. A thermal mechanism is probably responsible for the Xe redistribution, since the transport greatly exceeds that expected on the basis of ballistic mixing alone. This topic was not investigated further. The phenomena of Xe redistribution has been reported by others [26].

References

[1] B. M. Paine and R. S. Averback, *Nucl. Instr. and Meth.* **B7/8**, 666 (1985)

[2] T. Sands, private communication (1985)

[3] R. P. Elliot, *Constitution of Binary Alloys, First Supplement* (McGraw-Hill, New York, 1965), 661

[4] , *Powder Diffraction Files*

[5] K. S. Kim and R. E. Davis, *J. Elect. Spectrosc. and Related Phenom.* **1**, 251 (1972/1973)

[6] N. S. McIntyre, T. E. Rummery, M. G. Cook and D. Owen, *J. Electrochem. Soc.* **123**, 1164 (1976)

[7] M. G. Mason, S.-T. Lee and G. Apai, *Chemical Physics Lett.* **76**, 51 (1980)

[8] M. G. Mason, *Phys. Rev. B.* **27**, 748 (1983)

[9] R. Kelly in *Chemistry and Physics of Solid Surfaces V*, R. Vaselow and R. Howe, eds. (Springer-Verlag, New York, 1984), 159

[10] P. J. Grunthaner, Ph. D. Thesis, California Institute of Technology, (1980)

[11] K. B. Winterbon, *Ion Implantation Range and Energy Deposition Distributions* (IFI Plenum, New York, 1975)

[12] D. K. Brice, *J. Appl. Phys.* **46**, 3385 (1975)

[13] W. L. Johnson, Y.-T. Cheng, M. Van Rossum and M-A. Nicolet, *Nucl. Instr. and Meth.* **B7/8**, 657 (1985)

[14] R. Pretorius, J. M. Harris and M-A. Nicolet, *Sol. St. Elect.* **21**, 667 (1978)

[15] A. J. Barcz, B. M. Paine and M-A. Nicolet, *Appl. Phys. Lett.* **44**, 126 (1984)

[16] A. J. Barcz and M-A. Nicolet, *Appl. Phys.* **A 33**, 167 (1984)

[17] H. A. Scheffé, *Biometrika* **40**, 87 (1953)

[18] N. W. Cheung, R. J. Culbertson, L. C. Feldman, P. J. Silverman, K. W. West and J. W. Mayer, *Phys. Rev. Lett.* **45**, 120 (1980)

[19] M-A. Nicolet and S. S. Lau in *VLSI Electronics: Microstructure Science, Vol. 6*, N. G. Einspruch and G. B. Larrabee, eds. (Academic Press, New York, 1983), 391

[20] R. N. Ghoshtagore, *J. Appl. Phys.* **40**, 4374 (1969)

[21] L. S. Wielunski, C-D. Lien, B-X. Liu and M-A. Nicolet in *Metastable Materials Formation by Ion Implantation*, S. T. Picraux and W. J. Choyke, eds. (North-Holland, New York, 1982), 139

[22] T. C. Banwell, M. Finetti, B-X. Liu, M-A. Nicolet, S. S. Lau and D. M. Scott in *Defects in Semiconductors II*, J. W. Corbett and S. Mahajan, eds. (North-Holland, New York, 1983), 411

[23] A. S. Grove, *Physics and Technology of Semiconductor Devices* (Wiley, New York, 1967), 28

[24] U. Shreter, F. C. T. So, B. M. Paine and M-A. Nicolet in *Ion Implantation and Ion Beam Processing of Materials*, G. K. Hubler, O. W. Holland, C. R. Clayton and C. W. White, eds. (North-Holland, New York, 1984), 31

[25] L. M. Gratton, A. Miotello and C. Tosello, *Appl. Phys.* **A 36**, 139 (1985)

[26] D. C. Ingram and D. G. Armour, *Nucl. Instr. and Meth.* **194**, 117 (1982)

Chapter IV Models for Characterizing Bilayer Mixing

A. Introduction

A number of mechanisms are known to contribute to atomic transport in ion mixing [1-4]. Recoil implantation is the simplest to recognize. The motion of a primary recoil can be treated separately from the response of the rest of the target. A very large number of target atoms experience short range displacements induced by the cascade of higher generation collisions, which are governed by screened coulomb interactions [2]. The motion within a cascade is predominantly isotropic, although the anisotropic flux of secondary recoils may also be significant. Electronic interactions introduce chemical effects after the average particle energy has diminished to $O(1\text{eV})$. Much of the mixing in metal-metal systems occurs in this thermalized regime [4]. Chemical effects can bias the random walk motion within this regime producing a Darken effect. The intermixing ceases when the average particle energy falls below the cohesive energy binding the atoms in the sample [3]. Johnson et al. have proposed that the metallurgical phases are formed after the concentration profile is established [3]. The formation of an intermediary liquid-like state in a dense cascade is partially responsible for this separation of phenomena. The rapid quenching imposes kinetic constraints, which may favor formation of metastable phases [3,5]. The formation and migration of point defects such as vacancies greatly enhance the diffusional mixing at elevated temperatures in both metal-metal and metal-silicide systems [6-8]. The lifetime of the defects produced in a cascade is long enough so that the defects produced in subsequent overlapping

cascades may interact. Mixing will then depend on the flux $\dot{\Phi}$, in addition to the fluence Φ [8]. A dose rate effect is not observed with the other mechanisms.

It may be possible to examine the problems of describing net metal transport and phase formation separately in the M-SiO_2 system for irradiation a low temperatures. It was previously shown that the evolution of the metal RBS profiles are very similar for Ti, Cr and Ni, with deviations correlated to ballistic effects, even though the morphology of the mixed regions are very different. The chemical reactions of M with SiO_2 are more complicated than those of binary alloys. The saddle point configuration necessary to produce a reaction in our ternary system is certainly much harder to achieve than that for a binary alloy. The net transport at low temperatures may not be affected by chemical reactivity if the reaction rates are slow compared with the lifetime $\tau \sim 10$pSec of the cascade. The number of successful attempts estimated using the Eyring rate equation $\tau \cdot \frac{kT}{h} e^{-\Delta G / kT}$ is about one for T = 1700C and Δ G = 1eV [9]. The thermal reactivity of Ti with SiO_2 proceeds with the rapid removal of O from the reaction zone which is not supported by cascade mixing.

A large number of Ni clusters are contained in a single cascade volume. No serious restriction is imposed therefore by the local confinement of the metal in clusters. Ni may not be confined to the clusters during a cascade. The redistribution of Xe in the SiO_2 and Ni suggests that the cascades are dense enough to produce effective temperatures sufficient for rapid Xe diffusion. The thermal annealing demonstrated that Ni and Xe become mobile in the oxide at commensurate temperatures. We shall examine the consequences of assuming that phase formation and net transport can be treated separately. The mixed temperature experiments show that this hypothesis requires additional qualifications. Chemical reactions are apparent at high temperatures (Appendix AIII.2). An irradiation temperature of 500C is close enough to the threshold for

thermal reaction that ion mixing is capable of promoting the reactions and processes which would occur spontaneously at higher temperatures. The 25C - 500C mixed temperature experiment shows that cluster formation with Ni restrains transport at high temperatures.

B. Formal Description of Transport

We shall assume that the details of phase formation can be ignored if we restrict our interest to the average metal profile. There is a rapid fluctuation in the Ni density associated with the clusters. The distribution of Ni clusters depends on the depth x, but there does not appear to be a significant correlation with the position transverse to the surface normal. A meaningful description of the metal distribution is provided by the average number of atoms per unit area contained in a region of width dx parallel to the surface at a depth x; $C(x,\Phi)\,dx$. This was implicitly assumed in pursuing the RBS study.

The metal concentration at a particular point in the sample is determined by the motion occurring within each cascade containing this point. The displacements produced in a cascade differ for each cascade. It will be assumed that the transport within the SiO_2 can be described by a transition probability $g(\xi \rightarrow x)\,dx$ for a metal atom at a depth ξ to be displaced to x, dx in a single cascade. This is justified if the same mechanism governs the independent cascades. A dose rate effect is not expected [8]. If $C_n(x)$ is the average depth distribution of metal produced by precisely n overlapping cascades, then the evolution of the metal profile within the SiO_2 can be described by the Chapman - Kolmogorov equation [10];

$$C_{n+1}(x) = \frac{a_r}{a} f_r(x) + \int_0^\infty C_n(\xi)\, g(\xi \rightarrow x)\, d\xi \qquad (1)$$

$f_r(x)$ is the normalized profile for atoms injected into the SiO_2 from the metal

film, while a_r is the effective cross-section for an incident ion to produce injection. $a_r f_r(x)$ includes both primary and secondary recoils and their evolution during the cascade's thermalization. a is the projected area of the cascade, which is assumed to be constant (cylinderical cascade). The ratio $\frac{a_r}{a}$ represents the average number of atoms injected per cascade event. The complications from allowing a to be position dependent are not warranted here. The number n of cascades containing a particular infinitesmal region is Poisson distributed with parameter $a\Phi$. The average profile after a fluence Φ is therefore

$$C(x,\Phi) = \sum_{n=0}^{\infty} C_n(x) \cdot \frac{(a\Phi)^n}{n!} e^{-a\Phi} \tag{2}$$

Eqns. 1 and 2 define a classical Markov process [10], although the boundary condition at the M-SiO_2 interface still must be specified. Another description of the evolution of $C(x,\Phi)$ is obtained by differentiating Eqn. 2;

$$\frac{1}{a}\frac{\partial}{\partial\Phi}C(x,\Phi) = \sum_{n=0}^{\infty} C_{n+1}(x) \cdot \frac{(a\Phi)^n}{n!} e^{-a\Phi} - C(x,\Phi)$$

Substituting Eqn. 1 gives the master equation

$$\frac{1}{a}\frac{\partial}{\partial\Phi}C(x,\Phi) = \frac{a_r}{a} f_r(x) + \int_0^{\infty} C(\xi,\Phi)\, g(\xi\rightarrow x)\, d\xi - C(x,\Phi) \tag{3}$$

One could have started with the master equation and deduced Eqns. 1 and 2 as a series solution; either way permits the terms in the model to be defined. The assumption that $a_r f_r(x)$ is independent of Φ neglects sputtering of the metal film and changes in the range of the Ni atoms recoiling through the intermixed region. Eqn. 1 states that differences in the chemical interactions of the metal atoms can be ignored. It is convenient to assume that g is depth-independent and unbiased; $g(\xi\rightarrow x) = g(|\xi - x|)$, and short-ranged compared with the

distance over which $C(x,\Phi)$ varies significantly. The classical approximation to Eqn. 3 is then

$$\frac{1}{a}\frac{\partial}{\partial\Phi}C(x,\Phi) = \frac{a_r}{a}f_r(x) + D\frac{\partial^2}{\partial x^2}C(x,\Phi) \quad \text{for } x>0 \tag{4}$$

$$\text{where } D = \tfrac{1}{2}\int g(\Delta\eta)(\Delta\eta)^2 d(\Delta\eta)$$

The interesting phenomena occurs in the vicinity of the interface. We can allow some of the chemistry back into the model by adopting an impedance boundary condition (i.e. quasi-first-order kinetics) to describe the M-SiO_2 interface;

$$\left.\frac{\partial C}{\partial x}\right|_{x=0^+} = -\frac{R}{D}\left[C(0^+,\Phi) - C_0\right] \tag{5}$$

The metal film acts as both a source and a sink, depending on $C(0^+,\Phi) - C_0$, while the rate of exchange depends on the empirical rate constant R. One potential difficulty is that $x = 0$ may not really coincide with the physical interface. A similar expression applies to the Si-SiO_2 interface.

There are essentially five parameters in the model; a, D, R, C_0, and $a_r f_r(x)$. The model is fairly general in that it allows for many processes. Special cases will be compared with the experimental results. The zeroth and first moments

$$Q(\Phi) = \int_0^\infty C(x,\Phi)\,dx$$

$$(Q\bar{x})(\Phi) = \int_0^\infty C(x,\Phi)\,x\,dx$$

are of primary interest since these were experimentally measured. The initial condition prior to irradiation is taken to be $C(x,0) = 0$. Classical transport theory provides a convenient language with which to discuss our results.

C. Fundamental Low Dose Behavior

There are several cases in the following sections for which the yield produced by n overlapping cascades is $\int C_n(x)\,dx \simeq n \cdot R + n^{1/2} \cdot \begin{cases} A_1 & n=1 \\ A & n>1 \end{cases}$ where A and R are constants describing the isotropic and anisotropic behavior, respectively. The observed yield given by Eqn. 2 has the asymptotic behavior $Q(\Phi) \sim (A_1 + R)\alpha\Phi$ for $\alpha\Phi<1$, and $Q(\Phi) \sim A\sqrt{\alpha\Phi} + R\alpha\Phi$ for $\alpha\Phi>1$. The transition occurs at $\alpha\Phi=\left(\frac{A}{A_1}\right)^2$. The result of fitting this model with $A_1=A$ to the 25C data is shown in Fig. 1. As noted in Section III D.3, the fitted value of α is much too small [$\sim(0.73\text{nm})^2$] to be the area of a cascade. This shows that α does not explicitly enter into the model. The "time" like variable

$$t = \alpha\Phi$$

corresponding to the average number of events will be used hereafter, since it simplifies the notation in a natural way. It is also convenient to define $\frac{\alpha_\tau}{\alpha} f_\tau(x) = f(x)$, so that Eqn. 4 becomes

$$\frac{\partial}{\partial t} C(x,t) = f(x) + D\,\frac{\partial^2}{\partial x^2} C(x,t) \qquad (6)$$

D. Thick Oxide Layer

1. Moments

In this section only the interface at $x = 0$ is important. $C(x,t) = C(x,\Phi)$ is assumed to rapidly decrease for $x \to \infty$. Let $h(x)$ be a twice-differentiable function defined on $[0,\infty)$. If Eqn. 6 is multiplied by $h(x)$ and integrated over all x, one finds by two integrations by parts that

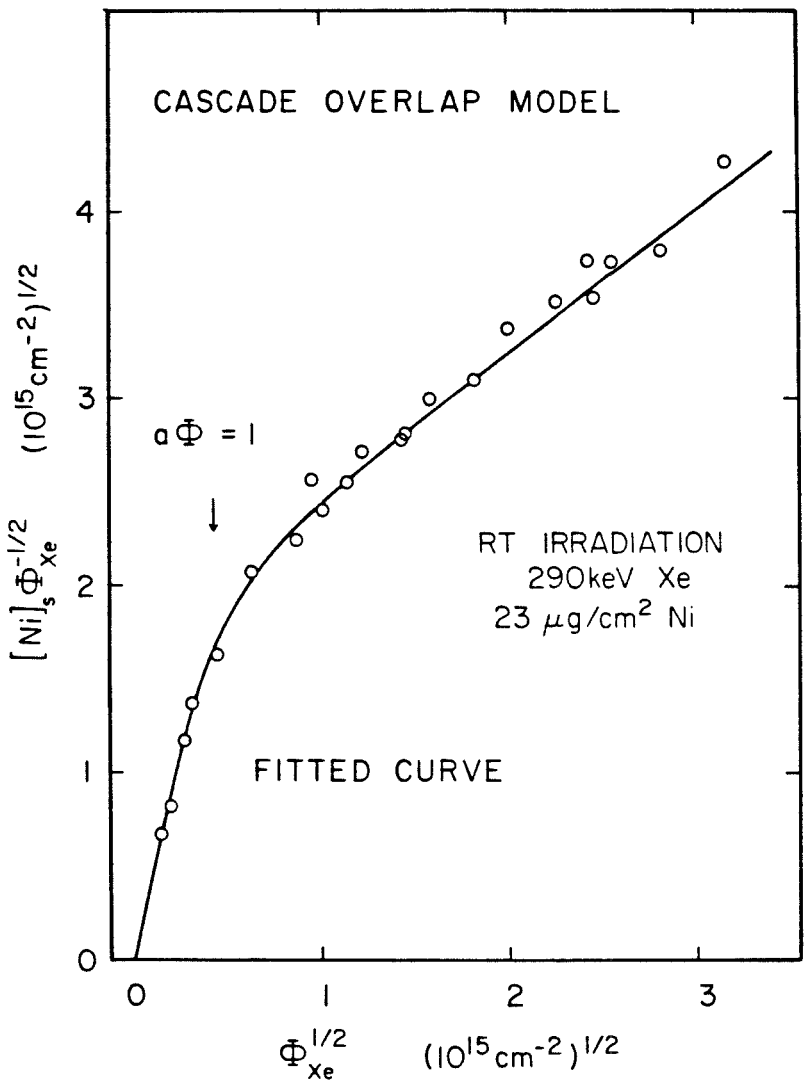

Figure 1. 25°C mixing data fitted with cascade overlap model using the parameters $A_1 = A = 0.75$, $R = 0.76$ and $a = (0.73nm)^2$.

$$\frac{d}{dt}\int_0^\infty h\,C\,dx = \int_0^\infty f\,h\,dx + D\dot{h}(0)\,C(0^+,t) + h(0)\,R\left[C_0 - C(0^+,t)\right] + D\int_0^\infty \ddot{h}\,C\,dx$$

where $\dot{h} = dh/dx$, etc. This equation provides a means of analyzing diffusion data using the moments of $C(x,t)$ [11]. Combining the results for $h=1$ and $h=x$ gives

$$\frac{Q\bar{x}}{t} = F\bar{x}_f + C_0 D + F\frac{D}{R} - \frac{Q}{t}\frac{D}{R} \qquad (7)$$

where $F = \int_0^\infty f(x)\,dx$ and $F\bar{x}_f = \int_0^\infty f(x)\,x\,dx$. Recalling that $t=a\Phi$, this model predicts a dose dependence for $\frac{Q\bar{x}}{\Phi}$ only if $\frac{D}{R}>0$ and Q has a non-linear dose dependence. Eqn. 7 fits the observed behavior for 25, 300C if the last term is negligable, but can not account for the Φ dependence at 500C.

2. Profile Evolution

The PDE defined above with Eqns. 5 and 6 can be solved using standard transform techniques [12]. We shall examine the behavior when either $f(x)$ or R dominates the mixing near the interface. The contribution of the deep primary recoils to $f(x)$ will be omitted presently and included later. These two limiting cases are illustrated in Fig. 2. The source $f(x)$ will be considered first with $R\to\infty$ and $C_0=0$. A representation of the solution obtained with separation of variables using a Laplace transform taken in t is

$$\hat{C}(x,s) = \frac{1}{\sqrt{D}}\int_0^\infty \frac{1}{s^{3/2}} e^{-x_>\frac{s^{1/2}}{\sqrt{D}}} \sinh\left[x_<\frac{s^{1/2}}{\sqrt{D}}\right] f(\eta)\,d\eta$$

where $x_> = \max(x,\eta)$ and s is the transform variable [13]. The measurable quantity of interest is the integral yield

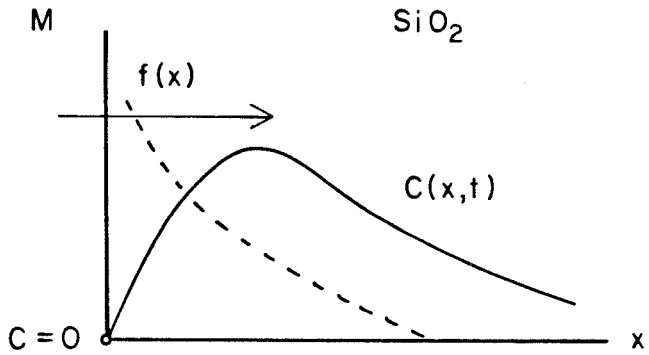

INJECTION

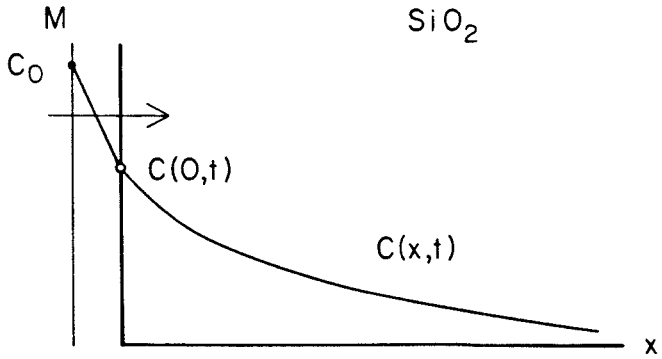

INTERFACIAL REACTION

Figure 2. Illustration of limiting cases for injection and interfacial reaction with a semi-infinite region .

$$\hat{Q}(s) = \int \hat{C}\, dx = \int_0^\infty \frac{1}{s^2}\left[1 - e^{-\eta \frac{s^{1/2}}{\sqrt{D}}}\right] f(\eta)\, d\eta \qquad (8a)$$

for which

$$Q(t) = \int_0^\infty d\eta\, f(\eta) \cdot t \int_0^1 \mathrm{erf} \frac{\eta}{\sqrt{4Dt\,\xi}} d\xi \qquad (8b)$$

The second integral can be simplified with two integrations by parts [14]. The asymptotic behavior is most easily recognized from the Laplace transform using the Tauberian theorems for $t \to 0$ ($s \to \infty$) or Watson's Lemma for $t \to \infty$ ($s \to 0$) [12,15]. One finds from the appropriate expansions in s that

$$Q(t) \sim Ft \quad \text{as } t \to 0$$

$$Q(t) \sim \frac{2}{\sqrt{\pi}} \frac{F \bar{x}_f}{D} (Dt)^{1/2} \quad \text{as } t \to \infty$$

These expressions are intuitively appealing. Injection dominates at low doses, since C is too small for diffusion to be significant. Near the interface, C increases until a steady-state value C_{ss} is attained when the diffusive flux $D\frac{C_{ss}}{\bar{x}_f}$ balances the injected flux F. The transition occurs at $Dt_0 = \frac{4}{\pi}\bar{x}_f{}^2$. Results for an exponential profile are given in Appendix AIV.1.

The other interesting situation is when R and C_0 determine the interfacial flux, while the contribution from f is negligable. The solution of the PDE in this case gives

$$\hat{Q}(s) = C_0 R \frac{1}{s^{3/2}} \frac{1}{s^{1/2} + R/\sqrt{D}} \qquad (9a)$$

for which

$$Q(t) = \frac{2}{\sqrt{\pi}} C_0 (Dt)^{1/2} + C_0 \frac{D}{R} \left[e^{\frac{R^2}{D} t} \operatorname{erfc} \left(\frac{R^2}{D} t \right)^{1/2} - 1 \right] \qquad (9b)$$

The reaction rate R limits the transport at low fluences and $Q(t) \sim C_0 R t \cdot \left[1 - O(\frac{R^2}{D} t)^{1/2} \right]$. The first term dominates when diffusion limits the transport at large t after $C(0^+,t) \rightarrow C_0$. The transition occurs at $R^2 t_0 = \frac{4}{\pi} D$.

Both of these cases simulate the dose dependence observed for the mixing in M/SiO_2 induced by Xe irradiation at 25, and 300C. Setting aside doubts about the validity of this type of model, is it possible to distinguish these two cases on the basis of their dose dependence $Q(\Phi)$, which alone can be measured accurately? One approach to the problem is to find those $f(x)$ which would produce indistinguishable behavior. This condition is satisfied by setting Eqn. 8a equal to Eqn. 9a;

$$C_0 R \frac{1}{s^{3/2}} \frac{1}{s^{1/2} + R/\sqrt{D}} = \int_0^\infty \frac{1}{s^2} \left[1 - e^{-\eta \frac{s^{1/2}}{\sqrt{D}}} \right] f(\eta)\, d\eta$$

Rearrangment with the substitution $z = s^{1/2}/\sqrt{D}$ gives

$$C_0 R \frac{z}{z + R/D} = \int_0^\infty \left[1 - e^{-z\eta} \right] f(\eta)\, d\eta$$

This expression produces the expected relationship $\int_0^\infty f(\eta)\, d\eta = C_0 R$ in the limit $z \rightarrow \infty$. Thus;

$$\int_0^\infty f(\eta)\, e^{-z\eta}\, d\eta = C_0 R \frac{R/D}{z + R/D}$$

Inversion of this Laplace transform gives the exponential solution $f(x) = C_0 R \cdot \frac{R}{D} e^{-\frac{R}{D} x}$ as the injection profile which would produce mixing $Q(t)$

with a dose dependence identical to that for an interfacial reaction. This also happens to be a very good description of the low-energy secondary recoil profile [16]. $Q(t)$ given by Eqn. 8b is not very sensitive to variations in the higher moments of $f(x)$. Eqn. 7 shows that the first moment can only distinguish between the limiting cases for small t. All mechanisms will, of course, look the same after diffusion limits transport.

3. Comparison With Experiment

It was previously shown that the deep recoil tail is not significantly altered by diffusional mixing in our experiments. Consequently, $[M]_s$ consists of the contribution from the shallow peak plus the linear primary recoil yield. The dose dependence predicted by these models can be described by the equation

$$[Ni]_s \Phi^{-\frac{1}{2}} = A_1 \Phi^{\frac{1}{2}} + A_2 h(A_3 \Phi^{\frac{1}{2}}) \tag{10}$$

where $h(u) = \frac{2}{\sqrt{\pi}} + \frac{e^{u^2}\operatorname{erfc} u - 1}{u}$. A_1 is the primary recoil yield. $A_2 = C_0\sqrt{D}$, or $\frac{F\bar{x}_f}{\sqrt{D}}$ and $A_3 = \frac{R}{\sqrt{D}}$, or $\frac{\sqrt{D}}{\bar{x}_f}$ for an interfacial reaction or secondary recoil injection, respectively. The area a of the cascade has been absorbed into the constants D, F, and R. An unconstrained least squares fit of Eqn. 10 to the 25C Ni results gave $A_1 = 0.59$, which is in good agreement with the value 0.65 deduced from the tail. There was a change in the other parameters when A_1 was constrained; $\frac{\Delta A_2/A_2}{\Delta A_1/A_1} = -0.8$, $\frac{\Delta A_3/A_3}{\Delta A_1/A_1} = 1.4$, although this did not significantly alter the goodness of fit for $\Delta A_1 < 0.2$. An unconstrained fit to the 300C data was excellent, except that $A_1 = -1.3$. The initial linear region extends out too far to be accounted for by the model. The values of the parameters deduced by fitting the 25, 300C data with A_1 set to 0.65 are given in Table 1. The fitted curves are compared in Fig. 3 with the experimental results. D was calculated from the

Table I. Parameters deduced from fitting Equations 7 and 10 to experimental results for 25 and 300°C Xe irradiation of 25nm Ni/SiO_2 samples .

Parameter	Units	Temperature	
		25°C	300°C
Injection			
F		6.2	2.3
$\bar{x}_f$	nm	2.5	6.4
D	$nm^2/10^{15}cm^{-2}$	58	79
Interfacial reaction			
C_0	$10^{21}cm^{-3}$	2.3	1.3
R	$nm/10^{15}cm^{-2}$	27	17
D	$nm^2/10^{15}cm^{-2}$	83	154

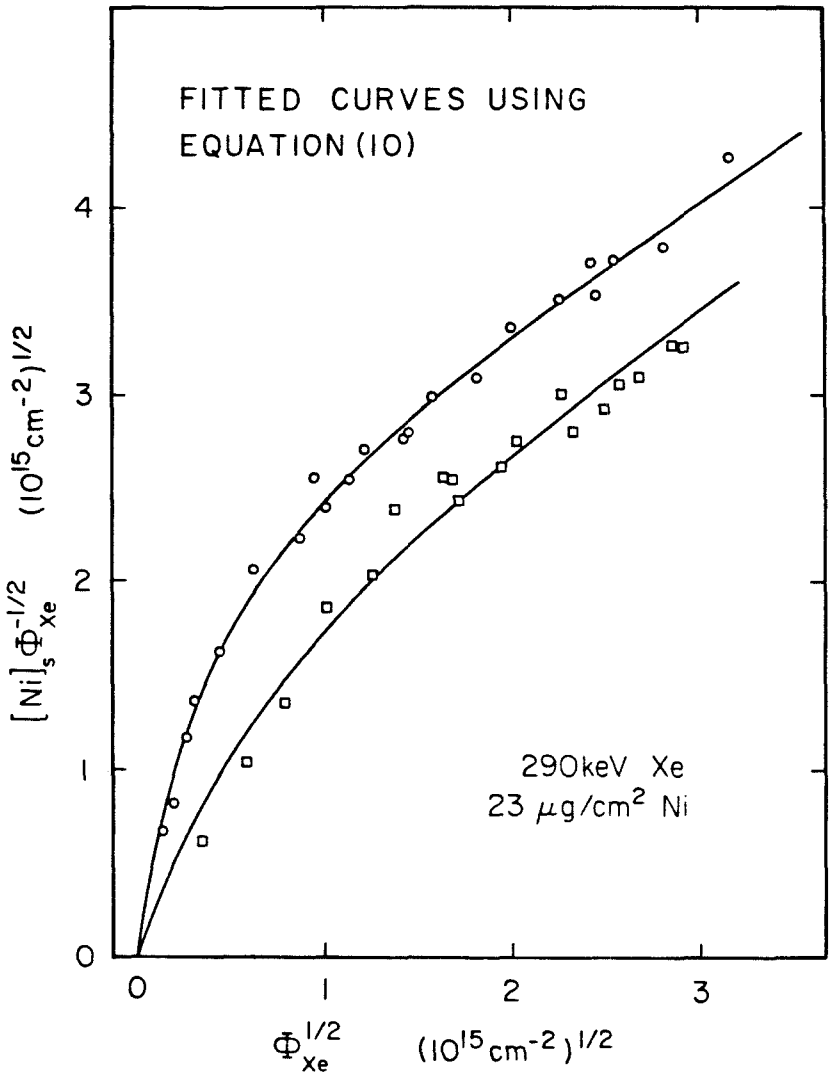

Figure 3. Fit of Equation 10 to mixing data for 25°C and 300°C irradiation temperatures.

evolution of the first moment, using Eqn. 7 and the fitted parameters A_2, A_3. Note that the primary recoil term is omitted from Q in fitting Eqn. 7 to the experimental results. Fig. 4 displays the consequence of fitting Eqn. 7 to the data for the two cases. It is evident that the error bars are a bit overwhelming.

The diffusivity calculated for a Ni marker spreading in an SiO_2 matrix under 300keV Xe irradiation is D = 6.8 $nm^2/10^{15}cm^{-2}$ [17]. This is much smaller than that reported in Table 1. for Ni/SiO_2 bilayers. D is often proportional to the energy deposited in elastic collisions F_D [2,4]. The ratio of F_D at the Ni-SiO_2 interface to F_D at the marker in the marker experiment is ~2.8 and therefore does not explain the factor of 10 difference.

The injection limit provides one interpretation of the mixing results. The diffusivity D does not change significantly with irradiation temperature up to 300C. The rate of injection F decreases, while the mean injection depth $\bar{x}_f$ increases with the irradiation temperature. A reliable estimate of F could not be obtained from first principles. Secondary recoil yields tend to vary from 1 - 4 [16,18,19]. The value of F required by the model is slightly greater than one might have expected. The temperature dependence suggests that lower-energy recoils are expelled during the cascade at higher temperatures. Barcz and Nicolet found that the spreading of metal markers in SiO_2 and Al_2O_3 produced by Xe irradiation was not affected by irradiation temperature up to 500C [17,20]. These experiments are also complicated by the formation of precipitates.

The behavior is more complicated when interpreted in terms of an interfacial reaction. The diffusivity D increases with elevation of the irradiation temperature, while both the equalibrium concentration C_0 and the rate constant R decrease. The concentration profile is bounded by $C(x,\Phi) < C_0$ when $f = 0$ in our constant coefficent diffusion model. Nevertheless, the observed peak concentration exceeds the calculated value of C_0 for $\Phi > 3x10^{15}cm^{-2}$. The reason for

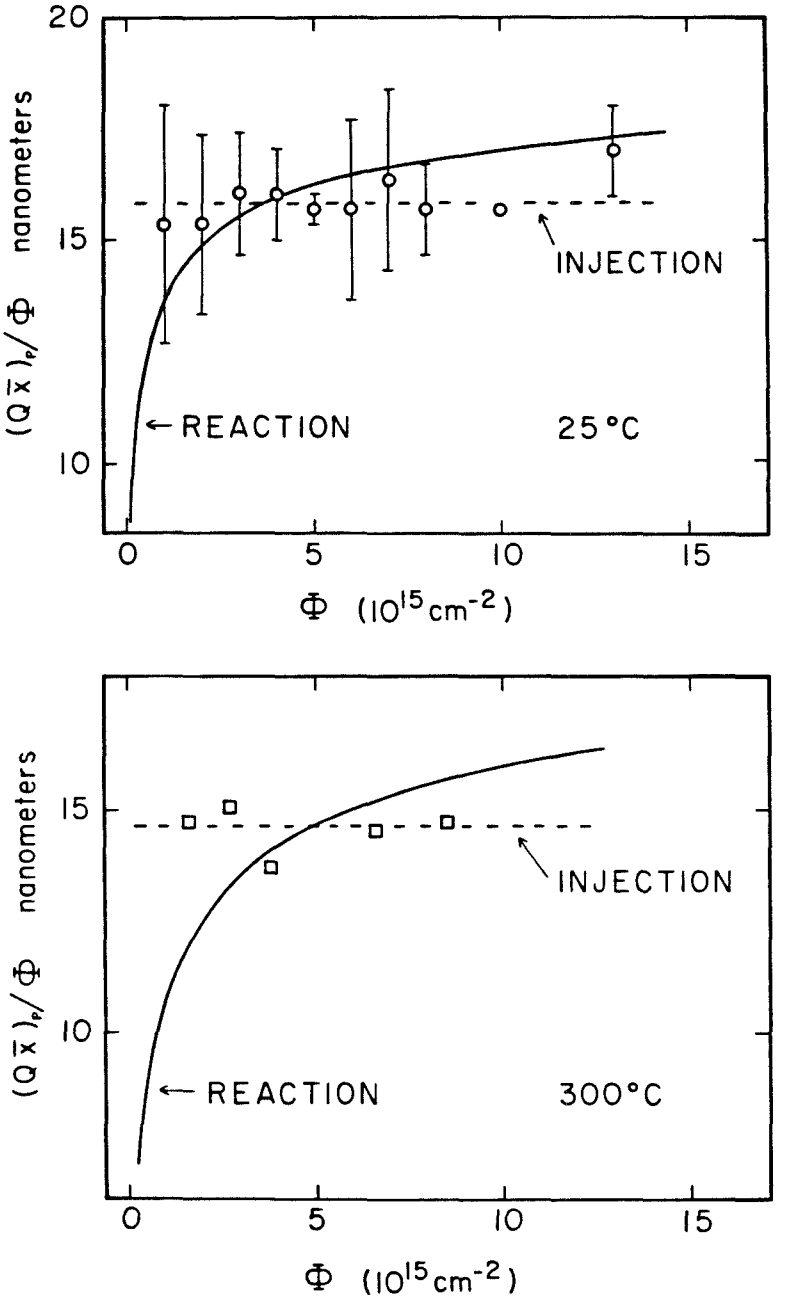

Figure 4. Fit of Equation 7 to the measured (partial) first moment for the two limiting cases .

considering the interfacial reaction is that one could imagine that a large amount of Ni permeates the SiO_2 during the hot part of the cascade. Most of this Ni is expelled as the cascade cools, although a conjectured kinetic limitation may result in the confinement of Ni in some form. The impedance boundary condition is the simplest way to incorporate an interaction between metal film and SiO_2.

4. Sequential Irradiation

The model can also be used to calculate the mixing behavior for a sample irradiated first at one temperature, and then again at another temperature. We shall examine the following sequence: The sample is irradiated to a dose t_1 at a temperature T_1. The model parameters at this temperature are C_{01}, $f_1(x)$, etc. The concentration $C(x,t_1)$ after t_1 becomes the initial condition for the second irradiation at temperature T_2 (parameters C_{02}, $f_2(x)$, etc.) to a dose t_2.

The impedance boundary condition is the first of the two limiting cases to be discussed. $f(x)$ is assumed to be negligable. The second PDE can be separated into an initial value problem and a coupled boundary value problem, both of which can be solved using Laplace transforms taken in t. The resulting net yield is given by

$$Q_{12} = Q_1(t_1) + Q_2(t_2) - C_{01}\int_0^\infty h\left(\eta\frac{R_1}{D_1}, \frac{R_1^2}{D_1}t_1\right) h\left(\eta\frac{R_2}{D_2}, \frac{R_2^2}{D_2}t_2\right) d\eta \qquad (11)$$

where

$$h(u,v) = \operatorname{erfc}\frac{u}{2\sqrt{v}} - e^{u+v}\operatorname{erfc}\left[\frac{u}{2\sqrt{v}} + \sqrt{v}\right]$$

and Q_1, Q_2 are given by Eqn. 9b with the appropriate parameters for T_1, T_2, respectively. The third term represents the compensation required to

accommodate different steady-state conditions at the interface. A analogous expression holds if the sequence is reversed. The difference between the two sequences is

$$\Delta Q(t_1,t_2) = Q_{12} - Q_{21} = (C_{02} - C_{01}) \int_0^\infty h(1)h(2)d\eta$$

This can be simplified in the diffusion limit when $R^2t > \frac{4}{\pi}D$, since $h(u,v) \sim \text{erfc}\, \frac{u}{2\sqrt{v}}$ as $v \to \infty$. The result of performing the integration in this limit is

$$\Delta Q \simeq (C_{02} - C_{01}) \cdot \frac{2}{\sqrt{\pi}} \left[(D_1t_1 + D_2t_2)^{1/2} - (D_1t_1)^{1/2} - (D_2t_2)^{1/2} \right] \qquad (12)$$

This can also be simply derived using superposition when $R \to \infty$. If $t_1 = t_2 = \frac{1}{2}t$, then

$$\frac{\Delta Q(t)}{Q_1(t)} \simeq \frac{1}{\sqrt{2}} \left[\frac{C_{02}}{C_{01}} - 1 \right] \left[1 + \left[\frac{D_2}{D_1} \right]^{1/2} - \left[1 + \frac{D_2}{D_1} \right]^{1/2} \right] \qquad (13)$$

The term in brackets does not vanish for finite D's and is ~0.6 for $D_2 = D_1$. Clearly, $\Delta Q = 0$ only if $C_{02} = C_{01}$, with the additional consequence that

$$Q_{12}^2 = Q_{21}^2 \simeq \tfrac{1}{2}Q_1(t)^2 + \tfrac{1}{2}Q_2(t)^2 \qquad (14)$$

The 25C - 300C mixed-temperature experiments showed that $\Delta Q / Q < 0.04$ if the deep primary recoil yield is independent of temperature. Eqn. 13 predicts that $\frac{C_{02}}{C_{01}} = 0.95 \pm 0.05$. This is certainly inconsistant with the results for C_0 in Table 1. The solid line in Fig. 20 of chapter III was obtained using Eqn. 14, although this result is barely distinguishable from the algebraic mean of the 25C and 300C curves.

The other case when injection dominates, so that $C_{01} = C_{02} = 0$ and $R_1, R_2 \to \infty$, is a bit more complicated. A straightforward solution of the two PDE's, by taking a double Laplace transform in t_1, t_2, produces;

$$\Delta Q = \frac{1}{2\pi i}\int_{-i\infty}^{+i\infty} ds\, e^{sD_2t_2}\, \frac{1}{2\pi i}\int_{-i\infty}^{+i\infty} dz\, e^{zD_1t_1} \int_0^{\infty} d\eta \left[\frac{f_2(\eta)}{D_2} - \frac{f_1(\eta)}{D_1}\right] \frac{e^{-\eta s^{1/2}} - e^{-\eta z^{1/2}}}{sz\,(z-s)}$$

The dominant contribution to the asymptotic representation in the long-time diffusion limit comes from the s, $z \to 0$ behavior of the third integral [15]. A simple expansion gives $\frac{e^{-\eta s^{1/2}} - e^{-\eta z^{1/2}}}{sz\,(z-s)} \simeq \frac{\eta}{sz\,(s^{1/2}+z^{1/2})} - O(\frac{\eta^2}{sz})$ for small s, z. The result from taking the inverse transforms with this approximation is

$$\Delta Q(t_1,t_2) \sim \frac{2}{\sqrt{\pi}}\left[(D_1t_1)^{1/2} + (D_2t_2)^{1/2} - (D_1t_1 + D_2t_2)^{1/2}\right]\left[\frac{(F\bar{x}_f)_2}{D_2} - \frac{(F\bar{x}_f)_1}{D_1}\right] \quad (15)$$

which is analogous to Eqn. 12, as might be expected for diffusion. The moment analysis interpreted using Eqn. 7 suggests that the change in $F\bar{x}_f$ between 25C and 300C is less than 10%. ΔQ is therefore relatively small in this case if we accept that the temperature dependence of D is not very great below 300C. The clusters certainly affect the Ni movement at higher temperatures. We can not reject the hypothesis that the major contribution to the shallow peak is from secondary recoils. There is some theoretical evidence which indicates that the secondary recoil yield is proportional to F_D at the bilayer interface [21,22]. This could explain the correlation between Q_M and F_D, shown in Fig. 11 of Chapter III.

E. Thin SiO_2 Layer

The boundary condition at the Ni-SiO_2 interface is the same as before,in Eqn. 5. Let $x = L$ correspond to the SiO_2-Si interface. The boundary condition at this interface can be approximated by $C(L,t) = 0$, since Si is a very effective

sink for Ni if we neglect the kinetics of NiO dissociation. The two limiting cases of secondary recoil injection and an interfacial reaction are illustrated in Fig. 5. The derivation of the solution to each of these cases follows from an unexciting application of techniques previously employed. The Laplace transform taken in t of $Q(t)$, the net yield of metal atoms moving across the interface at $x = 0$ into the SiO_2, for injection with $C_0 = 0$, $R \to \infty$ is

$$\hat{Q}(s) = \frac{1}{s^2}\int_0^L d\eta\, f(\eta)\left[1 - \frac{\sinh(L-\eta)s^{1/2}}{\sinh Ls^{1/2}}\right] - \frac{1}{s^2}\int_L^\infty d\eta\, f(\eta) \qquad (16)$$

Please note that this also includes the flux of metal atoms into the Si. The interesting asymptotic behavior is

$$Q(t) \sim Ft \quad \text{for } t \to 0 \qquad (17a)$$

$$Q(t) \sim Ft - t\int_0^L f(\eta)\left(1 - \frac{\eta}{L}\right) d\eta \quad \text{for } t \to \infty \qquad (17b)$$

The additional term for $t \to \infty$ represents the steady diffusive flux of metal back to the Ni-SiO_2 interface. Eqn. 17b gives $Q(t) \sim F \cdot \frac{\bar{x}_f}{L}\left(1 - e^{-L/\bar{x}_f}\right)$ for an exponential profile $f(x) = \frac{F}{\bar{x}_f} e^{-L/\bar{x}_f}$. A constrained fit of Eqn. 10 to the thick SiO_2 data reported in Fig. 19 from Chapter III with $A_1 = 0.5$ produced the parameters F = 5.7, and $\bar{x}_f$ = 3.3 nm. The initial linear region again extends out a bit farther than the model reasonably accounts for. The slope predicted for secondary recoil injection with these parameters, including primary recoils which are ignored in Eqn. 16, for L = 5 nm is 2.9 + 0.5 = 3.4. This is in favorable agreement with the experimentally observed value of 3.65 reported in Fig. 19 for the 20nm Ni/5nm SiO_2/Si samples.

An asymptotic expression for the long time behavior when the reaction

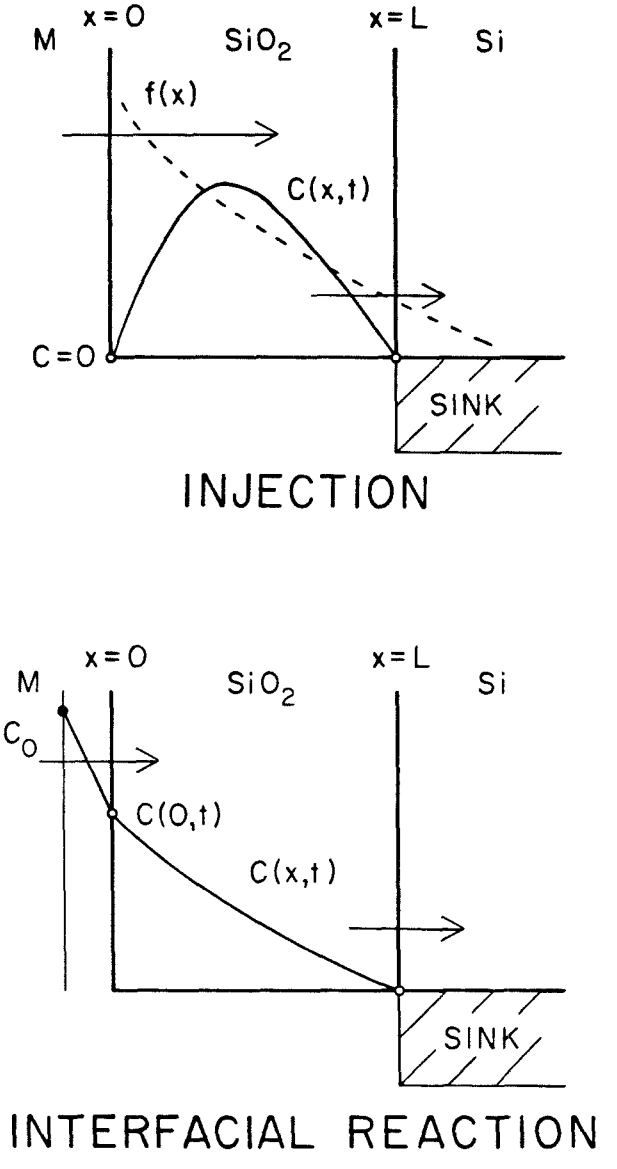

Figure 5. Illustration of limiting cases for injection and interfacial reaction with a sink at $x = L$.

limits the mixing can be deduced from the condition that the flux $-D\frac{\partial C}{\partial x}$ is constant inside the SiO_2 at steady state. The result for $Q(t)$ is

$$Q(t) \sim \frac{D}{D + LR} C_0 R t \quad \text{for } t \to \infty \tag{18}$$

The short time behavior is the same as that for a thick oxide. The slope predicted by Eqn. 18 for the yield in the thin oxide experiment is only 3.0, using the value of D for 25C from Table 1. The initially high slope predicted by either model is not actually observed in the experiment. Neither model nor experiment is reliable enough to identify which could be responsible for the discrepancy.

F. Other Models - Tidal Model

The following models derive from an extension of the mixed temperature experiment. Suppose that the Ni film acts as a diffusion source of Ni during the "hottest" portion of the cascade. The interface becomes a sink when the cascade cools, and eventually the concentration profile is frozen in. The motion within the hottest part of the cascade might be described by $\frac{\partial C}{\partial t} = D_h(t)\frac{\partial^2 C}{\partial x^2}$, with $C(0^+,t) = C_h$ for $0 < t \le t_h$, where t_h is the duration of the hot part. The retreat during the cooling $0 < t \le t_c$ would follow $\frac{\partial C}{\partial t} = D_c(t)\frac{\partial^2 C}{\partial x^2}$ with $C(0^+,t) = 0$, and the initial condition $C(x,t_h)$ from the previous period. In both cases the physical interval is $0 \le x < \infty$. Since experimentally there is not much metal in the SiO_2, we can assume $\tau_h \equiv \int_0^{t_h} D_h(t)\,dt < \tau_c \equiv \int_0^{t_c} D_c(t)\,dt$. The yield for a single cascade can be deduced from Eqns. 11,12 or by superposition;

$$Q_1 = \frac{2}{\sqrt{\pi}} C_h \left[(\tau_h + \tau_c)^{1/2} - \tau_c^{1/2} \right]$$

The profile for n overlapping cascades can be obtained using superposition. The result for $n \geq 1$ is

$$Q_n = \frac{2}{\sqrt{\pi}} C_h \sum_{k=1}^{n} \left([k(\tau_h + \tau_c)]^{1/2} - [k(\tau_h + \tau_c) - \tau_h]^{1/2} \right)$$

$$\sim \frac{2}{\sqrt{\pi}} \frac{C_h \tau_h}{\tau_h + \tau_c} (\tau_h + \tau_c)^{1/2} \tfrac{1}{2} \sum_{k=1}^{n} k^{-1/2} \quad \text{for } \tau_h \ll \tau_c$$

This looks like diffusion from a surface source with concentration $\frac{C_h \tau_h}{\tau_h + \tau_c}$. The last sum approaches $2n^{1/2} - 0(1)$ for large n. The model can be generalized to include an arbitrary profile $h(x)$ produced during the hot part of the cascade rather than just a diffusion profile. In this case $Q_1 = \int h(x)\,dx$, while the effective surface concentration becomes $\tau_c^{-1} \int h(x)\, x\, dx$. It was shown in Section C that these models give a fortuitously good fit to the experimental results...

References

[1] J. W. Mayer, B. Y. Tsaur, S. S. Lau and L. S. Hung, *Nucl. Instr. and Meth.* **182/183**, 1 (1981)

[2] P. Sigmund and A. Gras-Marti, *Nucl. Instr. and Meth.* **182/183**, 25 (1981)

[3] W. L. Johnson, Y. T. Cheng, M. Van Rossum and M-A. Nicolet, *Nucl. Instr. and Meth.* **B7/8**, 657 (1985)

[4] B. M. Paine and R. S. Averback, *Nucl. Instr. and Meth.* **B7/8**, 666 (1985)

[5] W. L. Johnson in *Proceedings of the Second Workshop on Ion Mixing and Surface Layer Alloying*, D. M. Follstaed, R. S. Averback and M-A. Nicolet, eds. (Sandia National Laboratory, NM, 1986), 32

[6] G. J. Dienes and A. C. Damask, *J. Appl. Phys.* **29**, 1713 (1958)

[7] R. S. Averback, L. J. Thompson, Jr., J. Moyle and M. Schalit, *J. Appl. Phys.* **53**, 1342 (1982)

[8] T. C. Banwell, M-A. Nicolet, R. S. Averback and L. J. Thompson, *Appl. Phys. Lett.* , accepted for publication (1986)

[9] F. Daniels and R. A. Alberty, *Physical Chemistry* (Wiley, New York, 1975), 319

[10] N. G. van Kampen, *Stochastic Processes in Physics and Chemistry* (North-Holland, New York, 1983)

[11] R. Ghez, J. D. Fehribach and G. S. Oehrlein, *J. Electrochem. Soc.* **132**, 2759 (1985)

[12] G. F. Carrier, M. Krook and C. E. Pearson, *Functions of a Complex Variable* (McGraw-Hill, New York, 1966)

[13] We shall adopt the notation:

$$\hat{f}(s) = \int_0^\infty f(t)\, e^{-st}\, dt$$

$$f(t) = \frac{1}{2\pi i} \int_B \hat{f}(s)\, e^{st}\, ds \quad .$$

An extensive compilation of transform pairs can be found in: G. E. Roberts and H. Kaufman, *Table of Laplace Transforms* (Saunders, Philadelphia, 1966)

[14] $$\int_0^1 \operatorname{erf} \frac{x}{\sqrt{\xi}}\, d\xi = (1 + 2x^2) \operatorname{erf} x + \frac{2}{\sqrt{\pi}} x e^{-x^2} - 2x\,|x| \quad .$$

[15] D. V. Widder, *The Laplace Transform* (Princeton University Press, Princeton, 1941)

[16] L. A. Christel, J. F. Gibbons and S. Mylroie *Nucl. Instr. and Meth.* **182/183**, 187 (1981)

[17] A. J. Barcz, B. M. Paine and M-A. Nicolet, *Appl. Phys. Lett.* **44**, 126 (1984)

[18] J. Delafond, S. T. Picraux and J. A. Knapp, *Appl. Phys. Lett.* **38**, 237 (1981)

[19] B. Maillot and M. Bruel, *Nucl. Instr. and Meth.* **209/210**, 707 (1983)

[20] A. J. Barcz and M-A. Nicolet, *Appl. Phys.* **A 33**, 167 (1984)

[21] G. Falcone and A. Oliva, *Appl. Phys. Lett.* **42**, 41 (1983)

[22] G. Fischer, G. Carter and R. Webb, *Radiat. Effects* **38**, 41 (1978)

Chapter V Primary Recoil Profiles and Related Problems

A. Introduction

The deep tail was a pronounced feature in all of the implanted samples and was usually recognizable by RBS without etching. This tail was attributed to recoil implantation. The literature on this subject is quite extensive [1-10]. In traversing the metal film, the incident ion collides with atoms in the film. These primary collisions are a source of energetic atoms, which in turn collide with yet other target atoms. The secondary collisions produce many more lower energy recoils. The direction of the primary recoils is anisotropic due to the correlation with the incident ion's initial momentum [2]. This correlation is lost after a few generations within the cascade, so that the directions of the secondary recoils is nearly isotropic [6]. The recoiling atoms come to rest at new locations depending on their aquired energy T and initial direction. Imagine, if you will, a metal layer of thickness L on top of a thick substrate such as SiO_2. We shall be concerned with the profile of the metal atoms $f(x)$ in the substrate resulting from recoil implantation induced by an ion with energy E_0 hitting this sample at normal incidence. Primary collisions determine the profile $f(x)$ with thin layers; $L < R_p$ where R_p is the projected range of the incident ion in the metal film. The profile is dominated by secondary recoils for thick layers [7].

The principle difficulty in calculating the recoil profile $f(x)$ arises from the fact that the recoiling atoms travel through two different media; the source and the substrate. The relocation profile for a particular displaced atom is determined by the energy loss, which is dominated by nuclear scattering at the

energies of interest here, and the angular deflections. The differences in mass and density can be factored out from the scattering cross-section, but not from the deflections. Additionally, an atom ending its flight near the interface may traverse several times before coming to rest. The straggling of the incident beam in the source layer complicates the problem for thin source layers. The corresponding difficulty with thick films is that the energy spectrum of the recoiling atoms is not understood well enough. The results presented in Chapter III are for samples in the thin film catagory. We shall therefore focus on this regime.

B. Primary Recoil Profiles for a Thin Source Layer

Fig. 1 illustrates the processes affecting the recoil profile with some of the difficulties accentuated. A number of approximations will be invoked to make the problem tractable. We shall neglect incident beam straggling for $L < 0.7R_p$. Some justification for this can be found in appendix AV.2. Secondary recoils will be omitted, since it is assumed that primary recoils dominate anyway. The major approximation concerns the range distribution in a bilayer medium. It will be assumed that there exists a length scaling factor which makes the source film look like the substrate. This is not true as the angular scattering is usually different. Discussion of this approach can be found in appendix AV.1, when the moving atom crosses the interface only once. The less exciting problem we shall consider is illustrated in Fig. 2. An extensive discussion of this problem has been given by Kelly, et al. [2,3]. The present calculation differs from theirs in the choice of the relocation profile for a bilayer medium.

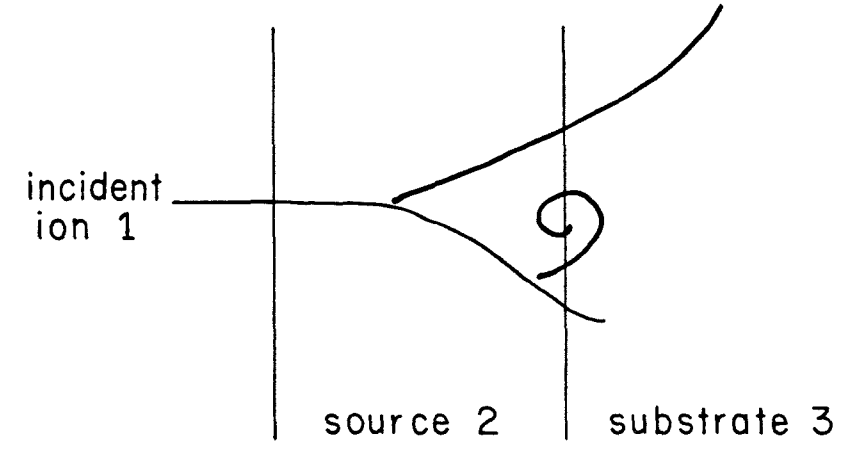

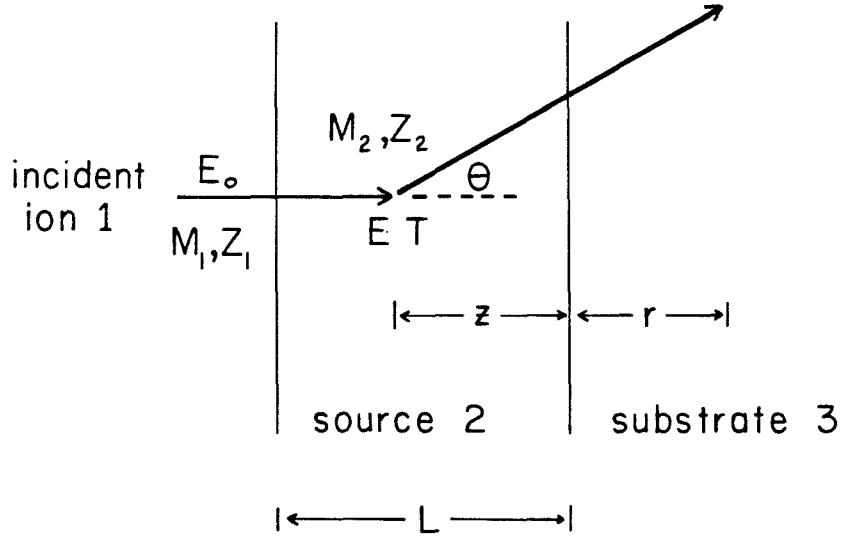

Figure 1. (Top) Illustration of recoil implantation problem with sources of difficulty accentuated.

Figure 2. (Bottom) Illustration of simpler problem treated in text.

C. Calculation

We shall denote the incident ion by the index 1, the source film by 2, and the substrate by 3. The recoiling atoms of interest will also be denoted by 2, although there is nothing to preclude considering a multi-component source layer. The events leading to the primary recoil profile will be decomposed into three components; dissipation of the incident ion's energy in traversing a distance $L - z$, collision of the incident ion with atom 2 in the source layer at z, resulting in the transfer of kinetic energy T to this atom, and finally the relocation of 2 into substrate 3 to a depth r.

1. Incident Ion Energy Loss

The length s of an ion's trajectory in a solid is nearly proportional to its initial energy E_0 [11]. One can conclude from this that the rate of energy loss $\frac{dE}{ds}$ is fairly constant over a wide energy range. The average energy of the incident ion at a depth $L - z$ in the source film is therefore;

$$E(z) = E_0 - S_{12}(L - z) \tag{1}$$

where $S_{12} = \frac{dE}{ds}$ for 1 in 2 evaluated at about E_0. Energy straggling will also be neglected.

2. Scattering

The scattering process is determined by the screened Coulomb interaction of 1 and 2. The scattering angle θ of 2 is correlated with its aquired energy T by conservation of energy and momentum;

$$T = \gamma_{12} E(z) \cos^2\theta \tag{2}$$

where $\gamma_{12} = \frac{4M_1M_2}{(M_1 + M_2)^2}$. Scattering is a stochastic process. If a fluence Φ of incident ions passes through a region dz at a depth z, then the number of collisions resulting in a transfer of energy T can be written as $\Phi d\sigma_{12}(T,E)\cdot\rho_2 dz$, where ρ_2 is the density of 2 in the source layer and $d\sigma_{12}$ is the scattering cross-section. The scattering cross-section for Thomas-Fermi screening can be represented by [12]

$$d\sigma_{12}(T,E) = \pi a^2 \frac{f(t^{1/2})}{2t^{3/2}} dt \tag{3}$$

where

$$a = 0.8853 a_0 (Z_1^{2/3} + Z_2^{2/3})^{-1/2}$$

$$a_0 = 0.0529\text{nm} \quad (\text{Bohr radius})$$

$$t = \varepsilon^2 \left(\frac{T}{T_M} \right)$$

$$\varepsilon = C_\varepsilon E$$

$$C_\varepsilon = \frac{M_2}{M_1 + M_2} \left(\frac{Z_1 Z_2 e^2}{a} \right)^{-1}$$

and

$T_M = \gamma_{12} E$ is the maximum energy transfer in a collision .

Another representation is given by the power law approximation [11]

$$f(\varepsilon\sqrt{T/T_M}) \simeq \frac{\lambda_m}{(\varepsilon\sqrt{T/T_M})^{2m-1}} \tag{4}$$

where the power m and constant λ_m depend on the reduced energy ε. $m \simeq 0.5$ for hundred keV Xe in most solids, and $\lambda_{1/2} = 0.327$ [12]. The reader might notice

that the representation given by Eqn. 4 can not be deduced mathematically from the previous equations without introducing physical arguments.

3. Relocation Profile

This is where the problem gets messy. Fig. 3a illustrates an atom with energy T starting at z in 2 along the normal and stopping at x in 3. If both materials are the same as 2, then $\langle x \rangle + z = g_{22} T$ where $\langle x \rangle$ is the mean value of x, and the factor g_{22} varies slowly with T. Likewise, if they are both the same as 3, then $\langle x \rangle + z = g_{23} T$. g_{22} and g_{23} characterize the interaction of atom 2 with the layers 2 and 3, respectively [13]. Appendix AV.1 shows that g is an appropriate scaling factor and to first approximation

$$\langle x \rangle = g_{23} T - \frac{g_{23}}{g_{22}} z \tag{5}$$

This is a very good approximation if the atom crosses the interface exactly once. The straggling is more complicated. We shall assume that $\sigma_x \equiv \sqrt{\langle x^2 \rangle - \langle x \rangle^2} = h_{23} T$, and $\sigma_y \equiv \langle y^2 \rangle^{1/2} = \hat{h}_{23} T$, where h_{23} and $\hat{h}_{23}$ also vary slowly with T [13]. This presumes that these fluctuations also scale with g.

If the atom 2 starts at an angle $\theta \neq 0$, rather than with normal incidence, then the effective projected range $g_{23} T$ will be reduced by $\cos\theta$ while the range straggling will be a weighted quadratic sum of the two components σ_x and σ_y as shown in Fig. 3b;

$$\langle r \rangle(\theta) = g_{23} T \cos(\theta) - \frac{g_{23}}{g_{22}} z \tag{6a}$$

$$\sigma_r^2(\theta) = h_{23}^2 T^2 \cos^2(\theta) + \hat{h}_{23}^2 T^2 \sin^2(\theta) \tag{6b}$$

Finally, we shall assume that the relocation distribution of atom 2 in 3 is Gaussian with parameters given by Eqns. 6a,b. This is valid for a homogeneous target

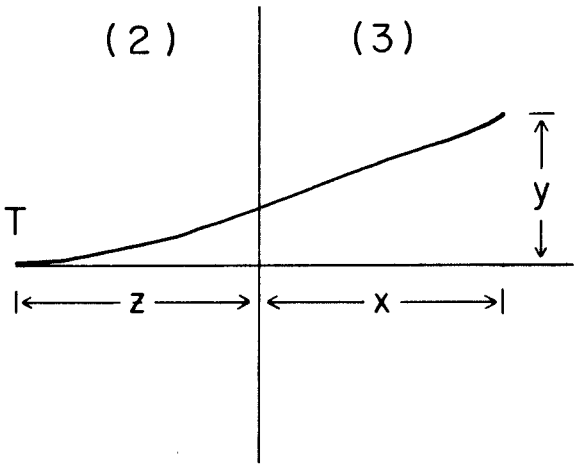

(a)

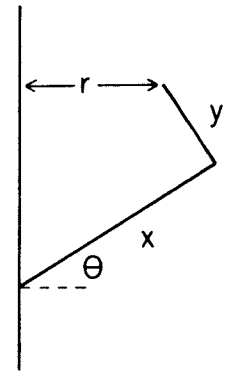

r , x , y are random variables ;

assume $\langle y \rangle = 0$.

$$r = x \cos\theta - y \sin\theta$$

$$\langle r \rangle = \langle x \rangle \cos\theta$$

$$\langle r^2 \rangle = \langle x^2 \rangle \cos^2\theta + \langle y^2 \rangle \sin^2\theta$$

(b)

Figure 3. (a) Definition of terms to describe relocation profile.
(b) Mean and variance for non-normal incidence.

with θ not too large [2,14]. The conditional distribution of recoils at r in 3, given that they start at z in in the source film with energy T in a direction θ, is consequently

$$F(r\,|\,z,T,\theta) = \frac{1}{\sqrt{2\pi}\sigma_r(\theta)} e^{-(r - \langle r\rangle(\theta))^2/2\sigma_r^2(\theta)} \tag{7}$$

Primary Recoil Profile in Substrate

Following the trajectory shown in Fig. 2, the profile of recoils residing in the substrate is

$$f(r) = \Phi\rho \int_0^L dz \int_{0<T<\gamma E(z)} d\sigma_{12}(T,E(z))\; F(r\,|\,z,T,\theta) \tag{8}$$

where unambiguous subscripts have been suppressed. A useful simplification is obtained with the change of variable $\eta = \cos^2\theta = \frac{T}{T_M}$. Using η as the independent variable with Eqn. 2 and 3 or 4 gives

$$d\sigma_{12} = \frac{C_{1/2}}{\gamma^{1/2}} \frac{f(\varepsilon\sqrt{\eta})}{\lambda_{1/2}} \frac{d\eta}{E\eta^{3/2}} \tag{9a}$$

$$d\sigma_{12} = \frac{C_m}{\gamma^m} \frac{d\eta}{E^{2m}\eta^{1+m}} \quad \text{power law approximation}, \tag{9b}$$

where $C_m = \frac{\pi}{2}\lambda_m a^2 \left[\frac{M_1}{M_2}\right]^m \left[\frac{2Z_1Z_2e^2}{a}\right]^{2m}$. This is the cross-section seen by the incident ion per source atom 2 for these atoms scattering into η, $d\eta$. We shall examine the analytical structure of Eqn. 8 using the power law approximation. The behavior for the universal cross-section is not fundamentally different. Combining Eqns. 1,6,8,9a gives

$$f(r) = \frac{\Phi}{2\pi} \frac{\rho C_m}{\gamma_{m+1} S_{12} h_{23}} \int_{E_i}^{E_0} \frac{dE}{E^{2m+1}} I(u;A,B) \tag{10}$$

where $E_i = E_0 - S_{12}L$ is the incident ion energy as it arrives at the source-substrate interface. Clearly, the loss $S_{12}L$ must not exceed E_0! The interesting integral is

$$I(u;A,B) = \int_1^\infty d\xi \, \frac{\xi^m}{[1 + B(1-\xi^{-1})]^{1/2}} e^{-A\frac{(u\xi - \xi^{-1/2})^2}{1 + B(1-\xi^{-1})}} \tag{11}$$

where $A = \frac{g_{23}^2}{2h_{23}^2}$ describes the relative width of the relocation profile. Typically, $A \gg 1$. The parameter $B = \frac{\hat{h}_{23}^2}{h_{23}^2} - 1$ describes the eccentricity of the component profiles. The substitution $\xi = \eta^{-1}$ was chosen to obtain more convenient limits of integration. The variable

$$u = u(r,E) = \frac{r}{g_{23}\gamma E} + \frac{(E - E_i)/S_{12}}{g_{22}\gamma E}$$

represents the scaled distance from z to r relative to the mean distance in 3 traveled for a given energy $T = \gamma E$. u is a convenient dimensionless depth scale somewhat analogous to r. The E dependence is not very strong for small L, consequently $I(u)$ can be considered as a first-order description of the recoil profile.

5. Asymptotic Behavior

The spatial structure of the profile $f(r)$ is primarily determined by the competition in the exponent of Eqn. 7. A large contribution to $f(r)$ comes from T (or equivalently θ), such that $<r>$ is near r, or else σ_r is large. The argument in the exponent of Eqn. 11 has a saddle point at $\xi = u^{-2/3}$ for $u < 1$, and is monotone increasing in ξ for $u > 1$ and $B < 2$. Laplace's method for fixed u with $A \to \infty$ gives;

$$I(u;A,B) \sim \frac{2\pi^{1/2}}{3}\frac{u^{-1-2m/3}}{A^{1/2}}\left[\,1 + O\left(\frac{u^{-2/3}}{A}\right)\right] \quad \text{for } 0<u<<1 \tag{12a}$$

$$\sim u^{-2(m+1)/3}\left\{ \frac{\pi^{1/2}}{3}\frac{u^{-1/3}}{A^{1/2}} \right.$$

$$+ \frac{u^{-2/3}}{9A}\left[1 + B(1-u^{2/3})\right]^{1/2}\left[2m + \frac{1+B}{1+B(1-u^{2/3})}\right]$$

$$\left. + \frac{1-u^{2/3}}{\left[1 + B(1-u^{2/3})\right]^{1/2}} \right\} \quad \text{for } u \simeq 1 \tag{12b}$$

$$\sim \frac{e^{-A(u-1)^2}}{A(u-1)\left[(2-B)(u-1)+3\right]} \quad \text{for } u>>1 \tag{12c}$$

A Taylor expansion for Eqn. 12b in $(1-u^{2/3})$ would be proper; however, it is not very informative, either. The parameter $B = \left[\frac{\sigma_y}{\sigma_x}\right]^2 - 1$ is generally not very large. Fig. 4 illustrates the dependence of σ_y/σ_x versus energy for a number of ions in SiO_2 and Ge. The later resembles Ti, Cr and Ni. These curves were obtained from published range statistics [11,14]. It is evident that this ratio is close to unity for many ion-target combinations. A little more work shows for $B = 0$ and $0<u<1$ that as $A\to\infty$

$$I(u;A,0) \sim \frac{\pi^{1/2}}{3}\frac{u^{-1-2m/3}}{A^{1/2}}\left[2 + \frac{(2m-1)(m+1)}{9Au^{2/3}} + O\left(\frac{1}{A^{3/2}u}\right)\right]$$

The third order term also vanishes for $m = \frac{1}{2}$.

$I(u;A,B)$ is plotted in Fig. 5 for $A = 6.2$, $B = 0$ and $m = \frac{1}{2}$ (Xe into Ni on SiO_2) and in Fig. 6 for $A = 10.7$, $B = 1.903$ and $m = \frac{1}{2}$ (As into SiO_2 on Si with O recoils). The asymptotic behavior is also indicated by dashed lines. It is evident from Figs. 5,6 or Eqn. 12 that this model does not really exhibit an exponential depth dependence. There is a strong dependence upon m for $u<1$,

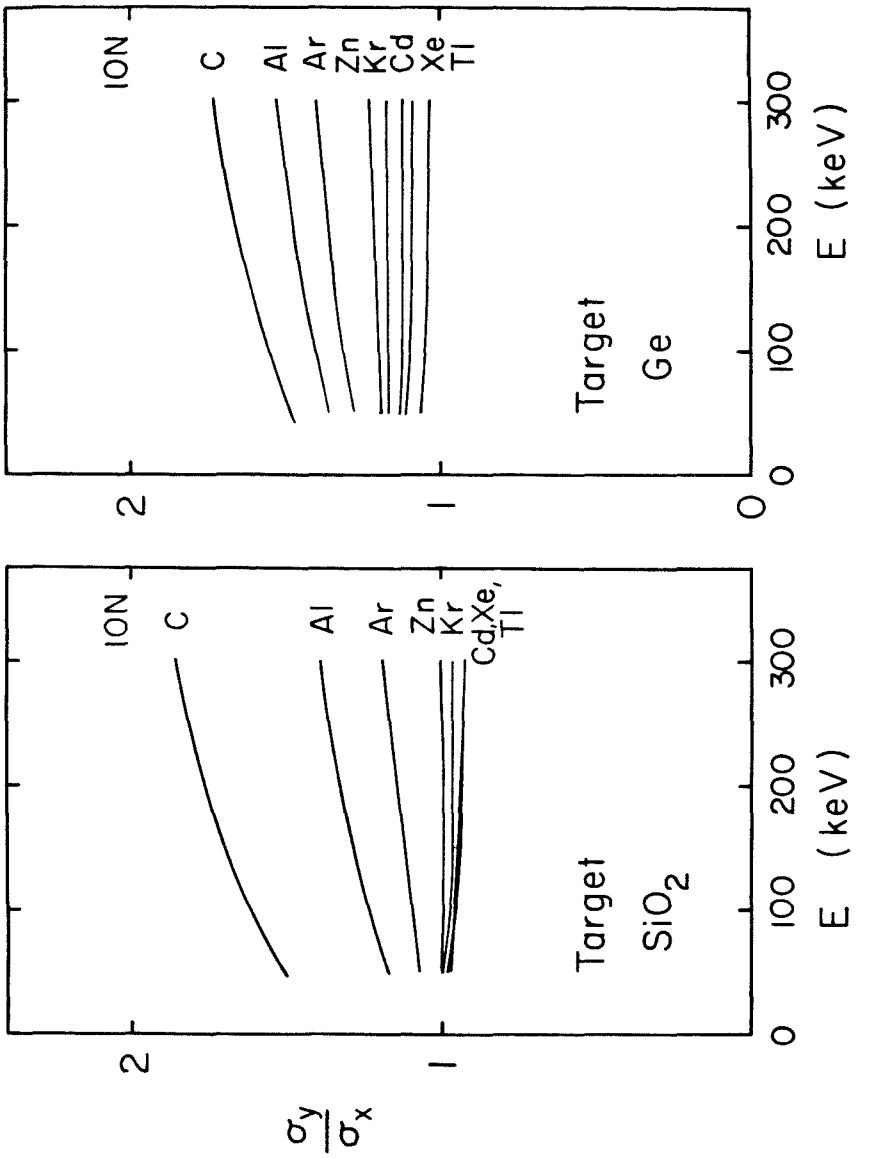

Figure 4. Energy dependence of the ratio σ_y/σ_x for various ions in two targets of practical interest.

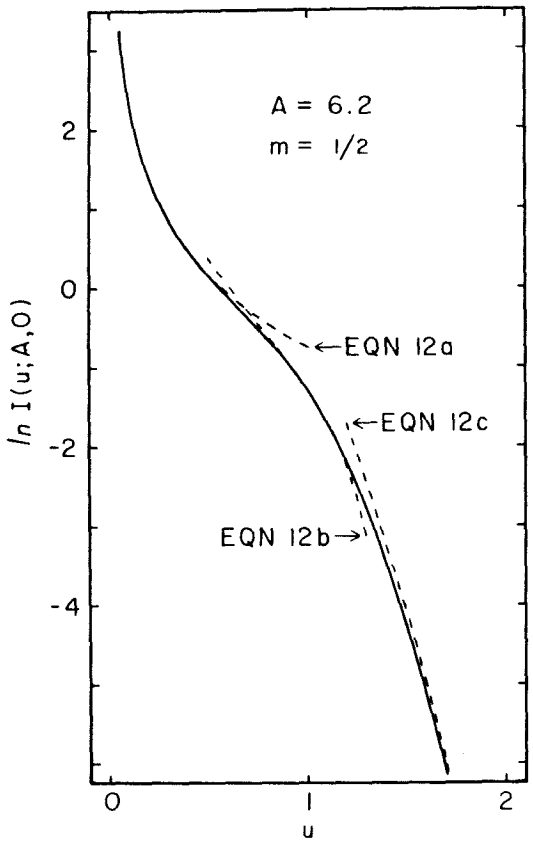

Figure 5. Graph of I(u;A,0) for parameters corresponding to Xe → Ni/SiO_2 with Ni recoils.

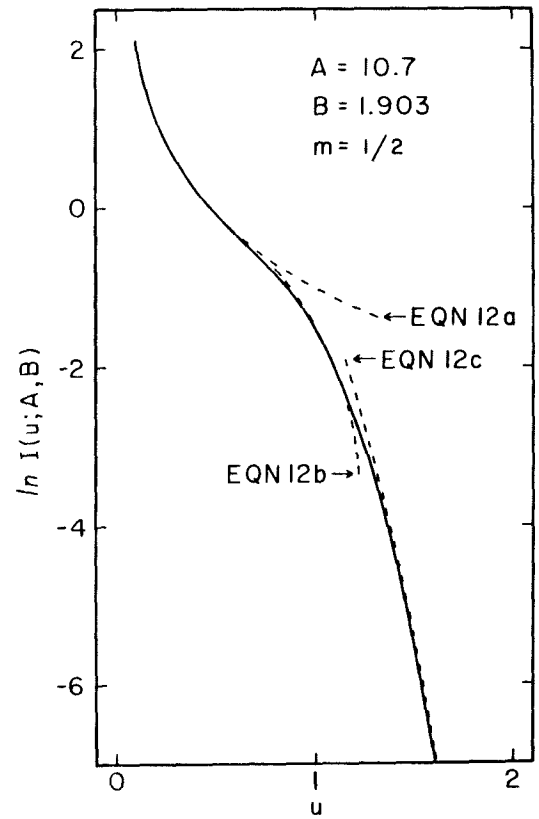

Figure 6. Graph of I(u;A,B) for parameters corresponding to As → SiO_2/Si with O recoils.

but it is relatively insignificant for $u>1$. A more pronounced exponential dependence was found using the approach by Kelly, et al. [2,3].

D. Comparison with Experiment

The range parameters S_{12}, g_{22}, g_{23}, h_{23}, and $\hat{h}_{23}$ were obtained from published range statistics, using a linear fit to the energy dependence [11,14]. Bulk densities were assumed for ρ. The primary recoil profiles given by Eqns. 10 and 11 for 26nm Ni/SiO_2, 33nm Cr/SiO_2 and 47nm Ti/SiO_2 samples, implanted with 290keV Xe to a fluence $\Phi = 10x10^{15}$ cm^{-2}, are presented in Figures 7a,b and c, respectively. The experimentally observed mixing profiles are also included. Calculations for both the $m = ½$ power law and universal cross-sections are shown. The agreement is adequate to warrant writing this chapter. The systematic variation in the shallow peak is readily apparent in relation to the calculated profiles. The extrapolated recoil yield was previously defined by linearly extrapolating the tail to the surface in a logarithmic plot. The area bound by the corresponding exponential curve was then calculated. The recoil yields for such a fit to the calculated power law profiles on the interval from 30 to 100nm are 0.67 for Ti, 0.77 for Cr, and 0.60 for Ni. The corresponding decay lengths are 37nm, 29nm, and 32nm, respectively. The measured extrapolated yield for Ni was 0.65, although this is surely 5% high due to Gaussian broadening. The observed decay length for Ni was 33nm and should not have been affected by this interference. The model seems to work in this case.

The model was also compared with computer simulations and experimental results for several other systems. Christel, et al., have published oxygen recoil profiles obtained from transport equation calculations for various ions implanted into SiO_2/Si [10]. Fig. 8 shows a series of oxygen profiles in a Si substrate calculated using Eqn. 8 with the universal cross-section for $1x10^{15}$ cm^{-2} As

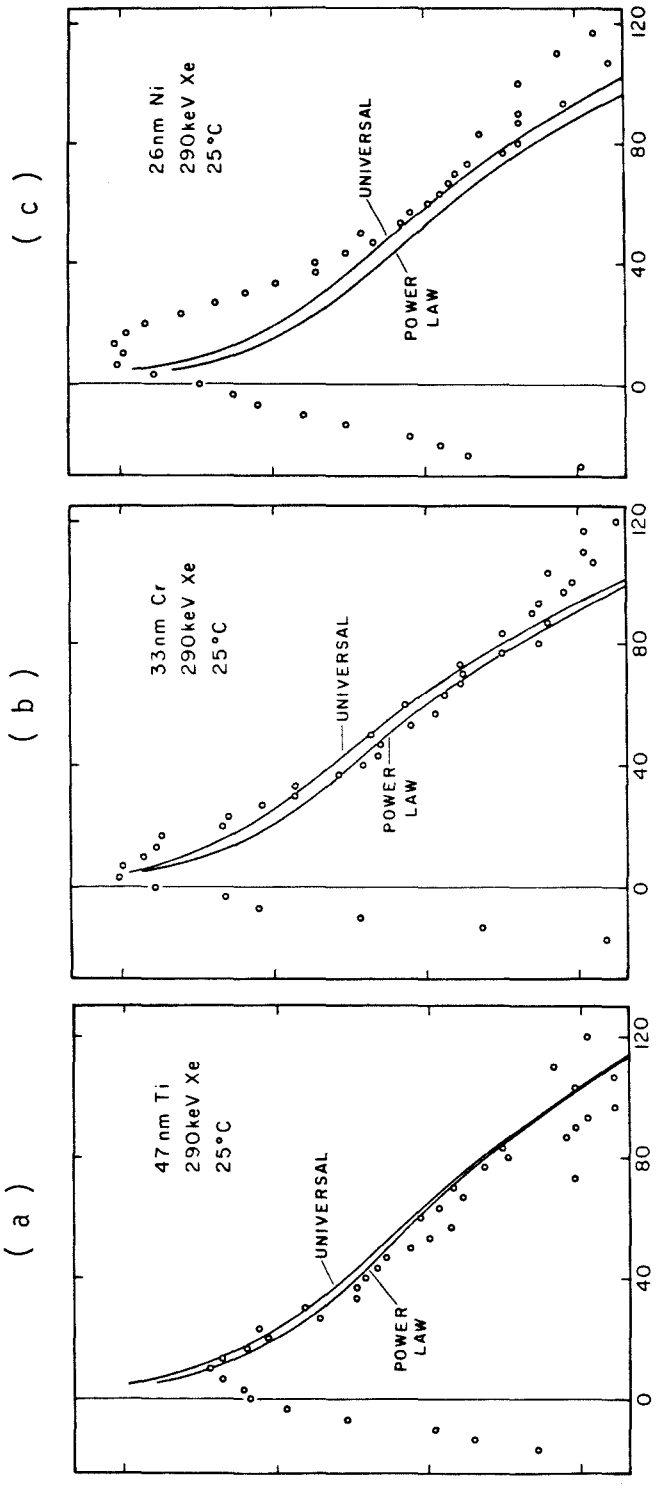

Figure 7. Comparison of theoretical primary recoil profiles and experimental results for 23μg cm^{-2} (a) Ti, (b) Cr and (c) Ni samples implanted with $10x10^{15}$ Xe cm^{-2}.

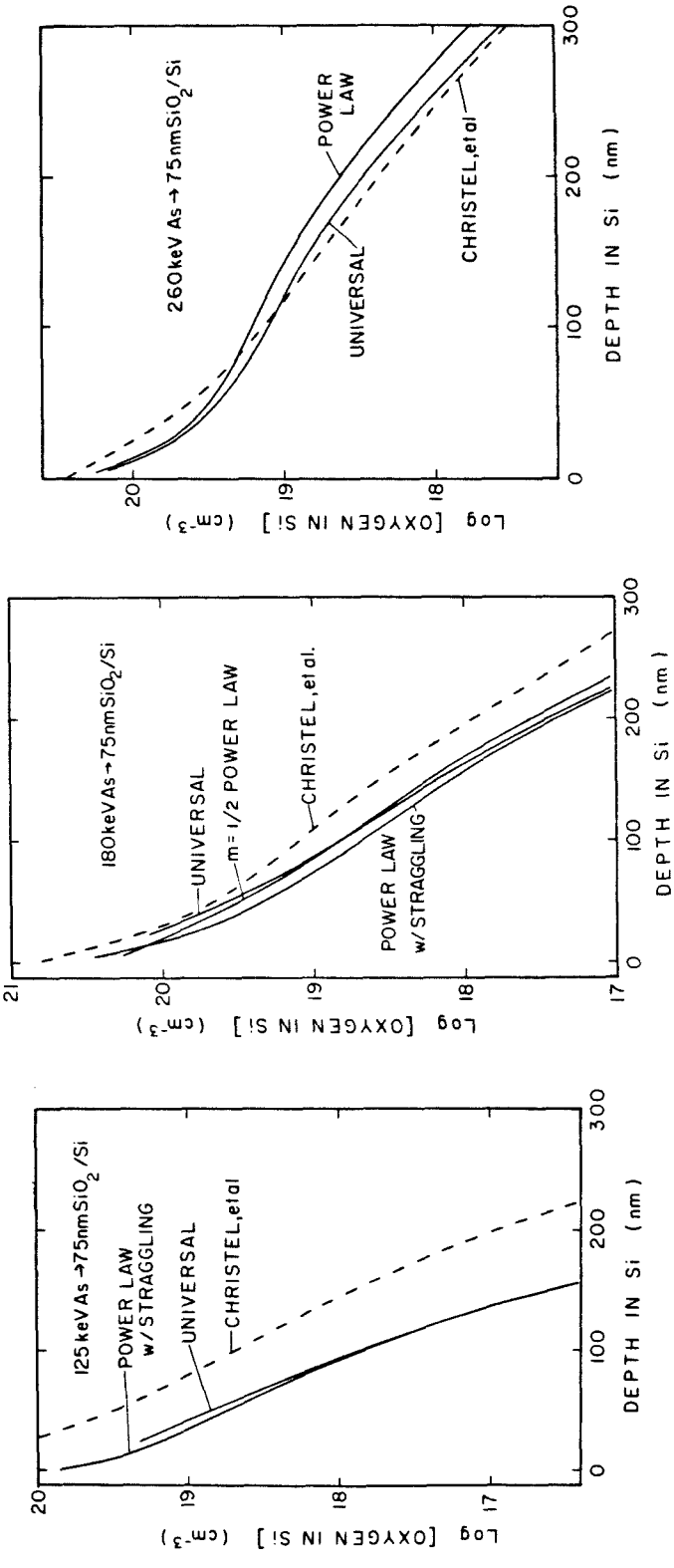

Figure 8. Comparison of simplified theory and transport equation results from Christel, et al.[10] for O recoils from As → SiO_2/Si.

implanted into 75nm SiO_2/Si at various energies. The results from the calculations of Christel, et al., are shown by dashed lines [10]. 125 keV As does not penetrate the 75nm SiO_2 layer; consequently, the integrand was set to zero for $E(z) < 0$ in order to perform the calculation in this case. There is reasonable agreement with the transport equation calculations for E_0 greater than 125 keV. Other results from Christel, et al., [10] show that the deviation between Eqn. 8 and the transport equation calculation for $r < 50$ nm is not just the result of omitting the secondary recoils but represents an actual failure of the model. A comparison of Eqn. 8 with a calculation by Christel, et al., [10] and experimental results by Hirao, et al., [15] are shown in Fig. 9 for oxygen recoils in Si produced by implanting 1×10^{15} cm^{-2} 180 keV As into 55nm SiO_2/Si. Both simulations appear to underestimate the recoil yield beyond 150nm. Another comparison is made in Fig. 10 with experimental results published by Moline and Cullis for 10×10^{15} cm^{-2} 150 keV As implanted into 43nm SiO_2/Si [16]. Besenbacher, et al., reported a recoil yield of 0.25 ± 0.6 for Cu atoms recoiling beyond 65nm of the interface for 500 keV implanted into 50nm Cu on Al [17]. A value of 0.18 is obtained from Eqn. 8 using the universal cross-section. The model represented by Eqn. 8 does pretty well with the depth dependence when it works. However, the magnitude is systematically low.

It is evident that the approximations leading to Eqn. 8 give a useful estimate of the recoil profile away from the interface when the source film thickness is no too great. It is interesting that the model fails severely when the incident ion does not penetrate the interface. Some of the assumptions can be tested by examining the distribution in the depth of origin of atoms recoiling to a specified depth. Let $P(z \mid r)\,dz$ be the probability that a recoil found at r originated from a region z, dz in the source layer. $P(z \mid r)$ was calculated with various values of r for the profiles reported in Figs. 7c and 9. The results given

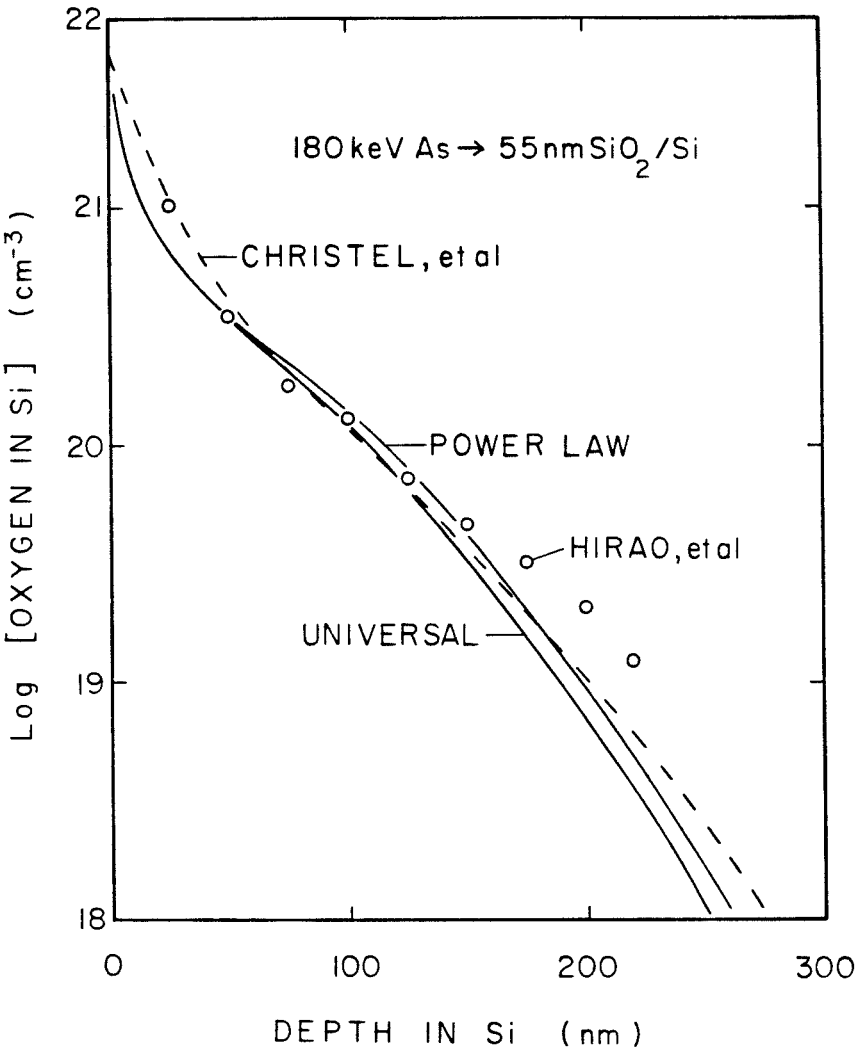

Figure 9. Comparison of simple theory with experimental results from Hirao, et al., [15] and transport equation results from Christel, et al.,[10].

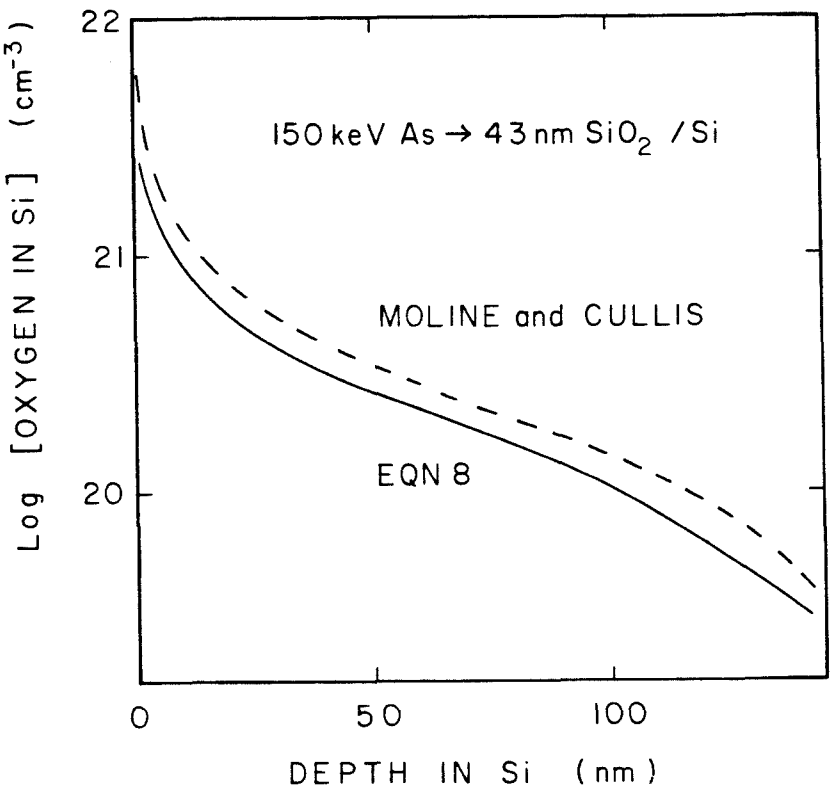

Figure 10. Comparison of simple theory with experimental results from Moline and Cullis [16].

in Fig. 11 show that the deep recoils come from throughout the source layer, whereas the shallow recoils are predicted to come only from near the interface. The latter case challenges the assumptions that deflections of the incident ion can be ignored and that Eqn. 7 gives an adequate representation of the relocation distribution. It is evident from Eqn. 9b that collisions with $\cos^2\theta < 1$ are most probable, although the energy transfer is less efficient. Incident ion straggling could conceivably enhance mixing near the interface; however, this was not found when it was included in the model. In fact, incident ion straggling did not significantly alter the recoil profile at all. This is indicated by one of the results plotted in Fig. 8b. This leaves the description of the relocation profile as the probable culprit. Secondary recoils contribute substantially to this region as well.

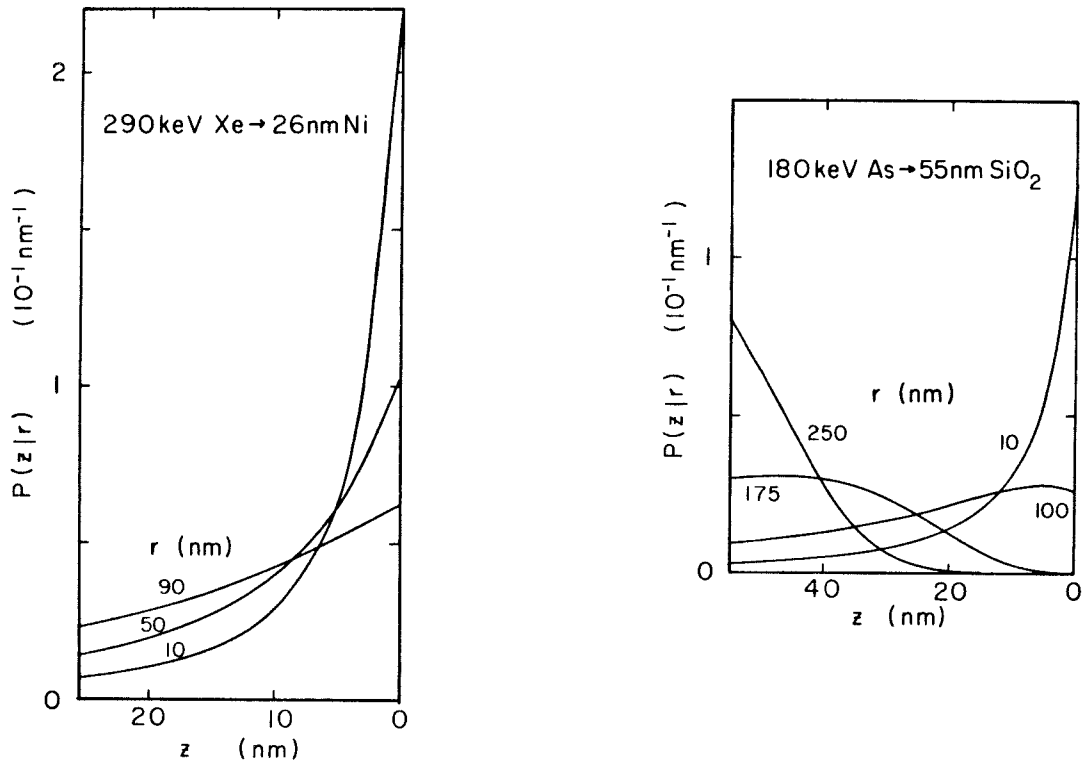

Figure 11. Distribution in depth of origin $P(z|r)$ for various relocation positions r with two types of samples.

References

[1] P. Sigmund and A. Gras-Marti, *Nucl. Instr. and Meth.* **182/183**, 25 (1981)

[2] R. Kelly and J. B. Sanders, *Surface Science* **57**, 143 (1976)

[3] S. Dzioba and R. Kelly, *J. of Nucl. Mat.* **76**, 175 (1978)

[4] R. Kelly and J. B. Sanders, *Nucl. Instr. and Meth.* **132**, 335 (1976)

[5] R. S. Nelson, *Radiat. Effects* **2**, 47 (1969)

[6] G. Falcone and A. Oliva, *Appl. Phys. Lett.* **42**, 41 (1983)

[7] G. Fischer, G. Carter and R. Webb, *Radiat. Effects* **38**, 41 (1978)

[8] R. Grötzschel, R. Klabes, U. Kreissing and A. Schmidt, *Radiat. Effects* **36**, 129 (1978)

[9] D. K. Brice, *J. Appl. Phys.* **46**, 3385 (1975)

[10] L. A. Christel, J. F. Gibbons and S. Mylroie, *Nucl. Instr. and Meth.* **182/183**, 187 (1981)

[11] K. B. Winterbon, *Ion Implantation Ranges and Energy Deposition Distributions* (IFI Plenum, New York, 1975)

[12] P. Sigmund, *Rev. Roum. Phys.* **17**, 823, 969, 1079 (1972)

[13] J. P. Biersack, *Nucl. Instr. and Meth.* **182/183**, 199 (1981)

[14] U. Littmark and J. F. Ziegler, *Handbook of Range Distributions for Energetic Ions in all Elements* (Pergamon, Elmsford, NY, 1983)

[15] T. Hirao, G. Fuse, K. Inoue, S. Takayanagi, Y. Yaegashi and S. Ichikawa, *J. Appl. Phys.* **50**, 5251 (1979)

[16] R. A. Moline and A. G. Cullis, *Appl. Phys. Lett.* **26**, 551 (1975)

[17] F. Besenbacher, J. Bottiger, S. K. Nielsen and H. J. Whitlow, *Appl. Phys.* **30**, 438 (1982)

Chapter VI Discussion and Concluding Remark

Summary of Results

The intermixing of Ti, Cr and Ni films with SiO_2 induced by Xe irradiation was described in Chapter III. There is no significant correlation between the reactivity of the metal with SiO_2 and the amount of mixing observed when the irradiations are performed at 25C or below. The contribution from primary recoils is quite pronounced since the gross mixing is small. A significant correlation exists between the mixing and the energy deposited through elastic collisions F_D. Several models were examined in Chapter IV in an attempt to describe the transport process in Ni/SiO_2. It is likely that injection of Ni by secondary recoil implantation is primarily responsible for getting Ni into the SiO_2. There were a few more objections against the other conceivable limiting cases. Secondary recoil injection is thought to scale with F_D. Trends in the mixing rates indicate that the dominant mechanism for Ti and Cr could be the same as for Ni. Nevertheless, the structure of the mixed region is very different for the three metals. The product of chemical reactions were identified with TEM and XPS. The low temperature results suggest that kinetic constraints are responsible for suppressing the chemical reactions that one might anticipate.

The processes of atomic transport and phase formation clearly fail to be separable at higher temperatures. A positive correlation with chemical reactivity emerges at higher irradiation temperatures. This was not pursued beyond the preliminary results reported in Appendix AIII.2 for Ti or Cr. The temperature at which rapid mixing occurs is not much below that for spontaneous

thermal reaction. Less Ni is retained in the SiO_2 at high irradiation temperatures. Ni incorporated in the SiO_2 by low temperature irradiation is not expelled during a consecutive high-temperature irradiation. The Ni remains trapped within larger clusters during a sequential 500C irradiation.

B. Comparison with Other Studies

Several ion irradiation-induced mixing studies with metal/insulator bilayer systems have been reported [1-4]. One difficulty with these experiments in general, including mine, is that high fluences must be employed to establish measurable intermixed regions if some form of resolution enhancement, with its additional uncertainty, is not used. The films can be altered during irradiation by sputtering and lateral segregation [2]. This can produce artificial steps in an RBS profile which are often hard to distinguish from real mixing at low temperatures. This is not a problem when intermixing produces regions with well-defined composition (steps in an RBS profile), such as may be the case in Nb/SiO_2 at room temperature [2], or Ni/SiC at high temperatures [3,4]. The step formation reported by White, et al., for 30nm Nb/SiO_2 with $10^{16}cm^{-2}$ 300keV Xe irradiation is in great contrast with our results. The difference may be associated with formation of a thermal spike in Nb but not in Ni. The energy deposition in Ni may not be sufficient to produce a dense cascade. Many smaller sub-cascades would quench faster than a single dense cascade. The range of motion within a sub-cascade would also be restricted.

A natural direction for further work is to extend the analysis developed for the early transition metals to include Nb. Boiling HCl with 1 w/o tetra-sodium EDTA was found to etch Nb. This etch has not been characterized, and only preliminary experiments have been conducted. Another perspective can be gained from repeating some of the experiments in which chemical effects have been

observed, but using light ions instead [5]. These experiments are underway at Caltech [6].

As a final parting remark, hindsight reveals that this research would have been more productive and rewarding if collaboration with others in this field had been actively pursued...

References

[1] T. Banwell, B-X. Liu, I. Golecki and M-A. Nicolet, *Nucl. Instr. and Meth.* **209/210**, 125 (1983)

[2] C. W. White, G. C. Farlow, J. Narayan, G. J. Clark and J. E. E. Baglin, *Materials Lett.* **2**, 367 (1984)

[3] D. Fathy, O. W. Holland, J. Narayan and B. R. Appleton, *Nucl. Instr. and Meth.* **B7/8**, 571 (1985)

[4] B. R. Appleton in *Proceedings of the Second Workshop on Ion Mixing and Surface Layer Alloying*, D. M. Foolstaed, R. S. Averback and M-A. Nicolet, eds. (Sandia National Laboratory, NM, 1986), 99

[5] W. L. Johnson, Y. T. Cheng, M. van Rossum and M-A. Nicolet, *Nucl. Instr. and Meth.* **B7/8**, 657 (1985)

[6] Y. T. Cheng, private communication (1986)

Appendix AII.1 Beam Heating

Fig. A1a shows a schematic representation of a Si substrate mounted to a carousel with a 100μm film of heat paste. The amount of Joule heating produced by a 3μA cm^{-2} 300keV beam is $w_0 = 0.9$W cm^{-2}. This produces a steady-state temperature difference across the Si (thermal conductivity α = 1.49W/cm°C) and heat paste (α = 7.5x10^{-3} W/cm°C) of 0.1 and 1.2C, respectively. Since the sample thickness is small compared to the dimensions of the irradiated area, the heating of the carousel can be treated separately. Fig. A1b shows a model used to estimate the temperature rise of the carousel; a radially symmetric heat source $f(r)$ is assumed. The temperature $T(r,z,t)$ satisfies $\nabla^2 T = (m/\alpha)\frac{\partial T}{\partial t}$ where m is the specific heat capacity. Mixed boundary conditions apply with $\left.\frac{\partial T}{\partial z}\right|_{z=0} = -f(r)/\alpha$ and $T \to 0$ as r, $z \to \infty$. The initial condition is $T = 0$. This PDE can be solved using standard transform techniques [1] giving

$$T(r,z,t) = \int_0^t \int_0^\infty \frac{F_0(k)}{\sqrt{\pi m \alpha \tau}} e^{-k^2\frac{\alpha\tau}{m} - \frac{mz^2}{4\alpha\tau}} J_0(kr)\, k\, dk\, d\tau \qquad (1)$$

where $F_0(k) = \int_0^\infty f(r) J_0(kr)\, r\, dr$

J_0 is the Bessel function of order zero. The temperature rise for $f(r)$ = constant w_0 on $0 \le r \le a$ and vanishing elsewhere approaches steady-state like $1 - O\left[\frac{\tau}{t}\right]^{1/2}$ where $\tau = \frac{ma^2}{4\alpha}$. For $t \gg \tau$, the steady- state temperature along the z axis is

$$T(0,z) = \frac{w_0 a}{\alpha}\left[\left(1+\frac{z^2}{a^2}\right)^{\frac{1}{2}} - \frac{z}{a}\right] \tag{2}$$

while for either z or $r \gg a$,

$$T(r,z) \sim \frac{w_0 a}{\alpha}\frac{1}{2}\frac{a}{\sqrt{r^2+z^2}} \tag{3}$$

as expected for radial heat flow. A stainless steel holder (α = 0.17W/cm°C, m = 4J/cm^3°C) with a = 1cm reaches steady-state in $10\tau \sim 1$ minute with a maximum temperature rise $w_0 a/\alpha$ = 16C. The temperature at points within our finite carousel will be closer to the surface temperature than the model (Eqn. 3) predicts. The estimated temperature rise for our thermocouple 3cm from the surface would be ~3C, which is comparable with the observed fluctuations of ~2C.

Reference for Appendix AII.1

[1] G. F. Carrier, M. Krook and C. E. Pearson, *Functions of a Complex Variable* (McGraw-Hill, New York, 1966), 301.

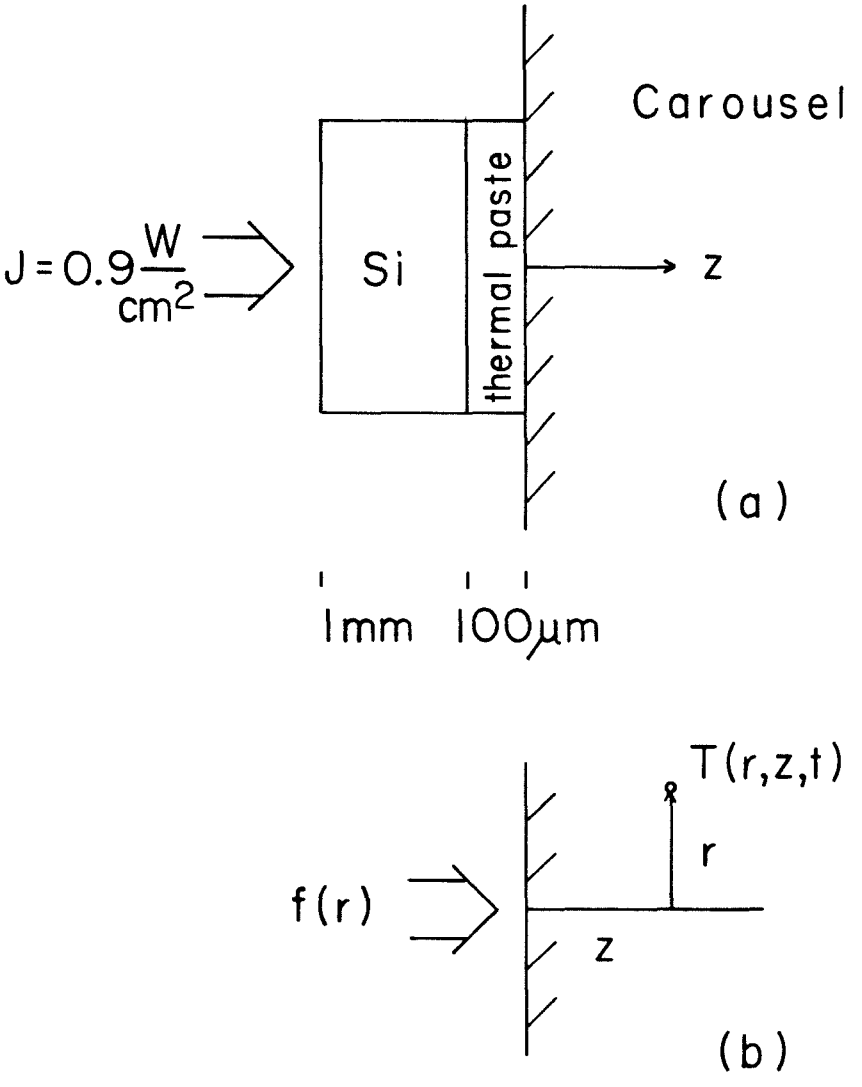

Figure A1. Schematic representation of a sample mounted on carousel.

Appendix AII.2 Pulse Pile-Up

Fig. A2a shows a block diagram of the signal processing and pulse pile-up detection system used for RBS. A current spike generated when a He particle stops in the detector is integrated in the pre-amp to give a voltage step. This is differentiated and shaped to give the indicated pulse by the subsequent amplifier. The pulse discriminator identifies individual pulses by looking at their rising and falling slopes. A second pulse arriving before time $\tau \simeq$ 400nSec, in which a previous pulse has not decayed sufficiently for the lower threshold to be crossed, will not be recognized. Two resolvable pulses occuring within ~6μSec are rejected. An RBS spectra for a 100nm Pt film on Si is shown in Fig. b. The step a 1.00 MeV corresponds to the Si substrate, while the rectangular peak from 1.71 - 1.84 MeV is for scattering off Pt. Si is displaced from its surface position of 1.13 MeV by the He energy loss in the Pt film. The peak at 3.6 MeV is Pt-Pt pile-up, and the ledge out to 2.8 MeV is due to Pt-Si pile-up. The two pulse pile-up spectrum is well known [1]. Let $f(E)dE$ be the probability that an incident He will be backscattered and detected with energy E,dE. $f(E)$ is determined by the sample. Since scattering represents identically distributed independent events, the arrival of He at the detector within dE constitutes a Poisson process [2] with rate $\dot{Q}f(E)dE$, where $\dot{Q}$ is the incident particle rate upon the sample. The probability of exactly n events in an interval ΔE occurring within a fixed time t is $P(n) = \frac{(\lambda t)^n}{n!} e^{-\lambda t}$ where $\lambda = \dot{Q}\int_{\Delta E} f(E)dE$. Suppose a particle with energy E_1 is detected at $t = 0$. The probability that exactly one event with energy E_2,dE occurs in the interval $[-\tau,\tau]$ is

$$P(E_1+E_2|E_1) = \frac{f(E_2)dE}{\int f dE}(2\tau\dot{Q}\int f dE)\exp(-2\tau\dot{Q}\int f dE) \qquad (1)$$

This is the probability that a He with energy E_1 will actually contribute to the pile-up spectrum at E_1+E_2. The distribution of the average number of counts in the two pulse pile-up spectrum is

$$h_p(E) = \frac{2\tau}{T}e^{-\frac{2\tau}{T}N}\int h(E')\cdot h(E-E')dE' \qquad (2)$$

where $h(E) = \dot{Q}Tf(E)$ represents the distribution of counts in time T if we neglect the fraction lost to pile-up. $N = T\dot{Q}\int f(E)dE$ is the (average) number of counts in the entire true spectrum. Typically $\frac{2\tau}{T}N \ll 1$, so that for a fixed N, $h_p(E)$ should vary linearly with $1/T$. Fig. A2c shows a plot of the integral pulse pile-up yields for the Pt-Pt peak and for the tail above 1.84 MeV, versus $1/T$. Using Eqn. 2, the parameter τ was calculated to be 350, 500 nSec, respectively. This is in good agreement with the value estimated from analysis of the circuit. The usual way to circumvent this inherent speed limitation is to use a separate high speed discriminator in conjunction with that in the 572.

References

[1] L. Wielopolski, *J. Appl. Phys.* **49**, 4943 (1978)

[2] N. G. van Kampen, *Stochastic Processes in Physics and Chemistry* (North-Holland, Amsterdam, 1983), 141.

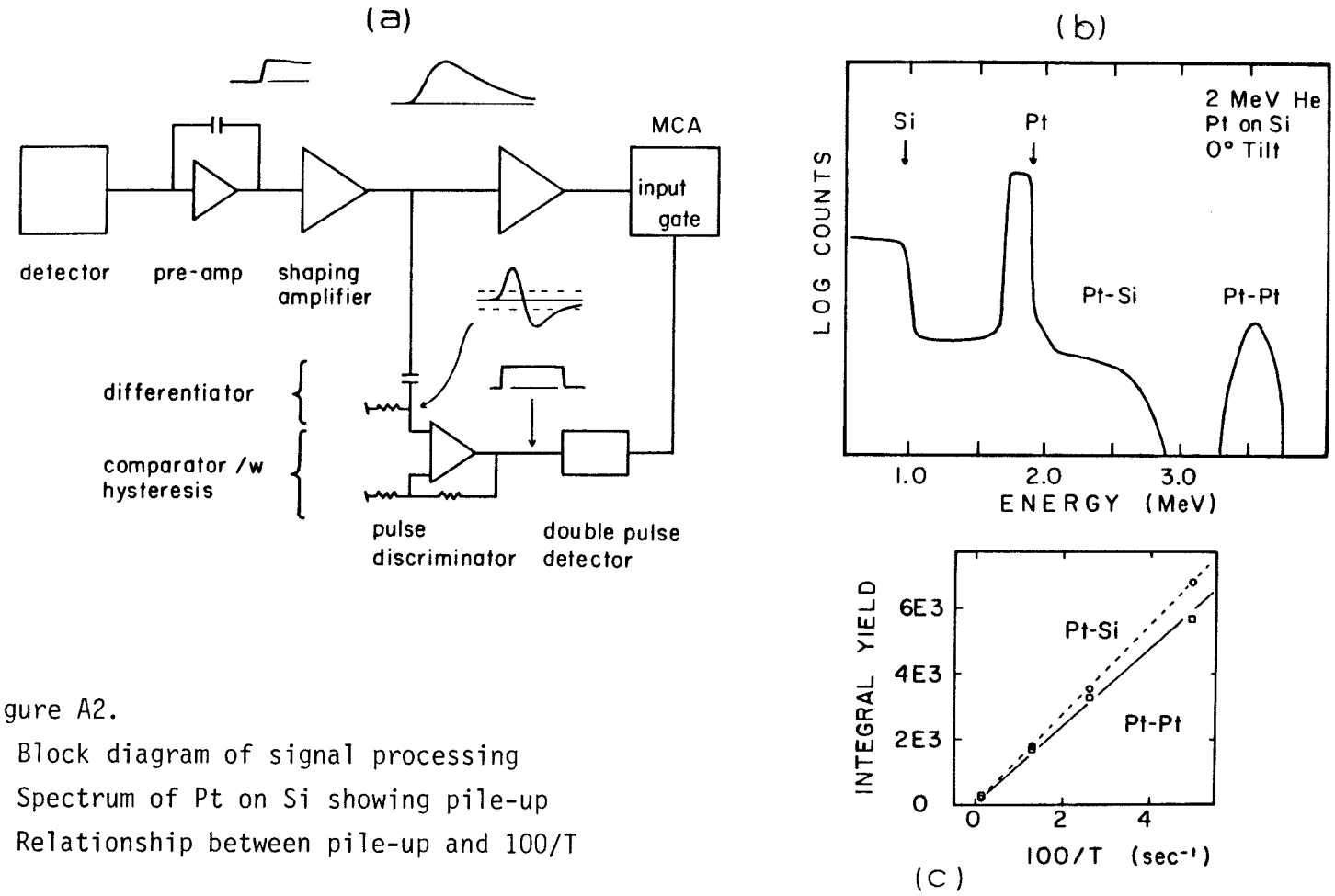

Figure A2.

a) Block diagram of signal processing

b) Spectrum of Pt on Si showing pile-up

c) Relationship between pile-up and 100/T

Appendix A III.1 Gaussian Broadening

The profiles obtained by RBS represent the actual atomic profiles $f(x)$ convoluted with the nearly Gaussian spectrometer noise density. The observed profiles $F(x)$ can be described by

$$F(x) = \int_{-\infty}^{\infty} f(\xi)\, g(x-\xi)\, d\xi \tag{1}$$

where $g(x) = \frac{1}{\sqrt{2\pi}\sigma} e^{-\frac{x^2}{2\sigma^2}}$

The variance of the noise is given by σ^2. This appendix discusses how Eqn. 1 alters some of the profiles which were encountered in our studies of ion mixing. These well known results are not at all profound, but are presented here as a reminder. Two useful relations follow from a simple change in the order of integration;

$$\int_{-\infty}^{\infty} F(x)\, dx = \int_{-\infty}^{\infty} f(\xi)\, d\xi \tag{2a}$$

and

$$\int_{-\infty}^{\infty} x\, F(x)\, dx = \int_{-\infty}^{\infty} \xi\, f(\xi)\, d\xi \tag{2b}$$

In their practical application, the integrals need only extend over the interval for which the profile is significantly different from zero.

The rectangular profile $h(x) = \begin{cases} 1 & \text{if } |x| < w \\ 0 & otherwise \end{cases}$ can be used to describe the

shallow peak. The convoluted profile $H(x)$ is also symmetric and can be characterized by its height H_{max} and its half width at half maximum W. The peak height of $H(x)$ occurs at $x = 0$ and is $H_{max} = \mathrm{erf}(\frac{w}{\sqrt{2}\sigma})$. The apparent width W given by the condition $H(W) = \frac{1}{2}H(0)$ satisfies

$$\mathrm{erf}(\frac{W+w}{\sqrt{2}\sigma}) = \mathrm{erf}(\frac{w}{\sqrt{2}\sigma}) + \mathrm{erf}(\frac{W-w}{\sqrt{2}\sigma})$$

The solution of this equation is shown in Fig. A1, along with the behavior for the peak height H_{max}. It can be seen that $\frac{W}{\sigma} = \sqrt{2\ln 2} + O(\frac{w}{\sigma})^2$ for $w < \sigma$ while the asymptotic behavior for $w \gg \sigma$ is $\frac{W}{\sigma} \sim \frac{w}{\sigma} + (\frac{w}{\sigma})^{-1} e^{-\frac{1}{2}(\frac{w}{\sigma})^2}$.

The exponential profile $f(x) = \begin{cases} e^{-\beta x} & \text{if } x \geq 0 \\ 0 & \text{if } x < 0 \end{cases}$ produces a profile which is also exponential for large x. Completing the square in the exponent in the integral gives

$$F(x) = e^{-\beta x} \cdot e^{\frac{1}{2}\beta^2\sigma^2} \cdot \frac{1}{2}\left[1 + \mathrm{erf}(\frac{x-\beta\sigma^2}{\sqrt{2}\sigma}) \right] \qquad (3)$$

The third term approaches 1 for $x > \sim \beta\sigma^2 + \sqrt{2}\sigma$, which for our recoil tails is 16nm, leaving only the distortion from the second exponential term. This second term is just a constant which will displace the profile in a log plot.

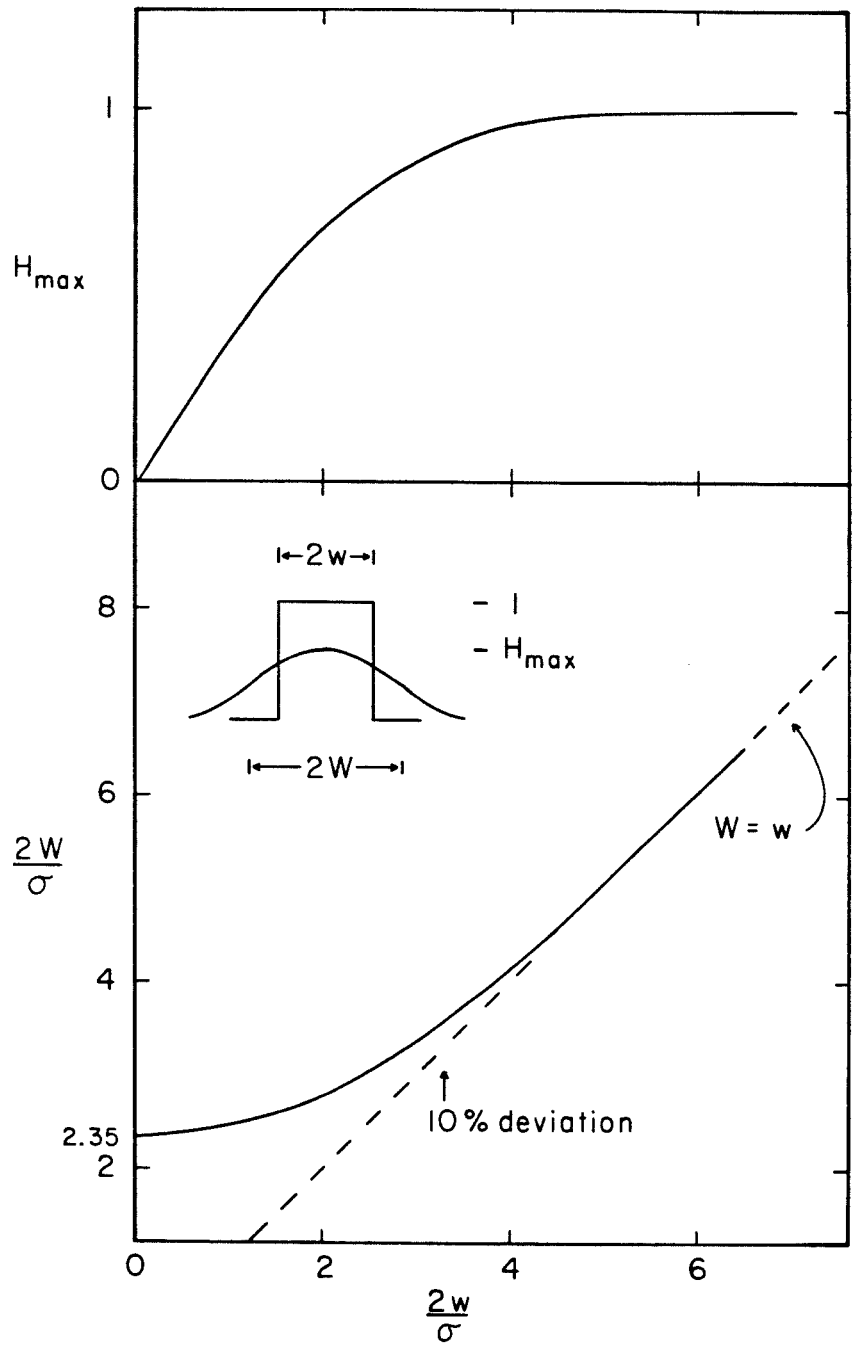

Figure A1. Graphs of apparent peak height and width at half maximum for a rectangular profile broadened by convolution with a Gaussian.

Appendix AIII.2 Chemical Effects in Ion Mixing of Transition Metals on SiO_2

Pre-print from *Nuclear Instruments and Methods*.

Nuclear Instruments and Methods 209/210 (1983) 125–129
North-Holland Publishing Company

CHEMICAL EFFECTS IN ION MIXING OF TRANSITION METALS ON SiO_2

T. BANWELL, B.X. LIU *, I. GOLECKI ** and M.-A. NICOLET
California Institute of Technology, Pasadena, California 91125, USA

The mixing of thin evaporated films of Ti, Cr and Ni of various thicknesses on thick (= 650 nm) thermally grown SiO_2 layers on ⟨111⟩ Si wafers has been investigated for 290 KeV Xe irradiations over the range of Xe fluence, Φ, of 10^{15} to 2×10^{16} Xe/cm^2 and of irradiation temperature, T, of 77 to about 750 K. For the analysis of the irradiated samples, mainly backscattering spectrometry was used after the free metal had been removed by chemical etching. The amount of mixed metal contained in the SiO_2 increases as Φ^{β}, where $\beta = 0.56$, to 0.73, at room temperature and below, for all metals and thicknesses, suggesting that cascade mixing dominates the transport process in this temperature region. The contribution of recoil mixing at the deep tail of the metal profiles is probable and may account for the values of $\beta > 1/2$. At 750 K, enhanced mixing occurs for the thermally reactive systems Ti/SiO_2 and Cr/SiO_2; however, mixing is suppressed for Ni/SiO_2. The fact that the deep tail of the metal profiles is not altered suggests that only the cascade mixing process is affected by chemical driving forces.

1. Introduction

Energetic ion irradiation results in relocation of atoms in a region around the incident ion track, in addition to the introduction of the ion into the surface. Studies of ion-beam induced mixing of several bilayer systems indicate that the mixing process is quite complex. A parabolic ion dose dependence is observed in silicide formation with a thin Fe, Co, Ni, Pd, Hf or Pt layer on Si induced by room temperature Xe ion irradiation [1]. A comparison of the respective thermal and ion-beam induced reactions suggests that the ion-beam mixing is dominated by chemical driving forces [1]. Ion beam irradiation of Sb/Si [2] and SiO_2/Si [3] bilayers results in interfacial mixing with a linear dependence on incident ion dose, as predicted for recoil implantation [2–5]. A parabolic dose dependence is associated with cascade mixing [5,6].

In the present study we have investigated the ion-beam mixing of Ti/SiO_2, Cr/SiO_2 and Ni/SiO_2 bilayers with 290 keV Xe. These systems were chosen in order to isolate the role of chemistry in the ion-beam mixing process. The metals have similar atomic masses such that differences in the ballistic processes will be minimal; however, their chemical reactivities with SiO_2 are significantly different [7]. All reactions of Ti with SiO_2 are thermodynamically favorable. In addition, Ti provides a diffusion path allowing oxygen transport away from the reaction zone at elevated temperatures [8]. There are two favorable reactions of Cr with SiO_2, both forming Cr_2O_3 which is renowned for its passivation behavior. There are no thermodynamically favorable reactions of Ni with SiO_2, and Ni films tend to coalesce into balls at high temperatures [7].

2. Experimental

Substrates with a ~ 6500 Å SiO_2 layer were prepared by 1100°C steam oxidation of polished ⟨111⟩ Si wafers. A Ti, Cr or Ni layer was deposited on the SiO_3 by e-beam evaporation in an oil-free vacuum system at pressures of $< 10^{-7}$ Torr. Samples with metal thickness $R_p/2$, $R_p - \Delta R_p$ and R_p were prepared with each metal, where R_p is the projected range and ΔR_p is the standard deviation in the projected range of 290 KeV Xe^+ in the metal (33 ± 2 μg/cm^2, 13 ± 2 μg/cm^2, respectively) [9]. Samples studied for thermal reactivity were isothermally annealed face-to-face in a quartz tube vacuum furnace at pressures of $< 10^{-6}$ Torr, over the temperature range 500–810°C for periods of 10–180 min. Xenon implantations were

* Permanent address: Qinghua University, Beijing, The People's Republic of China.
** Permanent address: Rockwell International, Microelectronics Research and Development Center, Anaheim, California 92803, USA.

0167-5087/83/0000–0000/$03.00

made at sample temperatures of −196°C, 27°C and 480–500°C with 290 keV Xe^+ to a fluence Φ_{Xe} of 10^{15}–2×10^{16} cm^{-2}. The target chamber pressure was $\lesssim 10^{-6}$ Torr. Titanium samples for high temperature Xe irradiation were capped with ~ 100Å of evaporated Al to inhibit thermal oxidation. The samples were subsequently examined by 2.0 MeV $^4He^+$ ion backscattering spectrometry. The free metal was removed by etching in boiling (85°C) 12 M HCl for 10 min. The samples were then dipped in hot (85°C) concentrated H_2SO_4 and rinsed in double distilled H_2O, followed by blow drying with N_2. The depth profiles of residual metal and Xe after etching were determined by 2.0 MeV $^4He^+$ backscattering analysis using an incidence angle of 60° from the sample normal and a scattering angle of 170°. The sensitivity in these experiments is 10^{14} cm^{-2} for Ti, Cr and Ni and 2×10^{13} cm^{-2} for Xe.

Selected samples were examined before and after etching by scanning electron microscopy/energy dispersive X-ray analysis (SEM/EDAX).

The residual metal remaining after etching unimplanted and unannnealed samples was below the 10^{14} atom/cm^2 sensitivity of our backscatter analysis. There is no evidence that the etching process removes metal or Si from layers containing Si. The presence of an oxygen-deficient metal oxide will inhibit the etching of Cr, although Ti etching is unaffected.

3. Experimental results

Our thermal annealing results agree with those of previous works [7]. Reaction products for Ni after 810°C and Ti, Cr after 500°C annealing for 120 min could not be detected. Both Ti and Cr react rapidly with SiO_2 at ≥ 670°C, attaining steady state in < 10 min with the thickest films used (730 Å, 470 Å, respectively).

A typical backscatter spectrum of a Xe irradiated sample (730 Å Ti, 6.7×10^{15} Xe/cm^2) is shown in fig. 1. Limited energy resolution and sputtering effects prevent simple analysis of the interface by backscattering spectometry before etching. The metal profile in the SiO_2 is readily discernible after removal of the free metal layer. The areal density or sheet concentration $[Ti]_s$ of the residual Ti is not altered by subsequent prolonged etching treatments. This was also verified for Cr and Ni. The

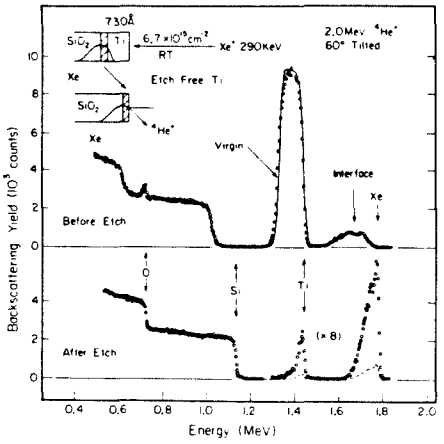

Fig. 1. Backscatter spectrum taken before and after etching a 730 Å-Ti layer on SiO_2 irradiated at RT with 6.7×10^{15} cm^{-2} 290 keV Xe.

Xe distribution in the SiO_2 is also preserved after etching. From the absence of a Xe marker shift, less that 40 Å of SiO_2 is etched from clean SiO_2 substrates which are implanted with 10^{15}–10^{16} cm^{-2} 290 keV Xe.

Fig. 2 shows log-log plots of the areal density of metal $[M]_s$ in the SiO_2 versus Xe fluence for Ti, Cr and Ni samples with various metal layer thicknesses after room temperature irradiation with 290 keV Xe and etching. To first order, the quantity log $[M]_s$ exhibits a predominately linear dependence on log Φ_{Xe} over the fluence range studied, with $d \log [M]_s / d \log \Phi_{Xe} = 0.56$–$0.73$. A slight systematic departure from linearity is evident. The mixing behavior is relatively insensitive to metal layer thickness.

The Ti and Xe profiles in SiO_2 for samples with an initial 470 Å Ti layer irradiated at room temperature with 290 keV Xe are shown in fig. 3 for various Xe fluences Φ_{Xe}. Similar profiles are obtained with the other Ti, Cr and Ni samples. The Ti profiles in fig. 3 are well represented by exponential tails; $[Ti](x) \propto \Phi_{Xe}^{0.63} \exp(-x/L)$, where x is the normal distance from the Ti/SiO_2 interface and $L \simeq 200$–300 Å.

Fig. 4 reports the influence of substrate temperature during irradiation on the Xe ion beam induced mixing of Ti, Cr and Ni with SiO_2. Within

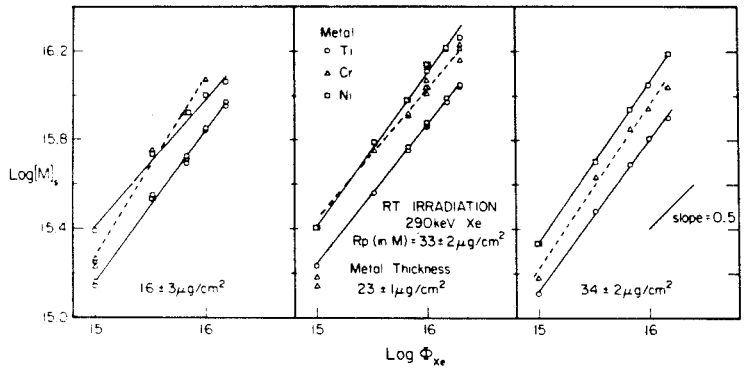

Fig. 2. Plots of $\log[M]_s$ versus $\log \Phi_{Xe}$ with 290 keV RT Xe irradiation for selected Ti, Cr, and Ni film thickness on SiO_2.

experimental uncertainty, the mixing behavior at RT and 77 K are the same. Enhanced mixing is observed for both Ti and Cr at 750 K (470°C) while the elevated substrate temperature results in suppressed mixing with Ni. Thermally induced reaction is not observed for $\Phi_{Xe} = 0$.

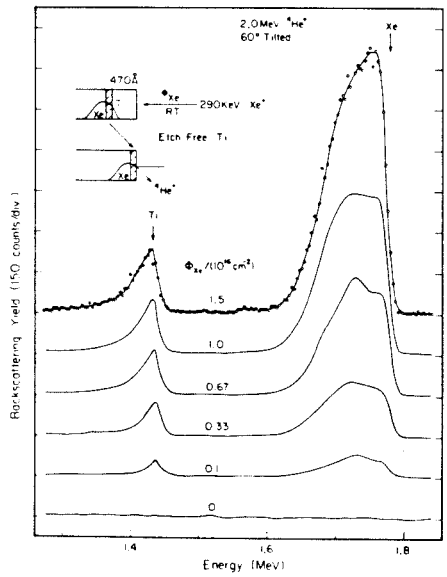

Fig. 3. Depth profile of intermixed Ti and residual Xe after RT irradiation with 290 keV Xe.

Fig. 5 shows the Ti and Ni profiles in SiO_2 for the corresponding samples irradiated at room temperature and 750 K with 10^{16} cm^{-2} Xe. Only the interfacial region is modified by the high-temperature Xe irradiation. The deeper portions of the metal profiles are unaltered. Near the interface, the Ti density is enhanced and the Ni density reduced at 470°C with respect to their room temperature levels.

4. Discussion

At room temperature and below, the mixing of Ti, Cr, and Ni layers with SiO_2 by Xe irradiation displays a fractional power-law dependence on Xe fluence, $[M]_s \propto \Phi_{Xe}^{\beta}$, where $\beta \sim 0.56$–0.73, suggesting that cascade mixing dominates the transport process in this temperature region. The exponential tail in the metal profiles indicate that recoil implantation is also significant [4,5]. The metal penetration depths are consistant with the maximum projected range of primary recoils in SiO_2; $R_p(\gamma_{M,Xe}E_0) \sim 1500$ Å, where $\gamma_{M,Xe}$ is the maximum fractional energy transfer to metal recoils and E_0 is the incident Xe ion energy. A combination of both processes can produce an apparent $\beta = d \log [M]_s / d \log \Phi_{Xe}$ which is greater than the value $\beta = 1/2$ predicted for isotropic low energy cascade mixing [5,6]. Also, a $\beta = 2/3$ dependence has been suggested for high-energy

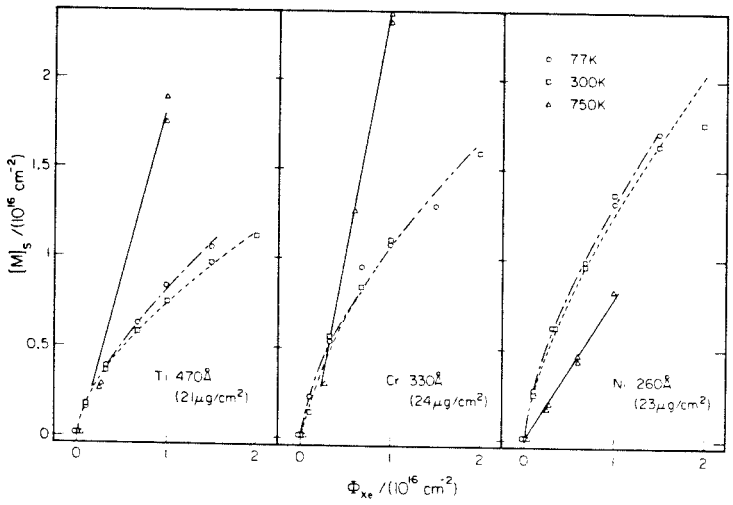

Fig. 4. Plots of $[M]_s$ versus Φ_{Xe} with 290 keV Xe irradiation of 23 ± 1 μg/cm² Ti, Cr, and Ni layers on SiO_2 for different substrate temperatures during irradiation.

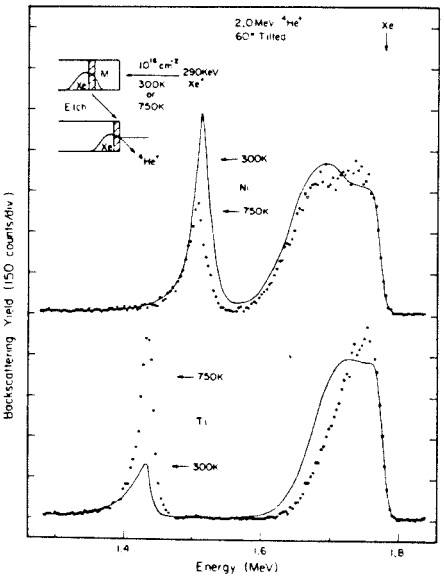

Fig. 5. Backscatter spectra showing comparison of intermixed Ti, Ni in SiO_2, and residual Xe after RT and 470°C irradiation with 10^{16} cm^{-2} 290 keV Xe.

cascade mixing [5]. Chemical effects are not expected at room temperature due to the relatively large activation energy of the chemical reactions involved.

A direct correlation exists between the high-temperature ion-mixing results and the corresponding thermally induced reactions. Fig. 4 shows that enhanced mixing occurs for the thermally reactive systems Ti/SiO_2 and Cr/SiO_2; however, ion-induced mixing is suppressed for Ni, which minimizes its interaction with SiO_2 [7]. The ratio $[Ti]_s/[Cr]_s$ is nearly constant, independent of Xe fluence or substrate temperature during ion irradiation. Transport limitations present in the thermal annealing of Cr/SiO_2 are not evident in our ion-beam mixing results. Temperature-related changes in the metal distributions after Xe irradiation are confined only to the vicinity of the interface: the extended tail is not affected by substrate temperature. This suggest that only the cascade mixing process is affected by chemical driving forces. From these observations, we propose that local thermodynamic considerations of the final state after atomic redistribution in a single collision cascade influence net transport in irradiation induced mixing. The energy transfer in last genera-

tion recoils of a collision cascade may be commensurate with chemical potentials.

5. Conclusion

One possible role of chemical driving forces in the outcome of ion beam mixing has beeen isolated in the current experiments. Our etching analysis with the early transition metal–SiO_2 bilayer system promises to provide further insight into the role of chemistry in ion beam mixing.

The authors wish to acknowledge R. Fernandez (Caltech) for performing the metal evaporations, R. Gorris (Caltech) for the design and construction of the high-temperature carrousel used in the high-temperature Xe irradiations, and R.E. Johnson (Rockwell International) for the SEM/EDAX work. The interest and encouragement of Drs. T.M. Reith and R.E. Davis (IBM, Tucson) is also acknowledged.

References

[1] J.W. Mayer, B.Y. Tsaur, S.S. Lau and L.S. Hung, Nucl. Instr. and Meth. 182/183 (1981) 1.
[2] M. Bruel, M. Floccari and J.P. Gailliard, Nucl. Instr. and Meth. 182/183 (1981) 93.
[3] B. Villepelet, F. Ferrieu, A. Grouillet, A. Golanski, J.P. Gailliard and E. Ligeon, Nucl. Instr. and Meth. 182/183 (1981) 137.
[4] L.A. Christel, J.F. Gibbons and S. Mylroie, Nucl. Instr. and Meth. 182/183 (1981) 187.
[5] P. Sigmund and A. Gras-Marti, Nucl. Instr. and Met. 182/183 (1981) 25.
[6] S. Matteson and M-A. Nicolet, in: Metastable materials formation by ion implantation, eds., S.T. Picraux and W.J. Choyke (Materials Research Society, 1981) Vol. 7, p. 3.
[7] R. Pretorius, J.M. Harris and M-A. Nicolet, Sol. St. Elect. 21 (1978) 667.
[8] K. Hauffe, Oxidation of metals (Plenum Press, New York, 1965) pp. 209–218.
[9] G. Dearnaley, J.H. Freeman, R.S. Nelson and J. Stephen, Ion implantation (North-Holland, Amsterdam, 1973).

Appendix AIII.3 Ion Irradiation Effects in $CrSi_2$ Thin Films

This paper will appear in May 1986 issue of the *Journal of Applied Physics*.

Effects of ion irradiation on conductivity of $CrSi_2$ thin films

T. C. Banwell, X.-A. Zhao,[a] and M-A. Nicolet
California Institute of Technology, Pasadena, California 91125

(Received 21 October 1985; accepted for publication 14 January 1986)

Electrical resistivity measurements are used to study damage in $CrSi_2$ thin films induced by Ne, Ar, or Xe ion irradiation over a fluence range of 10^{10}–10^{15} ions cm^{-2}. Irradiation produces a factor of 5–12 increase in film conductivity at the higher fluences. The influence of defect generation and recombination is evident. We speculate that formation of a compound defect is a dominant factor enhancing film conductivity. A temperature dependence at low fluences is reported and tentatively identified.

I. INTRODUCTION

The use of metal silicides in contact and interconnect technologies has motivated investigation of irradiation damage in silicides.[1-3] Recent studies show that the electrical conductivity of $CoSi_2$, $NiSi_2$, and Pd_2Si films are lowered by ion irradiation,[1,2] presumably due to the reduction in carrier mobility. In contrast, the conductivity of $CrSi_2$ can be increased by ion irradiation.[2,3] The details of the responsible processes are unknown. $CrSi_2$ is particularly interesting since it is a narrow (0.27 eV) band-gap semiconductor.[4,5] Thermally grown $CrSi_2$ films typically show degenerate p-type conductivity with carrier densities exceeding 10^{20} cm^{-3}. Electron and hole mobilities are 0.15 and 15 cm^2/V s, respectively.[4]

We report here on our investigations of changes in electrical transport in $CrSi_2$ films associated with Xe, Ar, and Ne ion irradiation. Two models are proposed which offer some insight into the damage process.

II. EXPERIMENT

$CrSi_2$ films were produced on several types of substrates. Approximately 1-μm-thick SiO_2 layers were thermally grown on 0.01 Ω cm n-type $<111>$ Si wafers by wet oxidation. Following oxidation, 80-nm Si, 40-nm Cr, and 40-nm Si layers were sequentially deposited thereon by e-beam evaporation; the background pressure remained below 10^{-7} Torr. Also, 30–50 Ω cm n-type $<100>$ Si and 5–30 Ω cm p-type $<111>$ Si wafers were organically cleaned, etched in 10% HF, slightly oxidized in boiling [H_2O_2, NH_3 (aq), H_2O: 1,1,5] and finally dipped in 3% HF prior to loading for deposition. Consecutive depositions of 40-nm Cr and 20-nm Si were made on these substrates. The Si cap was employed to minimize oxygen contamination. All samples were sequentially annealed at 600 °C, 30 s and 900 °C, 60 s in vacuum at $<7\times10^{-7}$ Torr. 2-MeV He backscatter spectrometry and x-ray diffraction (Read camera) were used to characterize the stoichiometry and structure of sections of each wafer. This showed the formation of 120-nm $CrSi_2$ in each case.[4] A slight (<10 nm) excess of Si was present at the surface of the samples on SiO_2. The samples were cleaved into 8×8 mm squares and electrically characterized before further use by four-point probe measurements of sheet resistance and Hall coefficient at room temperature, using standard methods.[6] There was negligible substrate conduction in the samples on the n-type $<100>$ Si or SiO_2 substrates; these $CrSi_2$ films were p-type with typical resistivities of $\sim$4400, $\sim$5500 $\mu\Omega$ cm, carrier concentrations of ~1, $\sim2\times10^{20}$ cm^{-3}, and Hall mobilities of ~13, ~7 cm^2/V s, respectively. The substrate contributed $\sim50\%$ to the measured film conductivity in the samples on the p-type $<111>$ Si wafer.

Two complementary irradiation experiments were performed. In one, samples were irradiated at room temperature (RT) with Xe at energies of 300–600 keV to fluences of 10^{11}–10^{15} Xe cm^{-2} at particle current densities, corresponding to a singly charged ion, of 2–100 nA/cm^2. The irradiated films were then characterized as before. The second set of experiments employed four-point electrical resistivity measurements of $CrSi_2$ films on SiO_2 made *in situ* with 300–500-keV Xe irradiation at room temperature and 77 K. Measurements were made for accumulated doses of 2×10^{10}–10^{15} ions cm^{-2}. Constant particle current density was maintained during irradiation, typically in the range 0.8–5 nA/cm^2. The relative uncertainty in dosimetry was $<1\%$ for a given run, and the absolute uncertainty was estimated to be $<10\%$. Similar implantations with 150-keV Ar and 90-keV Ne at room temperature were also performed.

Except for the 600-keV Xe irradiation, the (mean damage depth) + (damage straggling)$^{1/2}$ was less than the 120-nm $CrSi_2$ film thickness for all ions and energies used.[7] A thin film of thermally conductive paste (Dow Corning 340) was used to secure the samples to an implantation carousel of large thermal mass. We estimate the sample temperature to have risen less than 0.01 °C/nA cm^{-2}.

III. RESULTS

$CrSi_2$ film conductance increases with incident ion fluence ϕ for room-temperature Xe and Ar irradiation. Samples irradiated with Xe at 77 K, or with Ne at RT initially display a $\sim2\%$ decrease in conductance at fluences $<10^{11}$ cm^{-2}, beyond which the conductivity also increases with fluence. The film conductance $g(\phi)$ saturates at 5–12$\times$ its initial value g_0 for fluences of 6×10^{13}–10^{15} cm^{-2}. The apparent saturation level increases when larger particle current densities are employed. Additional investigations indicate that this is not the result of Joule heating.

Typical *in situ* results at fixed Xe current density for two irradiation temperatures are shown in Fig. 1. The ratio of

[a] Permanent address: Shanghai Institute of Metallurgy, Academy of Sciences of China, Shanghai, China.

 0021-8979/86/093077-04$02.40

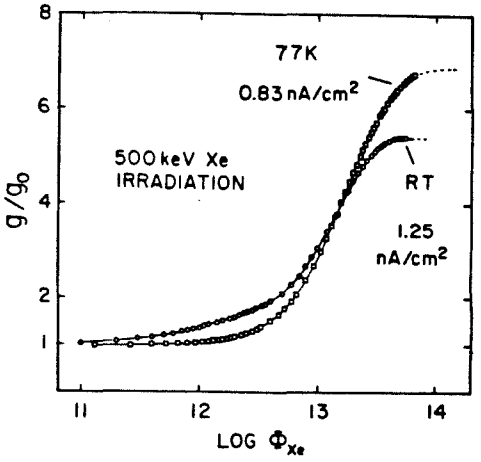

FIG. 1. Change in relative $CrSi_2$ film conductance $g(\phi)/g_0$ vs fluence ϕ, measured *in situ*, for 500-keV Xe irradiation at RT and 77 K.

conductance after fluence ϕ to initial conductance $g(\phi)/g_0$ is plotted semilogarithmically versus fluence ϕ for 500-keV Xe irradiations. The behavior is similar for other energies and ions. No significant substrate dependence was observed (correcting for background substrate conduction in $CrSi_2$ films grown on the $p<111>$ Si substrates).

The Hall effect measurements do not reveal a substantial change in the magnitude of the Hall mobility for Xe fluences below $10^{14}\,cm^{-2}$, although there is an apparent conversion to predominantly *n*-type conductivity at fluences exceeding 10^{12}–$10^{13}\,cm^{-2}$.

It was observed in *in situ* experiments that at room temperature, though not at 77 K, the film conductiviy decreases by 1–5% over a 20–60 s period after suspending irradiation. The temperature coefficient of resistivity is positive in this temperature range and cannot explain this change. Additionally, the magnitude and time scale are not consistent with thermal decay. Some self-annealing apparently occurs at room temperature.

IV. DISCUSSION

Our observations suggest that the enhancement of $CrSi_2$ conductivity results primarily from an increase in free-carrier concentration. We speculate that these carriers, possibly electrons, arise from completely ionized defects produced by the irradiation. The high mobility we observe (~ 10 $cm^2/V\,s$) relative to $\mu_n = 0.15\,cm^2/V\,s$ for electrons[4] suggests conduction via an impurity band. Figure 2 shows the variation in film resistivity with temperature before and after the LNT irradiation. The cooling curve is consistent with previous reports.[5] Carrier freeze-out is not an interference in this experiment.

The curves of g/g_0 vs ϕ exhibit a simple structure at high fluences ($>10^{13}\,cm^{-2}$), indicating that a first- or possibly second-order process may be responsible for saturation.[8] This suggests plotting $d(g/g_0)/d\phi$, which was calculated using three-point Lagrangian interpolation, versus g/g_0, as

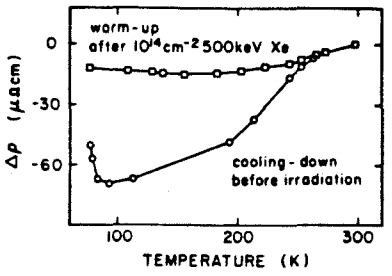

FIG. 2. Graph of resistivity change *relative to RT value* vs temperature for $CrSi_2$ film before and after irradiation at 77 K with $10^{14}\,cm^{-2}$, 500-keV Xe.

shown in Fig. 3 for samples implanted with 500 keV Xe at room temperature, 77 K, and with 150-keV Ar. The results for all *in situ* room-temperature implantations display similar behavior. All of the curves have a similar shape for $g/g_0 > \sim 2$, independent of temperature. One mechanism probably dominates this regime. Considering the behavior for $g/g_0 < \sim 2$, there appears to be an additional process present during RT irradiation which is suppressed at 77 K. It is evident from Fig. 3 that there is a nearly linear relationship

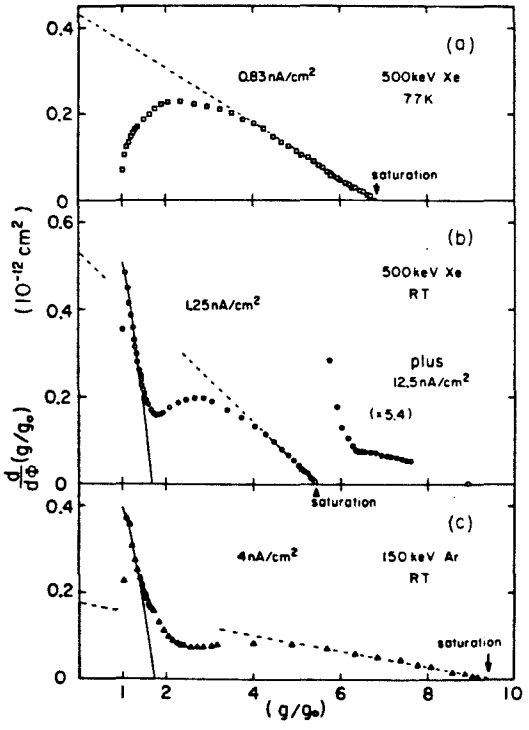

FIG. 3. Graph of $d(g/g_0)/d\phi$ vs (g/g_0) for 500-keV Xe irradiation at 77 K, RT and for 150-keV Ar at room temperature: (a), (b), and (c) respectively. In (b), the Xe current density was increased to 12.5 nA/cm^2 after saturation had occurred at 1.25 nA/cm^2 for a dose of $\sim 10^{13}$ Xe cm^{-2}.

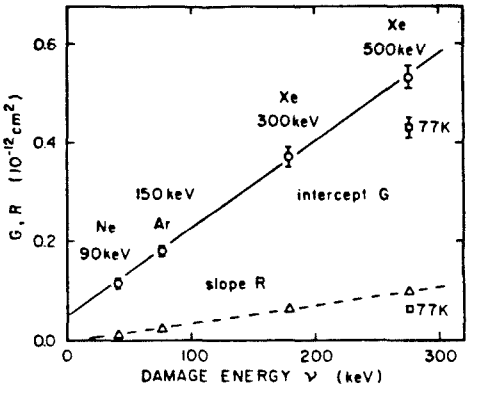

FIG. 4. Graph of intercept G and slope R vs damage energy ν for various ion-energy combinations studied.

between $d(g/g_0)/d\phi$ and (g/g_0) as they approach zero and saturation, respectively:

$$\frac{d}{d\phi}\left(\frac{g}{g_0}\right) = G - R\left(\frac{g}{g_0}\right). \tag{1}$$

In Fig. 4 we plot the values of G and R derived from this asymptotic dependence (dashed lines in Fig. 3) versus the deposited damage energy ν for the various ion-energy combinations studied.[7] The predominately linear dependence suggests that G corresponds to the generation of defects by the incident ion's nuclear energy loss, while existing defects recombine via radiation-enhanced diffusion.[9,10] The typical influence of dose rate on damage in $CrSi_2$ is demonstrated in Fig. 3(b). Further increases in g/g_0 were produced after saturation was reached ($\phi \simeq 10^{15}$ cm^{-2}) at a Xe current density of 1.25 nA/cm^2 by raising the current to 12.5 nA/cm^2. This effect requires further systematic investigation.

Simple models of overlapping coverage[10,11] are not adequate to describe the saturation at high fluences. However, they may be pertinent to the room- temperature behavior in Figs. 3(b) and 3(c) for $g/g_0 < 2$. If an incident ion produces an initial change in conductivity which is large compared to that produced by subsequent overlapping cascades, then $d(g/g_0)/d\phi$ would decrease substantially when $a\phi \gg 1$, where (a) is the effective area of the initially modified region. The solid lines in Figs. 3(b) and 3(c) correspond to such a model, assuming that subsequent impacts produce no additional change (see Appendix). By fitting these lines to the data, we deduce effective areas of $(8.7)^2$, $(10)^2$ nm^2 for 150-keV Ar, 500-keV Xe irradiation, respectively. The areas corresponding to transverse damage straggling $\pi \langle y^2 \rangle_D$ are $(33)^2$, $(44)^2$ nm^2, respectively, using Winterbon's calculations.[7] Recent studies of ion irradiation damage in tungsten using field ion microscopy[12] show that the average radius of the damaged region is $\sim 0.25 \langle y^2 \rangle_D^{1/2}$. These results show that our estimates of (a) are quite reasonable. The fact that the initial transient vanishes at 77 K indicates that the initial process occuring at RT involves defect diffusion and/or complex formation. The defects may not be sufficiently mobile at 77 K to produce this effect. This reduced mobility of defects may also account for the reduced values of G and R at 77 K in Fig. 4. The slight initial reduction in conductivity for fluences below 10^{11} cm^{-2} is accordant with this model of localized damage, since a reduction in carrier (hole) mobility due to scattering from these dispersed regions may dominate at very low fluences.

The 77 K result shown in Fig. 3(a) suggests that an electrically active compound defect is responsible for the increase in film conductivity. A significant feature is that $d(g/g_0)/d\phi$ initially starts near zero and increases very rapidly with respect to (g/g_0). This indicates that other electrically inactive defects are formed first and subsequently lead to formation of the active defect. The behavior at 77 K can be explained formally by the following model. We assume that the formation of the active defect A is limited by the formation of a simple inactive precursor defect I. All other intermediaries are assumed to be steady state, and competing reactions are neglected. The model can be described by the coupled reactions

$$0 \underset{(k_2)}{\overset{(k_1)}{\rightleftharpoons}} \{?\} + I, \tag{2a}$$

$$I + \{?'\} \underset{(k_4)}{\overset{(k_3)}{\rightleftharpoons}} A, \tag{2b}$$

where $\{?\}$ and $\{?'\}$ refer to unspecified defects. In this case quasi-first- order chemical kinetics apply, and the corresponding concentrations $C_a(\phi)$, $C_i(\phi)$ follow[13]:

$$\frac{d}{d\phi}C_i = k_1 - k_2 C_i - \frac{d}{d\phi}C_a, \tag{3}$$

$$\frac{d}{d\phi}C_a = k_3 C_i - k_4 C_a, \tag{4}$$

where the empirical rate constants k_1, k_2, k_3, k_4 depend on ion flux $d\phi/dt$, deposited energy ν, steady-state densities of other defects, etc. $g - g_0$ is assumed proportional to C_a; $(g/g_0) - 1 = \beta C_a$. The solution of Eqs. (3) and (4) for $C_i(0) = C_a(0) = 0$ gives

$$C_a(\phi) = \frac{(k_1 k_3)}{pq}\left(1 - \frac{pe^{-q\phi} - qe^{-p\phi}}{p - q}\right), \tag{5}$$

where

$$p,q = \frac{k_2 + k_3 + k_4}{2} \pm \left[\left(\frac{k_2 + k_3 + k_4}{2}\right)^2 - k_2 k_4\right]^{1/2}.$$

There are three relevant empirical parameters; $(\beta k_1 k_3)$, p, and q. We assume $p \neq q$. The asymptotic behavior for this model is

$$\frac{d}{d\phi}C_a \sim \left(\frac{k_1 k_3}{p}\right) - qC_a, \quad \text{as } \phi \to \infty, \tag{6a}$$

and as $\phi \to 0$;

$$\frac{d}{d\phi}C_a \sim (2k_1 k_3 C_a)^{1/2}\left[1 - \left(\frac{p+q}{3}\right)\left(\frac{2C_a}{k_1 k_3}\right)\right]^{1/2}, \tag{6b}$$

which is clearly the desired behavior. Figure 5 shows the result of fitting this simple model (solid line: $\beta k_1 k_3 = 9.01 \times 10^{-26}$ cm^4, $q = 0.064 \times 10^{-12}$ cm^2, $p = 0.24 \times 10^{-12}$ cm^2) to the results of Fig. 3(a). The agreement is excellent, although only suggestive. Variations of this model may also fit equally as well. A physical model requires knowledge of $CrSi_2$ defect chemistry which is lacking at

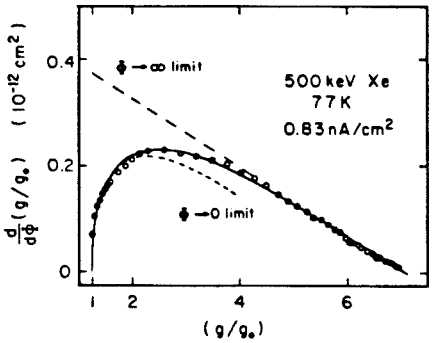

FIG. 5. Result of fitting simple coupled reaction model Eq. 5, (solid line) to 77 K Xe irradiation data (open circles) from Fig. 2(a). Asymptotic behavior is shown by dashed lines [from Eqs. 6(a), 6(b)].

present. It is likely that k_1 follows a Kinchen–Pease dependence (e.g., nearly linear in damage energy ν).[14] General statements about the other rate constants are not so obvious.

V. CONCLUSIONS

Our preliminary investigations have revealed a substantial amount of structure in the fluence dependence of inert ion implantation on $CrSi_2$ conductivity. Several processes seen in other systems have been tentatively identified. Electrical measurements provide a good qualitative characterization, but are relatively nonspecific and nonunique in their interpretation. Structural analysis from TEM, etc., is essential. The defect chemistry of $CrSi_2$ needs to be considered. The thermal annealing behavior of implanted $CrSi_2$ may offer some insight. Further investigation of irradiation damage in $CrSi_2$ at very low fluences ($\sim 10^{10}$ cm^{-2}) shows promise in elucidating the damage process, especially with light ions (e.g., Ne). $CrSi_2$ may be a good material to use in the study of dose rate effects.

ACKNOWLEDGMENTS

We thank A. Ghaffari for assistance with the evaporations and A. Collinwood for manuscript preparation. We acknowledge the partial financial support by the Office of Naval Research under Contract no. N00014-84-K-0275 (D. Polk). T. Banwell thanks IBM for a fellowship during this work.

APPENDIX

The effective conductivity of a two-dimensional medium composed of a random arrangement of regions with conductivities σ_0 and $b\sigma_0$ with fractional coverage $1-p$, p, respectively can be approximated by[15]:

$$y^2 - y(2p-1)(b-1) - b = 0,$$

where $y = \sigma/\sigma_0$. In our problem $p = 1 - \exp(-a\phi)$ is the fraction of area involved in at lease one cascade and possessing conductivity $b\sigma_0$. Differentiating and rearranging gives

$$\frac{d}{d\phi}y = a(b-y)\left(\frac{y^2+y}{y^2+b}\right).$$

The values of b used in Figs. 3(b) and 3(c) were determined by trial and error, with $b = 1.67$ and 1.71, respectively, producing reasonable agreement with the experiment.

[1]J. C. Hensel, R. T. Tung, J. M. Poate, and F. C. Unterwald, Nucl. Instrum. Methods (in press).
[2]C. A. Hewett, I. Suni, S. S. Lau, L. S. Hung, and D. M. Scott, in *Ion Implantation and Ion Beam Processing of Materials*, Vol. 27, edited by G. K. Hubler, O. W. Holland, C. R. Clayton, and C. W. White (North-Holland, New York, 1984), p. 145.
[3]U. Shreter and J. Nuchols (unpublished).
[4]M-A. Nicolet and S. S. Lau, in *VLSI Electronics: Microstructure Science*, Vol. 6, edited by N. Einspruch and G. Larrabee (Academic, New York, 1983), p. 391.
[5]F. Nava, T. Tien, and K. N. Tu, J. Appl. Phys. **57**, 2018 (1985).
[6]L. J. Van der Pauw, Phillips, Res. Rep. **13**, 1 (1958).
[7]K. B. Winterbon, *Ion Implantation Range and Energy Deposition Distributions* (IFI Plenum, New York, 1975).
[8]R. C. Birtcher, R. S. Averback, and T. H. Blewitt, J. Nucl. Mater. **75**, 167 (1978).
[9]G. J. Dienes and A. C. Damask, J. Appl. Phys. **29**, 1713 (1958).
[10]R. Webb and G. Carter, Radiat. Effects **42**, 159 (1979).
[11]R. P. Webb and G. Carter, Radiat. Effects **59**, 69 (1981).
[12]C-Y. Wei, M. I. Current, and D. N. Seidman, Philos. Mag. A **44**, 459 (1981).
[13]R. Sizmann, J. Nucl. Mater. **67–70**, 386 (1980).
[14]B. M. Paine and B. X. Liu, in *Materials Surfaces, Part A: Modification*, edited by C. R. Clayton and J. B. Lumsden (Academic, New York), (in press).
[15]S. Kirkpatrick, Phys. Rev. Lett. **27**, 1722 (1971).

Appendix AIII.4 Saturation of Si Activation at High Doping Levels in GaAs

This is a pre-print from *Journal of Physics and Chemistry of Solids* 44

J. Phys. Chem. Solids Vol. 44, No. 6, pp. 507–514, 1983
Printed in Great Britain.

0022-3697/83/060507-08$03.00/0
Pergamon Press Ltd.

SATURATION OF Si ACTIVATION AT HIGH DOPING LEVELS IN GaAs

T. C. BANWELL, M. MÄENPÄÄ† and M-A. NICOLET
California Institute of Technology, Pasadena, CA 91125, U.S.A.

and

J. L. TANDON‡
Rockwell International Science Center, Thousand Oaks, CA 91360, U.S.A.

(*Received* 12 *April* 1982; *accepted in revised form* 11 *August* 1982)

Abstract—Ion implantation of Si is extensively employed in the fabrication of GaAs integrated circuits as an *n*-type dopant. We have investigated the electrical activation of Si in GaAs with high dose (10^{17}–10^{19} cm^{-3}) room temperature Si implantations in semi-insulating GaAS. A co-implantation of As with Si was used to study the influence of local stoichiometry and substrate morphology on the electrical activation of Si. A van der Pauw method was employed for electrical characterization. Our results show that the previously reported saturation in the free electron concentration at 2×10^{18} cm^{-3} is not altered by co-implanted As.

We compile our results with those of several publications to obtain the electrical activation after ~850°C annealing for implanted Si in the concentration range 10^{16}–10^{20} Si cm^{-3}. A quantitative description of the saturation effect is presented and discussed in terms of a simple saturation mechanism.

1. INTRODUCTION

Ion implantation of Si is extensively employed in the fabrication of high speed GaAs integrated circuits as an *n*-type dopant[1, 2]. Electrical activation near 80% is obtained with low-dose room temperature implantations[1–3]. There exists, however, an upper 2×10^{18} cm^{-3} limit on the achievable free electron concentration[3] for high-dose Si implantations. Free electron concentrations exceeding 10^{18} cm^{-3} are required for producing good ohmic contacts on GaAs[1]. Silicon is a shallow substitutional amphoteric dopant in GaAs, acting as a donor when substituted for a Ga; Si_{Ga}, and as an acceptor when substitued for an As; Si_{As}[4]. Silicon is preferentially substitutional on Ga sites at low doses; however, it has been proposed that compensation occurs at high Si doses through the formation of $Si_{Ga}Si_{As}$ neutral neighbor pairs[3], occupation of acceptor sites[5, 6], $Si_{Ga}V_{Ga}$ complex formation[7, 8], or from a local deviation in stoichiometry[9–11]. It has also been proposed that the dual implantation with a complementary ion will enhance electrical activation by maintaining local stoichiometric balance[9–11]. Dual implantations of Ga with Se have shown an enhanced activation of Se above that observed for single Se implantations[10]. Recent studies did not reveal a corresponding increase in the upper limit of free carrier concentration obtained with Si and P or As dual implantations, though a given level of activation was achieved at reduced annealing temperatures[9, 11].

We have made a systematic investigation using a dual implantation of As with Si to study the influence of local stoichiometry and substrate morphology on the electrical activation of Si. We compile our results and those of several publications to obtain the electrical activation of implanted Si in GaAs after ~850°C annealing. A quantitative description of the saturation effect is presented. Finally, we discuss a simple characterization of the saturation mechanism.

2. EXPERIMENTAL PROCEDURES

Semi-insulating Bridgman ⟨100⟩ Cr doped GaAs was implanted at room temperature (R.T.) with 150 keV Si to a dose of 10^{13}, 10^{14} or 10^{15} ions cm^{-2}. Room temperature coimplantations of 360 keV As were also made to doses either five times less, equal to, or five times greater than the primary Si dose. The implanted samples were encapsulated with 2000 Å of reactively sputtered Si_3N_4 and annealed at 850 or 900°C for 30 min in flowing hydrogen. All implanted and annealed samples were characterized by sheet electrical measurements using a conventional van der Pauw method. A standard anodic stripping technique was employed for depth profiling of selected samples[12].

3. RESULTS

Results of the Hall measurements are presented in Figs. 1(a) and 1(b) showing sheet electron concentration (N_s) vs Si dose for annealing at 900 and 850°C, respectively. The solid line serves as a reference corresponding to 100% activation. Seventy percent electrical activation is obtained with the 10^{13} cm^{-2} Si dose, independent of annealing temperature or coimplanted As dose. Samples implanted to 10^{15} Si cm^{-2} show limited (≤10%) activation attributed to compensation, with only a slight enhancement from the coimplanted As. There is incomplete activation at 850°C as indicated by the two-fold increase in electrical activation at 900°C. The annealing dependence is consistant with previously reported results for

†Permanent address: Semiconductor Laboratory, Technical Research Centre of Finland, SF-02150 Espoo 15, Finland.
‡Present address: M/A-COM Gallium Arsenide Products, Burlington, Massachusetts, U.S.A.

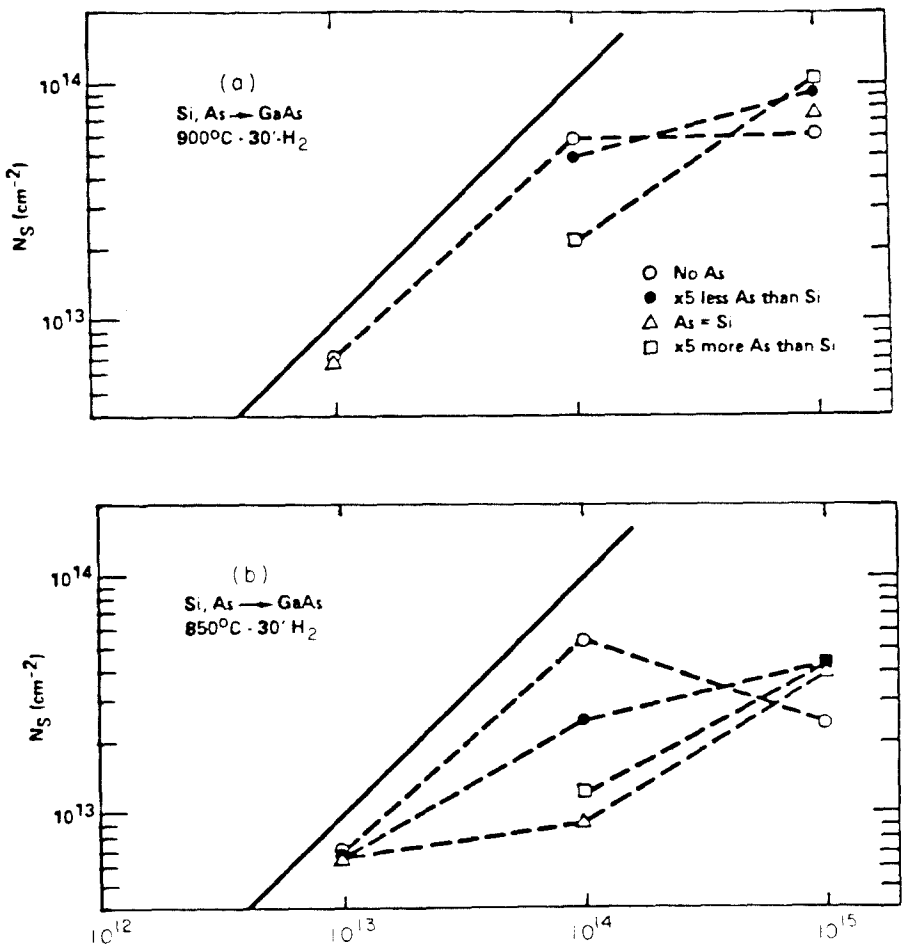

Fig. 1. Measured sheet electron concentration vs Si dose following annealing at (a) 900°C and (b) 850°C.

single implants[1]. In contrast to the 10^{13} and 10^{15} Si cm^{-2} cases, there is a discernible effect of As on the electrical activity at 10^{14} Si cm^{-2} with 850°C annealing. This effect diminishes at 900°C though the peak sheet concentration does not significantly increase. At both 850 and 900°C annealing, there is ~50% electrical activation with 10^{14} Si cm^{-2} in the absence of As. An additional As implantation initially decreases the sheet carrier concentration with increasing As dose. There is a slight recovery in activity between the 10^{14} and 5×10^{14} As cm^{-2} coimplanted samples at 850°C.

Figure 2 shows the sheet Hall mobility vs Si dose for each annealing temperature. The mobility displays the same behavior generally observed for single Si implantations. The increased dispersion in mobility at 850°C relative to 900°C is probably due to incomplete annealing at the lower temperature.

Measured free electron concentration n and mobility profiles for samples implanted with 10^{15} Si cm^{-2} and annealed at 900°C are shown in Fig. 3. The Si and equal-dose As profiles calculated using LSS range parameters are also shown[13]. The free electron profiles are essentially constant at 1.6×10^{18} cm^{-3}, independent of As coimplantation. Dispersion in the profiles is within expected experimental uncertainties. The integrated concentrations (from surface to ~0.5 μm) agree within 25% with the measured sheet values. Coimplanted As has a negligible effect on the mobility profile. It is inferred from the close correlation of these profiles with the surface measurements of Figs. 1 and 2 and previously published results[1-3] that the substrates, the sample preparation, and the measurement techniques employed here are reproducible.

The effect of coimplanted As on the free electron concentration n and mobility profiles for samples implanted with 10^{14} Si cm^{-2} and annealed at 850°C is shown in Fig. 4. LSS profiles for the Si and equal-dose As implantations are drawn for comparison. Arsenic has a pronounced effect on the free electron concentration, as indicated by the surface measurements of Fig. 1(b). The limitation of the free electron concentration at ~10^{18} cm^{-3} is evident in samples with little or no As. The integrated concentrations (from surface to ~0.35 μm) agree within 30% of the corresponding sheet values. An equal implantation of As at 10^{14} cm^{-2} reduces the free electron concentration near the surface by a factor of 25, and produces a significant depth dependence. With a large As dose, the free electron concentration n approaches the saturation level though there is a step at approximately R_p of the LSS profile.

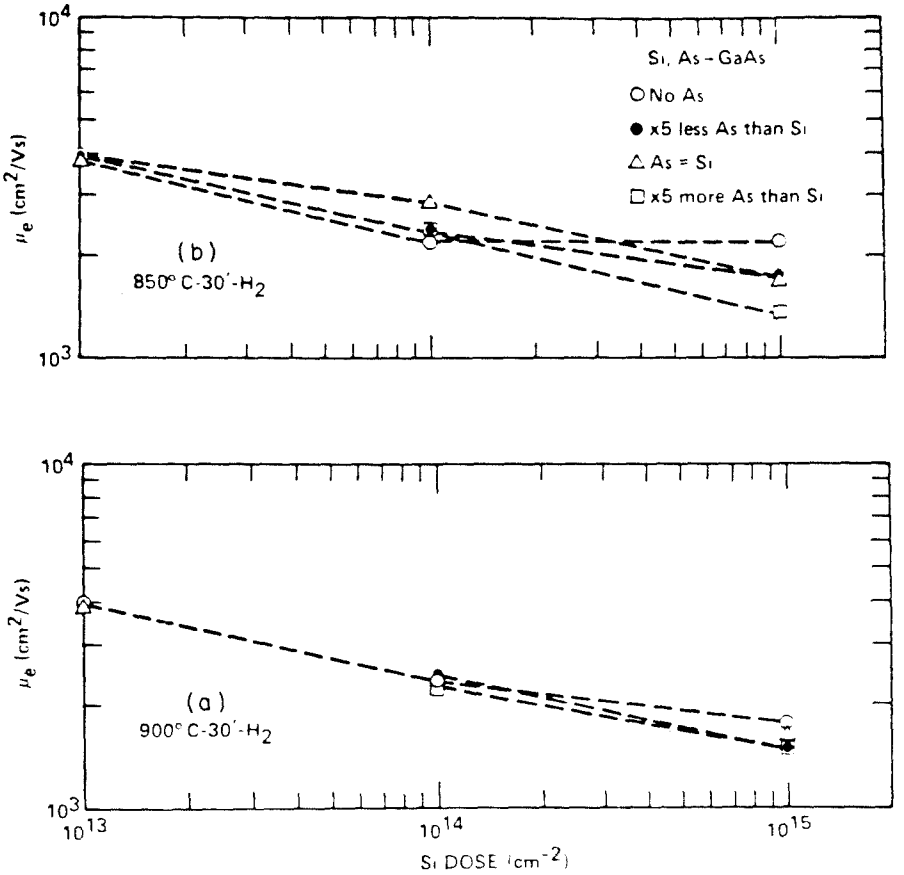

Fig. 2. Measured sheet Hall mobility vs Si dose following annealing at (a) 900°C and (b) 850°C.

4. DISCUSSION

4.1 *Interpretation of dual implantation results as a consequence of thermal equilibrium*

It is evident that an enhanced free electron concentration cannot be obtained with Si by altering the local stoichiometry with coimplanted As at R.T. The similar behavior reported by Stoneham *et al.*[10] for coimplanted P with Si indicates that the threshold is not a function of compensating species.

The electrical profiles for 10^{14} Si cm^{-2} (Fig. 4) suggest that the morphology of the implanted layer is a factor affecting Si activation. In contrast to the behavior shown for 10^{13} and 10^{15} Si cm^{-2}, coimplanted As has a strong influence on the Si activity at 10^{14} cm^{-2}, although the effect is contrary to prediction[11].

We note that this latter dose coincides with the transition region between the formation of a damaged single crystalline layer and the full amorphization of GaAs by R.T. implantation of As[14], or Si[14, 15] in the energy range of hundreds of keV. The As dose dependence observed in Fig. 4 most probably arises from an explicit dependence of the residual damage on the As dose in that transition region. The pronounced decrease in free electron concentration at the surface with 10^{14} As cm^{-2} implantation is probably due to incomplete annealing. The sheet measurements (Fig. 1) show that the effect of As is less pronounced at 900°C than at 850°C. This further substantiates our conclusion that the effects seen in Fig. 4 are structural in origin. Extrapolation of amorphization ranges reported for As in GaAs[14] indicates that a 5×10^{14} cm^{-2}, 360 keV As will produce a fully amorphous region extending to 1–2 R_p. The recovery of the free electron concentration observed with 5×10^{14} cm^{-2} As implantation can therefore be attributed to improved regrowth from the amorphous state. This correlation is supported by TEM studies of Se-implanted GaAs, which indicate that residual damage remaining after a 500°C anneal is decrescent at high Se doses[16].

The markedly different behavior of the As coimplantation with 10^{14} and 10^{15} Si cm^{-2} (Figs. 4, 3 respectively) also imply that the influence of coimplanted As on the free electron profiles in Fig. 4 is associated with changes in substrate morphology rather than stoichiometry. Extrapolation of results for the amorphization of GaAs by implanted Si, as established by RBS channeling measurements[14] and X-ray rocking curve studies[15], indicate that GaAs is fully amorphous to a depth of $\sim 2R_p$ after R.T. implantation of 10^{15} Si cm^{-2}. The subsequent As implantation into the amorphized layer is thought to merely extend the region. It has been shown for single species implantation that regrowth is primarily governed by the initial amorphous layer thickness, irrespective of ion species or dose[14]. It is therefore likely that the residual damage is qualita-

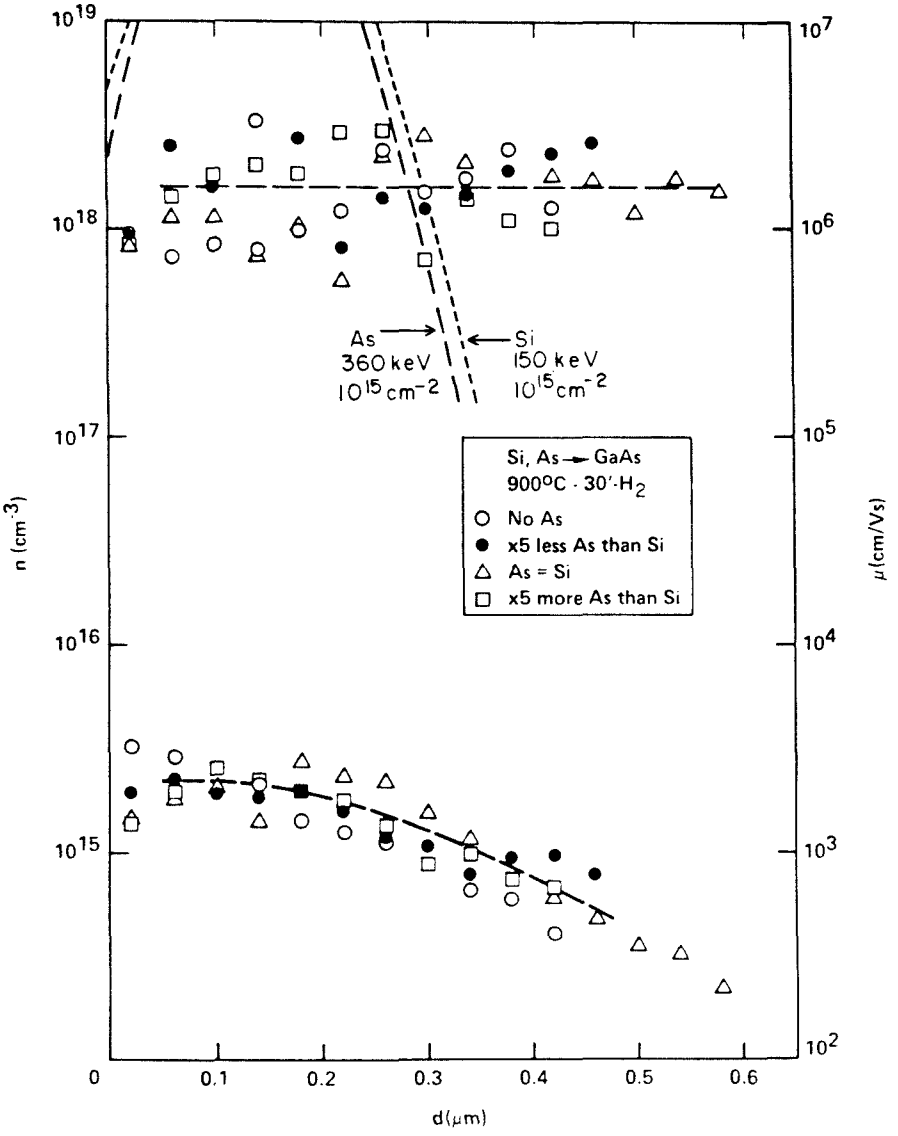

Fig. 3. Measured free electron concentration (top) and Hall mobility for samples implanted with 10^{15} Si cm^{-2} and annealed at 900°C.

tively the same for all samples coimplanted with 10^{15} Si cm^{-2}, to which we attribute the absence of the As coimplantation effect seen in Fig. 3.

Our results show that the dual implantation of As with Si has a very minor influence on Si electrical activation, except for the case tentatively attributed to imperfect GaAs regrowth. There is no effect on the upper 2×10^{18} cm^{-3} free electron limit. We interpret this behavior as resulting from the establishment of thermal equilibrium at the annealing temperature. The concentration of native defects like V_{As} can exceed 10^{19} cm^{-3} in GaAs annealed above 700°C[17, 18]. Consequently, significant As redistribution should occur through vacancy substitution at our annealing temperatures. Implanted As could possibly occupy Ga sites as the anti-site defect As_{Ga}[19], presumably a shallow donor. Our results, however, do not reveal a nelectrical activation associated with implanted As. Additionally, As could remain interstitial or as an interstitial complex[19], although this does not appear to be significant in annealed bulk GaAs[17].

It is evident from the width of the electrically active regions reported in Figs. 3 and 4 that As does not significantly influence Si redistribution during annealing at 850–900°C. The free electron profiles in Fig. 3 are consistant with previously reported Si implantation results, for which SIMS analysis showed that Si redistribution extends to 2–3 R_p after 900°C annealing for 30 min[3]. This may be associated with ion irradiation induced damage in the GaAs, which has a similar depth dependence[14, 15].

4.2 *Compilation of Si activation data*

The results on electrical activation reported for R.T. implanted Si do not seem to depend explicitly on implantation energy. Electrical activation results calculated from the present experiments and from previously pub-

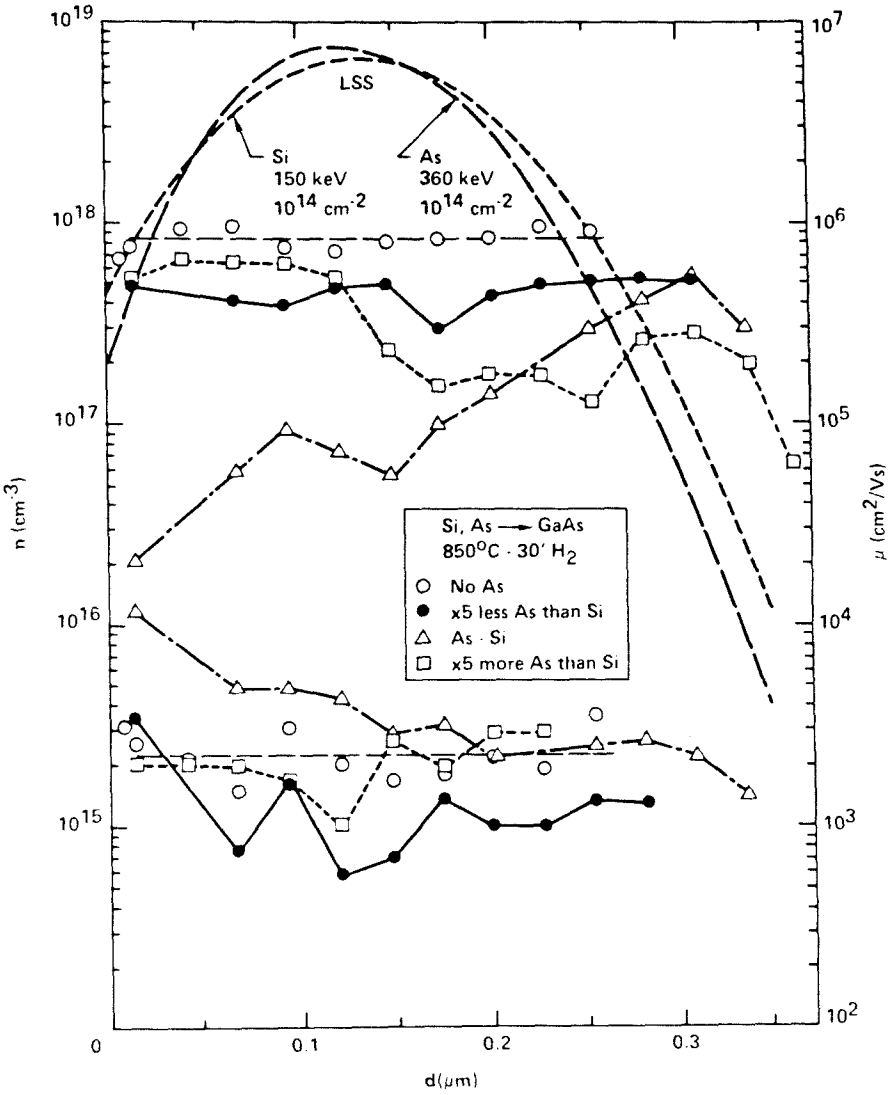

Fig. 4. Measured free electron concentration (top) and Hall mobility for samples implanted with 10^{14} Si cm^{-2} and annealed at 850°C.

lished results[1–3, 9, 11] are compiled together in Fig. 5, showing activation $a = n/n_{Si}$ vs Si concentration (n_{Si}). We report only those results for which an ~850°C post-implantation annealing was performed. Whereas both Si concentration and activation or free electron concentration are reported by Masuyama *et al.*[3], and Hobgood *et al.*[2], measured Si profiles were not available in the other cases. In those cases, the electrical activation results reported in Fig. 5 were calculated from sheet concentrations, the free electron profile, and the known Si implantation dose ϕ, as follows. The free electron concentration (n) was calculated from the measured free electron profile $n_{meas}(x)$ normalized to agree with the measured sheet electron concentration N_s; i.e.

$$n(x) = n_{meas}(x)\frac{N_s}{\int n_{meas}(\xi)\,d\xi}. \qquad (1)$$

The Si concentration profile was assumed to be rectangular, extending the width d of the free electron profile at ~0.75 of the maximum, with $n_{Si} = \phi/d$, where ϕ is the implanted Si dose. Extensive Si diffusion, which would significantly violate this assumption, does not occur for annealing to 900°C[1, 3, 9, 11]. Below saturation, the free electron profile was assumed to reflect the qualitative behavior of the Si profile. The broadly peaked profiles reported in Ref. [1] and Ref. [11] at low doses further support a rectangular profile approximation. The results of these calculations plotted together in Fig. 5 all fit on a single S-shaped curve, even though they represent independent investigations. For comparison purposes, it is useful to consider the graph of

$$\log\left[\frac{\text{Si not acting as a donor}}{\text{Si acting as a donor}}\right] = \log\frac{n_{Si}-n}{n} = \log\left(\frac{1}{a}-1\right)$$

presented in the upper portion of Fig. 5.

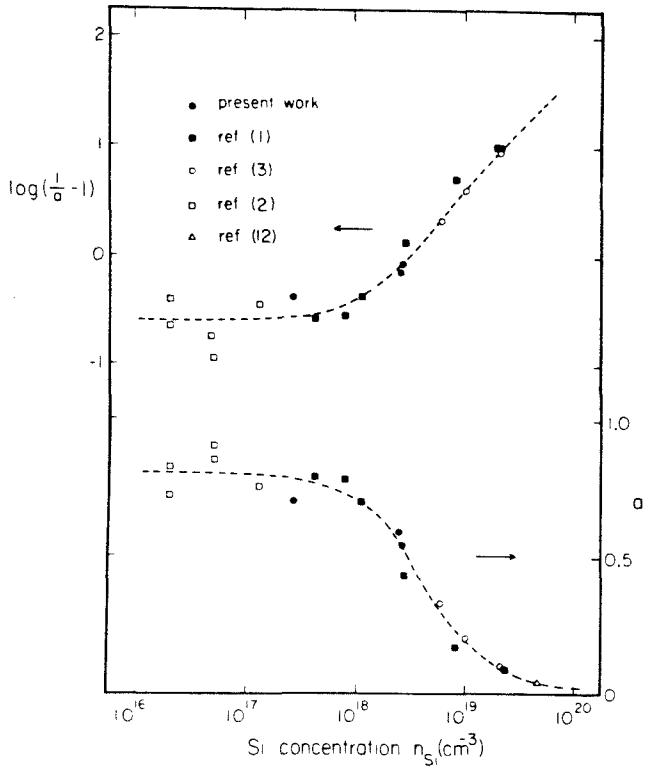

Fig. 5. Compilation of electrical activation results calculated from present experiments and published works.

Figure 5 shows that a constant 80% activation is obtained for Si concentrations n_{Si} below 10^{18} cm^{-3}. The free electron concentration $n = a \cdot n_{Si}$ saturates at 2×10^{18} cm^{-3} for n_{Si} above $\sim 2 \times 10^{18}$ cm^{-3}. Identical behavior has been reported for bulk Si doped GaAs annealed at 1200°C, in which Si concentrations n_{Si} below 2.3×10^{18} cm^{-3} produces 80% activation and saturation occurs at $n \simeq 4 \times 10^{18}$ cm^{-3} for n_{Si} exceeding 6×10^{18} cm^{-3}[5]. Kung *et al.* have shown that the saturation level differs by a factor of two in bulk Si doped GaAs when annealed at 1100°C vs 700–900°C[20]. These observations support the theory of Whelan *et al.*[5] that the general shape of the saturation curve should not be strongly temperature dependent.

4.3 *Formal model for saturation behavior*

The electrical activation of Si shown in Fig. 5 can be formally described by a simple model of saturation. We partition the Si between an active state and an inactive state, for which we hypothesize a maximum occupancy of n_0 and $n_1 \gg n_0$, respectively (see diagram in Fig. 6). The activation for this model, derived in Appendix I, is given by

$$a = \frac{\left(1 - \frac{n_{Si}}{n_0} a\right)}{\left(1 + \theta - \frac{n_{Si}}{n_0} a\right)} \qquad (2)$$

where $\theta \equiv (n_1/n_0) \exp(-\Delta\epsilon)$ and $\Delta\epsilon(>0)$ is the difference in the formation energy of the two states. The dashed lines in Fig. 5 are obtained from eqn (2) with $n_0 = 2 \times 10^{18}$ cm^{-3} and $\theta = 0.25$. It is obvious that the saturation effect in the model arises from $1 - (n_{Si}/n_0)a \to 0$ corresponding to completely filling the allowed n_0 low energy states. We associate the restricted density of active states n_0 in the formal model with that concentration at which Si becomes equally partitioned between acceptor and donor sites through a Fermi level dependent process, as proposed by Longini *et al.*[21].

The constant partial activity at low Si concentrations indicates the presence at low doping of a compensating process without an explicit Fermi level dependence. However, background doping effects complicate specific interpretation of the low dose behavior[2]. The incomplete activation in our formal model arises from the existance of the hypothetical inactive states.

4.4 *A characterization of the saturation mechanism*

Numerous investigations have been published discussing the identity of the species responsible for compensation in highly Si doped GaAs. Several species have received attention: Si_{As}^{-} from thermal considerations[20] and IR LVM studies[6], $Si_{Ga}Si_{As}$ from IR absorption studies[22], $Si_{Ga}V_{Ga}$ from thermomechanical considerations[8] and IR LVM studies[7], and possibly other defects[23]. The sharp saturation in the free electron concentration shown in Fig. 5 and in Ref. [5] at high Si concentrations provides information about the compensating specie if that single specie dominates the process. The results reported in Fig. 5 imply that $d \log a / d \log n_{Si} = -1.0 \pm 0.1$ for $n_{Si} > n_0 \simeq 2 \times 10^{18}$ cm^{-3},

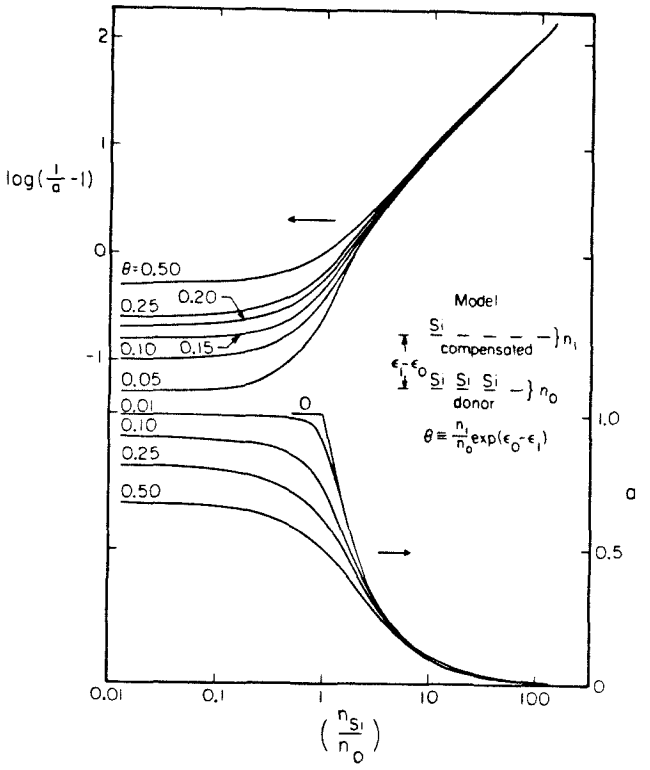

Fig. 6. Graph of electrical activation for a simple model of saturation. The model is illustrated on the right. Various values of free energy parameter θ are considered.

as indicated by eqn (9) of the Appendix. The results reported in Fig. 1 of Ref. [5] also imply that $d \log a/d \log n_{Si} = -1.0 \pm 0.1$ for $n_{Si} > 6 \times 10^{18}\,cm^{-3}$. Brouwers method[24] will be employed here to calculate the Si electrical activation assuming a single species A dominates the compensation mechanism. This is suggested by the simple structure of the activation curves.

We consider A to occupy the single charge state $-\gamma$, $\gamma \geq 0$. We define λ to be the number of bound Si in A. It will be assumed that thermal equilibrium is achieved during annealing. Except for Fermi level effects, we shall assume that changes in defect concentrations associated with the formation of A can be neglected; that is, we shall ignore the competition between equilibria not involving Si_{Ga} or A. Additionally, the usual approximations regarding defect freeze-in after annealing[19], and the use of the Boltzmann approximation[8] at the annealing temperature are made. Within the context of these assumptions, the principle of detailed balance allows us to describe the general compensation process by

$$\lambda Si_{Ga}^{+} + \{D\} + (\lambda + \gamma)e^{-} \rightleftarrows A + \lambda V_{Ga}^{\bullet} \qquad (3)$$

where $\{D\}$ represents neutral defects whose concentrations are assumed to depend only on the annealing temperature. The corresponding mass action expression is

$$\frac{[A]}{[Si_{Ga}^{+}]^{\lambda} n^{\lambda+\gamma}} = k(T_a) \qquad (4)$$

where $k(T_a)$ depends only on the annealing temperature T_a. The conservation laws are

$$n = [Si_{Ga}^{+}] - \gamma[A] \qquad (5)$$

$$n_{Si} = [Si_{Ga}^{+}] + \lambda[A] \qquad (6)$$

where intermediary species are neglected. The electrical activation $a = (n/n_{Si})$ given by these approximations is

$$\frac{1-a}{(\gamma + \lambda a)^{\lambda} a^{\lambda+\gamma}} = (\lambda + \gamma)^{1-\lambda} k(T_a) n_{Si}^{2\lambda+\gamma-1}. \qquad (7)$$

The asymptotic behavior at large n_{Si} for a neutral species A, e.g. $\gamma = 0$, gives $d \log a/d \log n_{Si} = -1.0 + 1/2\lambda$. The asymptotic behavior at large n_{Si} for $\gamma \neq 0$ gives $d \log a/d \log n = -1 - (\lambda - 1/\lambda + \gamma)$. Table 1 lists $d \log a/d \log n_{Si}$ for various values of λ and γ. We conclude from comparing Table 1 and the observed value (-1.0 ± 0.1) that an ionized acceptor state $(\gamma > 0)$ binding a single Si $(\lambda = 1)$ is responsible for the observed saturation behavior associated with annealing at 850°C and 1200°C. In eqn

Table 1. Tabulation of asymptotic values of $d \log a/d \log n_{Si}$ at large n_{Si} given by eqn (7) for various values of λ, γ

	$\lambda = 0$	$\lambda = 1$	$\lambda = 2$
$\gamma = 0$	0	- 0.5	- 0.75
$\gamma = 1$	0	- 1.0	- 1.33
$\gamma = 2$	-0.5	- 1.0	- 1.25

(7), only the constant $k(T)$ is altered if several species with the same λ, γ dominated the saturation process. Furthermore, the inclusion of intermediaries in eqn (6) does not alter the leading order behavior as given by eqn (7). Following the approach of Kung *et al.*[6], a more detailed calculation assuming

$$\frac{[A]}{[Si_{Ga}^{+}]} = k(T)\, e^{(\gamma+1)\omega/kT}$$

gives good correlation with the knee in Fig. 5 at $\sim 10^{18}$ Si cm^{-3} for $\gamma = 1$ or 2. The two previously reported defects Si_{As}^{-} and $Si_{Ga}V_{Ga}^{-}$ are consistant with our observations; however, the charge states of the later species are uncertain.

Kung *et al.* have shown that Si_{As}^{-} accounts for the saturation behavior at ~1240°C[6], although another species such as $Si_{Ga}V_{Ga}$ appears to be responsible in the temperature range 400–750°C[7, 20].

5. CONCLUSIONS

Our results show that the electrical activation of implanted Si after 850–900°C annealing does not significantly differ from that observed in bulk Si doped GaAs. There is no evidence that alteration of the stoichiometry of the implanted layer with As will enhance Si activation, though residual damage appears to affect activation.

Acknowledgements—We thank I. Suni, C. Malhiot and C. Swarts (Caltech) for helpful discussions in connection with this work. The assistance of the reviewer in directing our attention to significant literature is gratefully acknowledged. The samples were prepared at Rockwell International Science Center, Thousand Oaks, where the project benefitted from the assistance and guidance of C. G. Kirkpatrick. The work was financially supported in part by the Advanced Research Projects Agency of the Department of Defense and was monitored by the Air Force Office of Scientific Research under Contract No. F-49620-77-C-0087.

REFERENCES

1. Tandon J. L., Nicolet M-A. and Eisen F. H., *Appl. Phys. Lett.* **34**, 165 (1979).
2. Hobgood H. M., Eldridge G. W., Barret D. L. and Thomas R. N., *IEEE Trans. Electron Dev.* **ED-27**, 140 (1981).
3. Masuyama A., Nicolet M-A., Golecki I., Tandon J. L., Sadana D. K. and Washburn J., *Appl. Phys. Lett.* **36**, 749 (1980).
4. Milnes A. G., *Deep Impurities in Semiconductors*, pp. 46–63. Wiley, New York (1973).
5. Whelan J. M., Struthers J. D. and Ditzenberger J. A., *Proc. Int. Conf. Semicond. Phys. Prague*, 1960, p. 943. Czechoslovak Academy of Sciences, Prague (1961).
6. Kung J. K. and Spitzer W. G., *J. Appl. Phys.* **45**, 2254 (1974).
7. Kung J. K. and Spitzer W. G., *J. Appl. Phys.* **45**, 4477 (1974).
8. Swaminathan V. and Copley S. M., *J. Appl. Phys.* **47**, 4405 (1976).
9. Stoneham E. B., Patterson G. A. and Gladstone J. M., *J. Elect. Mat.* **9**, 2 (1980).
10. Inada T., Kato S., Ohkubo T. and Hara T., *Proc. 1st Int. Conf. on Ion Beam Modification of Materials*, p. 401. Budapest, Hungary (1978).
11. Stolte C. A., *Ion Implantation in Semiconductors* (Edited by F. Chernow, J. A. Borders and D. K. Brice), p. 149. Plenum Press, New York (1976).
12. Müller H., Eisen F. H. and Mayer J. W., *J. Electrochem. Soc.* **122**, 651 (1975).
13. Gibbons J. F., Johnson W. S. and Mylrorie S. W., *Projected Range Statistics*. Dowden, Hutchinson & Ross, Stroudsburg, Pennsylvania (1975).
14. Grimaldi M. G., Paine B. M., Nicolet M-A. and Sadana D. K., *Appl. Phys. Lett.* **39**, 70 (1981).
15. Speriosu V. S., Paine B. M., Nicolet M-A. and Glass H. L., *Appl. Phys. Lett.* **40**, 604 (1982).
16. Sadana D. K. and Booker G. R., *Radiat. Eff.* **42**, 35 (1979).
17. Logan R. M. and Hurle D. T. J., *J. Phys. Chem. Solids* **32**, 1739 (1971).
18. Blanc J., Bube R. H. and Weisberg L. R., *Phys. Rev. Lett.* **9**, 252 (1962).
19. Libowitz G. G., *Treatise on Solid State Chemistry*, Vol. 1 *The Chemical Structure of Solids* (Edited by N. B. Hannay), pp. 335–361. Plenum Press, New York (1975).
20. Kung J. K. and Spitzer W. G., *J. Appl. Phys.* **44**, 912 (1973).
21. Longini R. L. and Greene R. F., *Phys. Rev.* **102**, 992 (1956).
22. Spitzer W. G. and Panish M. B., *J. Appl. Phys.* **40**, 4200 (1969).
23. Hwang C. J., *J. Appl. Phys.* **40**, 4591 (1969).
24. Brouwer G., *Philips Res. Rep.* **9**, 366 (1954).

APPENDIX I

Consider a system of non-interacting particles with volume V possessing two finitely degenerate levels as depicted in Fig. 6. The partition function can be written $Z = Z_0(\eta_0) \cdot Z_1(\eta_1)$ where

$$Z_0 = \frac{N_0!}{(N_0 - \eta_0)!\eta_0!} e^{-\eta_0\epsilon_0/kT}$$

$$Z_1 = \frac{N_1!}{(N_1 - \eta_1)!\eta_1!} e^{-\eta_1\epsilon_1/kT}$$

and η_0 is the number of particles in the ground state, η_1 is the number occupying the higher energy state, and $\eta_0 + \eta_1 = \eta_t$ is the total number of particles introduced into the system; $\eta_t < N_0 + N_1$. Neglecting volume effects, the equilibrium condition $dF/d\eta_0 = 0$ implies

$$\frac{d}{d\eta_0} kT \ln [Z_0(\eta_0) \cdot Z_1(\eta_t - \eta_0)] = 0.$$

Application of the Stirling approximation with $a = \eta_0/\eta_t$ and the assumption that $\eta_t \ll N_1$ gives the quadratic

$$a^2 - \left[1 + (1+\theta)\frac{n_0}{n_t}\right] a + \frac{n_0}{n_t} = 0 \tag{8}$$

where the densities $n_0 = N_0/V$, etc., have been introduced, and $\theta = N_1/N_0 \exp(\epsilon_0 - \epsilon_1/kT)$. Simple algebraic manipulation gives eqn (2), with $n_t = n_{Si}$. For fixed θ, the limiting behavior is

$$a \simeq (1+\theta)^{-1} \quad \text{for } n_t \ll n_0$$

$$a \simeq \left(\theta + \frac{n_t}{n_0}\right)^{-1} \quad \text{for } n_t \gg n_0. \tag{9}$$

The graphs of a and $\log 1/a - 1$ vs n_{Si}/n_0 calculated from eqn (8) for various θ are shown in Fig. 6.

Appendix AIV.1 Profile for Exponential Injection

The concentration profile for atoms injected into a semi-infinite region wherein they may move by diffusion and the interface at $x = 0$ is a sink was described in Chapter IV for an arbitrary injection profile $f(x)$. A straight forward solution of the diffusion equation with an exponential injection profile; $\frac{\partial C}{\partial t} = D\frac{\partial^2 C}{\partial x^2} + e^{-\beta x}$, subject to the initial condition $C = 0$ and the boundary conditions that C vanish at $X = 0$ and for $x \to \infty$ can be obtained by separation of variables with a Laplace transform taken in t

$$\hat{C}(x,s) = \frac{e^{-\beta x} - e^{-\frac{s^{1/2}}{\sqrt{D}}x}}{s\,(s - \beta^2 D)} \quad .$$

The Convolution Theorem simplifies evaluating the inverse transform. The result is (a mess);

$$C(x,t) = e^{-\beta x}\left[\frac{e^{\beta^2 Dt} - 1}{\beta^2 D}\right] + \frac{1}{\beta^2 D}\operatorname{erfc}\frac{x}{2t^{1/2}D^{1/2}}$$

$$- \frac{e^{\beta^2 Dt}}{\beta^2 D}\,\frac{1}{2}\left[e^{\beta x}\operatorname{erfc}\left(\frac{x + 2\beta Dt}{2D^{1/2}t^{1/2}}\right) + e^{-\beta x}\operatorname{erfc}\left(\frac{x - 2\beta Dt}{2D^{1/2}t^{1/2}}\right)\right] \qquad (1)$$

The first term represents the accumulating injection profile broadened by diffusion, while the third term accounts for the diffusional loss to the interface. The long term behavior is produced by the second term. The asymptotic behavior is

$$C(x,t) \sim t\, e^{-\beta x} \qquad \text{for } x > 0,\ t \to 0$$

$$\sim \frac{1}{\beta^2 D}\operatorname{erfc}\frac{x}{2D^{1/2}t^{1/2}} \qquad \text{for } t \to \infty \ .$$

It is convenient to introduce the dimensionless variables $X = \beta x$, and $T = \beta^2 Dt$. In these variables:

$$\beta^2 D\, C(X,T) = e^{-X}(e^{T} - 1) - \frac{1}{2}e^{T}\left[e^{X}\operatorname{erfc}\left(\frac{X+2T}{2T^{1/2}}\right) + e^{-X}\operatorname{erfc}\left(\frac{X-2T}{2T^{1/2}}\right)\right]$$

$$+ \operatorname{erfc}\frac{X}{2T^{1/2}} \ .$$

Fig. A1 shows a plot of $\ln\frac{\beta^2 DC(X,T)}{T}$ versus X for several values of T. The tail becomes noticeably distorted for $X > 2$ when $T \simeq 0.5$. This corresponds to $\beta^{-2} \simeq 2Dt$ which is just the variance for spreading of a thin marker.

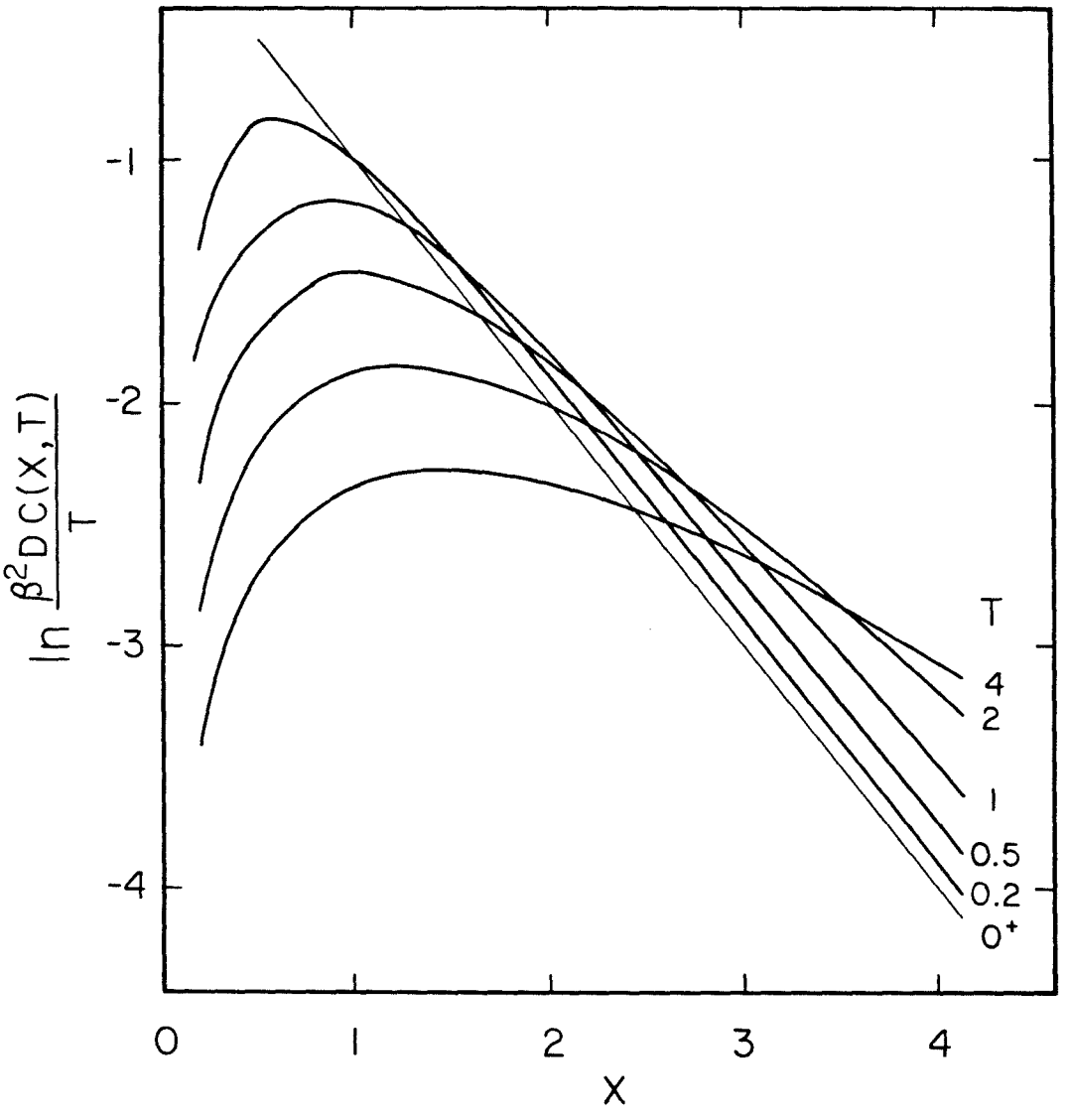

Figure A1. Evolution of concentration profile for exponential injection .

Appendix A V.1 Range Statistics

A. Approximate Range Statistics in a Bilayer Medium

A number of treatments of this problem can be found in the literature [1-4]. We extend the continuously slowing down approximation used by Jiminez-Rodriguez [4] to include lateral straggling when the moving atom crosses the interface only once. Atom 1 starts at a distance z from the interface with energy E_0 in material 2, moving initially along the normal toward the interface. It may cross the interface with energy $E>0$, while moving in a direction with respect to the normal given by $\omega = \cos\Theta$. This atom proceeds into layer 3 to a depth r. The distribution for r obtained by following this trajectory can be written

$$P(r\,|\,E_0) = \int dE \int d\omega\, P(E,\omega\,|\,E_0,z)\, P(r\,|\,E,\omega) \tag{1}$$

where $P(r\,|\,E,\omega)$ is the distribution for r given E and ω, while $P(E,\omega\,|\,E_0,z)$ is the joint distribution for E and ω at the interface. If atom 1 crosses the interface only once, then $P(r\,|\,E,\omega)$ is approximately Gaussian with mean $\langle r\rangle(E,\omega) = \omega R_{13}(E)$ and variance

$$\sigma_r^2(E,\omega) \;=\; \omega^2\,\sigma_x^2(E) \;+\; (\,1-\omega^2\,)\,\sigma_y^2(E)$$

where R_{13} is the projected range of 1 in 3 for a given E, while σ_x, σ_y are the projected range and transverse straggling respectively. Motivation for this is shown in Fig. 3b of this chapter. We shall assume that $\sigma_x = \sigma_y = \sigma_{13}$ (please examine Fig. 4 in Chapter V). The first two moments of $P(r\,|\,E_0)$ are then

$$\langle r\rangle(E_0) = \int dE \int d\omega\, P(E,\omega|E_0,z)\ \omega R_{13}(E) \tag{2}$$

$$\langle r^2\rangle(E_0) = \int dE \int d\omega\, P(E,\omega|E_0,z)\ [\ \omega^2 R_{13}^2(E) + \sigma_{13}^2(E)\ ] \tag{3}$$

Winterbon [1,2] and others have shown for power law scattering with parameter m that $R_{13}(E) \simeq g_{13} E^{2m}$. Eqn. 2 consequently implies that

$$\langle r\rangle(E_0) = g_{13} \cdot \int dE \int d\omega\, P(E,\omega|E_0,z)\ \omega E^{2m}$$

We shall now employ the same translational invariance argument used to derive the Boltzmann transport equation in classical range theory [5]. If layer 3 has the same compositon as layer 2, then the interface only shifts our point of reference by z. The range expression applied to layer 2 gives

$$\langle r\rangle_{same} = g_{12} E_0^{2m} - z = g_{12} \cdot \int dE \int d\omega\, P(E,\omega|E_0,z)\ \omega E^{2m} \tag{4}$$

Rearrangement and substitution back into Eqn. 2 produces

$$\langle r\rangle(E_0) = g_{13}\ (\ E_0^{2m} - \frac{z}{g_{12}}) \tag{5}$$

The parameter $m = \frac{1}{2}$ is appropriate for the systems we have been examining [5]. We shall assume that σ_{13} varies linearly with E; $\sigma_{13} = h_{13} E$ [1,2,6]. With this approximation, Eqn. 3 gives

$$\langle r^2\rangle(E_0) = g_{13}^2\ \langle\omega^2 E^2\rangle + h_{13}^2\ \langle E^2\rangle$$

where $\langle E^2\rangle = \int E^2 dE \int d\omega P(E,\omega|E_0,z)$, etc. The variance of r is given by

$$\sigma_r^2(E_0) = g_{13}^2\ \langle\omega^2 E^2\rangle + h_{13}^2\ \langle E^2\rangle - g_{13}^2\ (\ E_0 - \frac{z}{g_{12}})^2 \tag{6}$$

σ_r^2 is independent of z if we make 2 and 3 the same material and assumes the value $h_{12}^2\ E_0^2$. This constraint on Eqn. 6 implies that

$$\langle \omega^2 E^2 \rangle \simeq \left(E_0 - \frac{z}{g_{12}} \right)^2 + \frac{h_{12}^2}{g_{12}^2} \left(E_0^2 - \langle E^2 \rangle \right) \tag{7}$$

Consequently,

$$\sigma_r^2 \simeq h_{13}^2 E_0^2 + g_{13}^2 \left[\frac{h_{12}^2}{g_{12}^2} - \frac{h_{13}^2}{g_{13}^2} \right] \left(E_0^2 - \langle E^2 \rangle \right) \tag{8}$$

To first order in z

$$\langle E^2 \rangle = \langle E \rangle^2 + \langle E - \langle E \rangle \rangle^2 \simeq \left(E_0 - S_{12} z \right)^2 + \frac{1-m}{2-m} \gamma_{12} E_0 S_{12} z$$

where S_{12} is the total stopping power for 1 in 2. The constants in the second term are for power law scattering when nuclear stopping dominates. The result of combining the last two equations is

$$\sigma_r^2 \simeq h_{13}^2 E_0^2 + g_{13}^2 E_0^2 \left[\frac{h_{12}^2}{g_{12}^2} - \frac{h_{13}^2}{g_{13}^2} \right] \left[\left[2 - \frac{1-m}{2-m} \right] \gamma_{12} \frac{S_{12} z}{E_0} - O\left[\frac{S_{12} z}{E_0} \right]^2 \right] \tag{9}$$

Equations 5 and 9 were used to calculate the implantation profiles for oxygen and Xe in Ni/SiO_2 refered to in chapter III. The second term vanishes if h scales with g. This was assumed in calculating the recoil implantation profiles. The arguments used to obtain Eqn. 5 can be extended to a multilayer target by induction with the result

$$E_0^{2m} = \int_0^{\langle r \rangle} \frac{d\xi}{g(\xi)}$$

This represents a generalization of the result given in [4].

B. Another Look at Range Theory for Homogeneous Materials

The projected range $R(E)$ for a homogeneous target can be derived using Eqn. 2 from the behavior as $z \to 0$, where the approximation is most accurate. Translational invariance when layers 2 and 3 are the same gives

$$R(E_0) - z = \int dE \int d\omega \, P(E,\omega | E_0,z) \, \omega R(E)$$

Expanding about $z = 0$ gives

$$\int dE \int d\omega \, \omega \, R(E) \, \frac{\partial}{\partial z} P(E,\omega | E_0,z) \Big|_{z=0} = -1 \qquad (11)$$

As mentioned in Appendix V.2, the angular deflections are correlated with the nuclear energy loss so that $P(E,\omega | E_0,z) = P(\omega | E,E_0) \cdot P(E | E_0,z)$. An expression for $\bar{\omega}(E,E_0) = \int d\omega \, \omega P(\omega | E,E_0)$, originally derived by J. Biersack, is also given there. Substitution gives

$$\int dE \, R(E) \, \bar{\omega}(E,E_0) \, \frac{\partial}{\partial z} P(E | E_0,z) \Big|_{z=0} = -1$$

Lateral straggling can be neglected in calculating $P(E | E_0,z)$ since it represents a second-order effect. The energy dependence in the cross-sections can be ignored for P but not $\bar{\omega}$. An exact solution $P(E | E_0,z)$ for small z to an approximate transport equation is required by this hybrid approach. Note that the last equation will immediately give g if $R(E) = g \, E^{2m}$.

References

[1] K. B. Winterbon, *Appl. Phys. Lett.* **31**, 649 (1977)

[2] K. B. Winterbon, *Radiation Effects* **39**, 31 (1978)

[3] J. Bottiger, J. A. Davies, P. Sigmund and K. B. Winterbon, *Radiation Effects* **11**, 69 (1971)

[4] J. J. Jiminez-Rodriguez, D. S. Karpuzov, R. G. Elliman, M. J. Nobles, S. Kostic and D. G. Armour, *Nucl. Inst. and Meth.* **209/210**, 43 (1983)

[5] U. Littmark and J. F. Ziegler, *Handbook of Range Distributions for Energetic Ions in all Elements* (Pergamon, Elmsford, NY, 1983)

[5] J. F. Gibbons, W. S. Johnson and S. W. Mylroie, *Projected Range Statistics* (Dowden, Hutchinson and Ross, Stroudsburg, 1975)

Appendix A V.2 Random Walk on a Sphere

Consider, if you will, a point on the surface of a unit sphere with polar coordinates (θ,φ). A random walk is generated if we let this point hop in discrete steps of arc length R about the surface of the sphere. In many physical applications the point starts out at the pole $\theta = 0$ and the distribution in θ is of physical interest. θ describes the angular deflections in ion range calculations where each step corresponds to an elastic collision. Clearly the magnitude R and direction of each hop are random variables. Several treatments of this problem can be readily found in the literature [1-4]. An inherent difficulty in this problem is associated with the non-commutativity of rotations. W. H. Furry worked the problem using quaternions to represent the rotation associated with each step, for which a transport equation was deduced [1]. A generalization of Furry's analysis was made by L. D. Favro using Cayley-Klein parameters to describe the rotation [2]. Percival and Richards [3], and J. Beirsack [4] adopted a phenomenological approach using the diffusion equation in spherical coordinates. The latter is not very satisfying, since indirect arguments must be employed to obtain the diffusion coefficient. In this appendix we show a simple way to derive the moments of $\cos\theta$ directly from the description of the points motion with each step.

Let Θ_n, Θ_{n+1} be the polar angle of the point after n and $n+1$ steps. Let the intervening step be defined as shown in Fig. A1. We shall assume that the direction Ψ is uniformly distributed on $[-\pi,\pi]$, while R has a known distribution on $[0,\pi]$. From spherical trigonometry

$$\cos\Theta_{n+1} = \cos\Theta_n \cos R + \sin\Theta_n \sin R \cos\Psi \qquad (1)$$

Θ_n, R and Ψ are uncorrelated. The average value is

$$\langle\cos\Theta_{n+1}\rangle = \langle\cos\Theta_n\rangle\langle\cos R\rangle$$

since $\langle\cos\Psi\rangle = \int_{-\pi}^{\pi}\cos\psi\cdot\frac{1}{2\pi}d\psi = 0$. Consequently

$$\langle\cos\Theta_n\rangle = \langle\cos\Theta_0\rangle\langle\cos R\rangle^n \tag{2}$$

The average number of displacements $\bar{n}$ is usually specified by a physical problem, rather than n. The distribution for n will be Poisson for small enough $\bar{n}$. The first moment when $\bar{n}$ is given will be

$$\langle\cos\Theta\rangle(\bar{n}) = \sum_{n=0}^{\infty}\frac{\bar{n}^n e^{-\bar{n}}}{n!}\langle\cos\Theta_n\rangle$$

$$= \langle\cos\Theta\rangle(0)\cdot e^{\bar{n}(\langle\cos R\rangle - 1)} \tag{3}$$

Typically, $\langle\cos R\rangle$ can be expected to change with n. The nuclear scattering cross-section of a moving atom changes with the energy loss following each collision. Generally, $\bar{n}$ and $\langle\cos R\rangle$ are related to a common parameter t, such as the atom's energy. If we let $\bar{n} = \lambda(t)\,dt$, then repeated application of Eqn. 2 gives

$$\langle\cos\Theta\rangle(t) = \langle\cos\Theta\rangle(0)\cdot e^{\int_0^t\lambda(\tau)[\langle\cos R\rangle(\tau) - 1]d\tau} \tag{4}$$

The assumptions leading to Eqn. 4 are the same as those used to derive the transport equation for the probability density function. Note that if the distribution for R is sharply peaked about $R = 0$, then $\langle\cos R\rangle \simeq 1 - \frac{1}{2}\langle R^2\rangle$, so that the term in brackets resembles a diffusion coefficient, and

$$\langle\cos\Theta\rangle(t) \simeq \langle\cos\Theta\rangle(0)\cdot e^{-\frac{1}{2}\int_0^t\lambda(\tau)\langle R^2\rangle(\tau)d\tau} \tag{5}$$

as previously reported [2-4].

The second moment obtained using Eqn. 1 is

$$\langle\cos^2\Theta_{n+1}\rangle = \frac{1}{2}\langle\sin^2 R\rangle + \left(1 - \frac{3}{2}\langle\sin^2 R\rangle\right)\langle\cos^2\Theta_n\rangle$$

since $\langle\cos^2\Psi\rangle = \frac{1}{2}$. This recursion relation can be readily solved. The previous arguments concerning the distribution of n also apply. The physical distribution is

$$\langle\cos^2\Theta\rangle(\bar{n}) = \frac{1}{3}\left\{1 - e^{-\pi\frac{3}{2}\langle\sin^2 R\rangle}\right\} + \langle\cos^2\Theta\rangle(0)\cdot e^{-\pi\frac{3}{2}\langle\sin^2 R\rangle}$$

The expression analogous to Eqn. 4 using $\bar{n} = \lambda\, dt$ is

$$\langle\cos^2\Theta\rangle(t) = \frac{1}{3}\left\{1 - e^{-\frac{3}{2}\int_0^t \lambda\langle\sin^2 R\rangle\, d\tau}\right\} + \langle\cos^2\Theta\rangle(0)\cdot e^{-\frac{3}{2}\int_0^t \lambda\langle\sin^2 R\rangle\, d\tau} \qquad (6)$$

The higher moments can be generated in exactly the same way with somewhat greater effort. The probability density function for Θ only depends on the quantity $\int_0^t \lambda\langle R^2\rangle\, d\tau$ [1-4].

J. Biersack was the first to apply these results to ion range calculations [4]. Fig. A2 shows the collision of an atom 1 by atom 2 in the laboratory reference frame. Conservation of energy and momentum give

$$\cos R = \frac{1 - \frac{1}{2}\left(1 + \frac{M_2}{M_1}\right)\frac{T}{E}}{\left(1 - \frac{T}{E}\right)^{\frac{1}{2}}}$$

where E is the incident atom's energy and T is the energy lost to atom 2. A simple approximation for $T \ll E$ is $\cos R \simeq 1 - \frac{1}{2}\frac{M_2}{M_1}\frac{T}{E} + O\left(\frac{T}{E}\right)^2$. Using the energy E of atom 1 as the parameter t in Eqn. 4 with $\langle\cos\Theta\rangle(E_0) \equiv 1$ gives

$$\langle\cos\Theta\rangle(E) = e^{-\lambda\frac{M_2}{M_1}\int_E^{E_0}\frac{S_n}{S_n+S_e}\varepsilon^{-1}d\varepsilon} \qquad (7)$$

where E_0 is the initial energy, $\langle T\rangle = \int T\, d\sigma_{12} / \int d\sigma_{12}$ is the average energy loss per collision, $\lambda = \frac{1}{S_n + S_e}\rho^2 \int d\sigma_{12}$ is average number of collisions per unit energy loss, $S_n = \rho_2 \int T\, d\sigma_{12}$ is the energy loss per unit lenght due to nuclear collisions and $S_n + S_e$ is the combined nuclear and electronic stopping. Eqns. 5,6 show that $\langle\cos^2\Theta\rangle \simeq \frac{1}{3} + \frac{2}{3}\langle\cos\Theta\rangle^3$ when Θ initially starts from zero. Fig. A3 shows the variation in the mean and standard deviation of $\cos\Theta$ as a function of the average position of an atom for a given energy loss assuming that $(M_2/M_1)(S_n/S_n + S_e) = 1$ [4]. It is evident that the lateral straggling is not very significant until the near the end of the projected range.

References

[1] W. H. Furry, *Phys. Rev.* **107**, 7 (1957)

[2] L. D. Favro, *Phys. Rev.* **119**, 53 (1960)

[3] I. Percival and D. Richards, *J. Phys. B.* **12**, 2051 (1979)

[4] J. P. Biersack, *Nucl. Instr. and Meth.* **182/183**, 199 (1981)

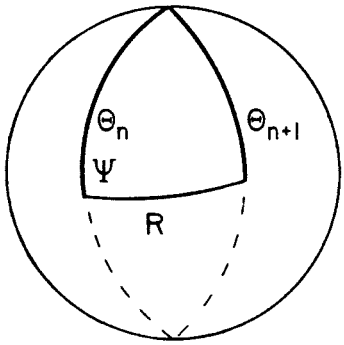

Figure A1.

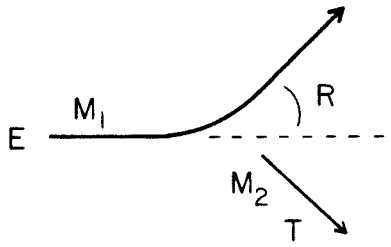

Figure A2.

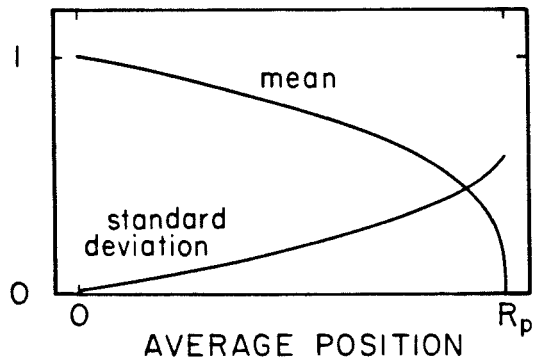

Figure A3.